Spin and charge properties of Si: P probed using ion-implanted nanostructures

Author:
McCamey, Dane Robert

Publication Date:
2007

DOI:
https://doi.org/10.26190/unsworks/17682

Spin and Charge Properties of Si:P Probed using Ion-Implanted Nanostructures

Dane Robert McCamey

THE UNIVERSITY OF
NEW SOUTH WALES

SCHOOL OF PHYSICS

A thesis submitted in fulfilment of the requirements for the degree
Doctor of Philosophy

April 10, 2007

PLEASE TYPE

THE UNIVERSITY OF NEW SOUTH WALES
Thesis/Dissertation Sheet

Surname or Family name: McCamey
First name: Dane   Other name/s: Robert
Abbreviation for degree as given in the University calendar: Ph.D.
School: Physics   Faculty: Science
Title: Spin and Charge Properties of Si:P Probed using Ion-Implanted Nanostructures

Abstract 350 words maximum: (PLEASE TYPE)

This thesis investigates the defects, charge states and spin properties of phosphorus doped silicon, and is motivated by a number of proposals for quantum information processing (QIP) that involve using the spin or charge of individual donors in silicon as qubits.

The implantation of phosphorus into silicon is investigated; specifically the ability to remove damage and activate the implanted donors. The impact of implantation on the transport properties of silicon MOSFETs at cryogenic temperatures is used to investigate the damage. Implanting phosphorus into the MOSFET channel leads to reduced electron mobility. The defect density increases linearly with implant density ($\Delta n_{\mathrm{defect}} = 0.08 \pm 0.01 n_{\mathrm{implant}}$). Silicon implantation does not show this effect, suggesting that the additional defects are ionised P donors in the channel. Implant activation for low density donors was complete for an implant density of 2×10^{12} cm^{2}.

Similar studies were undertaken on devices with a variety of dielectrics. Thermally grown SiO_2 was found to have the lowest defect density of those studied, although Al_2O_3 deposited via atomic layer deposition was found to have properties that may be useful for the fabrication of devices with low thermal processing budgets. The as-grown defect density of the thermal silicon dioxide was found to be $2.1 \pm 0.3 \times 10^{11}$ cm^{2}.

Ion implantation of nanoscale devices allowed the spin properties of a small number of phosphorus donors in silicon to be probed via electrically detected magnetic resonance. This allowed the detection of the spin resonance of as few as 100 spins. This represents an improvement in number detection of 4 orders of magnitude over previous EDMR studies of donors in silicon. EDMR was used to investigate the properties of P donors in isotopically purified ^{28}Si . The material had a background doping level too high to detect small numbers of spins, however, the narrow linewidth of the phosphorus resonance confirm that the isotopic purity is greater than 0.999.

A proof-of-principle demonstration of pulsed EDMR of ion-implanted donors in silicon is presented. The spin dependent transient that results from manipulating the donor spins via pulsed ESR is sensitive to as few as 10^4 donors, and is a required component for observation of spin Rabi oscillations by this technique.

Declaration relating to disposition of project thesis/dissertation

………………………………………….. ………………………………………..……………… September 15, 2007
Signature   Witness   Date

FOR OFFICE USE ONLY   Date of completion of requirements for Award:

Registrar and Deputy Principal

THIS SHEET IS TO BE GLUED TO THE INSIDE FRONT COVER OF THE THESIS

Certificate of originality

I hereby declare that this submission is my own work and to the best of my knowledge it contains no materials previously published or written by another person, or substantial proportions of material which have been accepted for the award of any other degree or diploma at UNSW or any other educational institution, except where due acknowledgement is made in the thesis. Any contribution made to the research by others, with whom I have worked at UNSW or elsewhere, is explicitly acknowledged in the thesis.

I also declare that the intellectual content of this thesis is the product of my own work, except to the extent that assistance from others in the project's design and conception or in style, presentation and linguistic expression is acknowledged.

(Signed)

(Date) September 15, 2007

Copyright Statement

(Signed)

(Date) September 15, 2007

Authenticity Statement

(Signed)

(Date) September 15, 2007

Abstract

This thesis consists of work carried out to investigate the defects, charge states and spin properties of phosphorus doped silicon. This investigation is motivated by a number of proposals for quantum information processing that involve using the spin or charge of individual donors in silicon as qubits.

The work begins by investigating the implantation of phosphorus into silicon; specifically the ability to remove damage and activate the implanted donors. This problem has been studied in detail for high dose implantation for room temperature operation, due to its importance in conventional silicon microelectronics. However, in this thesis the impact of implantation on the transport properties of silicon MOSFETs at cryogenic temperatures is used to investigate the damage in a regime where QIP devices are expected to operate. The implantation of phosphorus into the channel of the MOSFET is found to reduce the mobility of the device by increasing the charge carrier scattering from ionised impurities. The increase in defect density is found to be a linear function of the implant density, with a proportionality factor of 0.08 ± 0.01. Similar measurements on devices with silicon implantation do not show this effect, leading to the conclusion that the increased defects are in fact ionised phosphorus donors in the channel of the MOSFET. Implant activation for low density donors was determined, by room temperature threshold voltage measurements, to be unity for an implant density of $2 \times 10^{12}\mathrm{cm}^{-2}$.

Similar low temperature studies were undertaken on devices with a variety of dielectric materials. Thermally grown silicon dioxide was found to have the lowest defect density of the materials studied, although aluminium oxide deposited via atomic layer deposition was found to have properties that may be useful for the fabrication of devices with low thermal processing budgets. The as grown defect density of the thermal silicon dioxide was found to be $2.1 \pm 0.3 \times 10^{11}\mathrm{cm}^{2}$, which may allow development of QIP devices containing one or two qubits but will need to be improved for larger scale implementation

Ion implantation of nanoscale devices was then used to allow the spin properties of a small number of phosphorus donors in silicon to be probed via electrically detected magnetic resonance. This technique detects spin resonance by the change in current caused by the change in the recombination rate of photoexcited carriers when electron spin resonance conditions are satisfied, and is significantly more sensitive than conventional electron spin resonance. By combining this technique with devices where the current is restricted to flow through a very small region containing a small number of donors, the resonance of as few as 100 spins was observed. This represents an improvement of at least 7 orders of magnitude than conventional electron spin resonance, and 4 orders of magnitude over previous EDMR studies of donors in silicon.

This technique was then used to investigate the properties of P donors in isotopically purified ^{28}Si . The material was found to have a background doping level too high to allow the detection of small numbers of spins, however, the narrow linewidth ($B_{p-p} < 0.04$mT) of the phosphorus resonance was used to determine that the isotopic purity was better than 0.999.

A proof of principle demonstration of pulsed EDMR of ion-implanted donors in silicon presented. This measurement of the spin dependent transient that results from manipulating the donor spins via pulsed ESR is show to be sensitive to as few as 10^4 donors, and is a required component for observation of spin Rabi oscillation by this technique.

Finally, initial measurements of a new device architecture for the detection of EDMR in the channel of a Si-MOSFET is presented. This device may allow the detection of EDMR on microsecond timescales at millikelvin temperatures.

Acknowledgements

Undertaking the work in this thesis was a truly enjoyable experience, due to a number of factors. These ranged from learning new things, from physics to fabrication techniques, writing, submitting and having papers accepted into journals, traveling to and attending conferences and undertaking work at different labs. However, the most important were the people with whom I was privileged to work.

This work was guided by two supervisors, Robert Clark and Alex Hamilton. I would like to thank them both for their support and guidance during my thesis. Alex invited me to undertake this work in the Centre for Quantum Computer Technology, and I am grateful to him for the opportunity to work in such a professional and innovative group. Bob, who must be acknowledged for his tireless leadership of the Centre, supervised me in the final years of this work. I am grateful to Bob for the opportunities he provided for me (and indeed all of the students in the group), especially the ability to interact with outstanding scientist from all around the world. Indeed, the first time I traveled out of Australia was to a conference with Bob, which I greatly enjoyed.

One of the really great things about working in this group has been the outstanding scientist who I was able to work with. Andrew Ferguson always ready with great ideas and for great discussions. Victor Chan was an invaluable source of advice (especially about fabrication), as well as some pretty awful jokes. In the first couple of years, expansive and wide ranging physics discussions at coffee were made enjoyable and challenging by David Reilly and Tilo Buehler, both of whom were happy to answer (sometimes non-thinking) questions from new PhD students. Nadia Court and Susan Angus have been office mates of the highest calibre. Discussions ranged from aluminium evaporation to cooking, and I enjoyed (and learnt from) every one of them. I have also enjoyed working with Rolf Brenner, Neil Curson, Fey Hudson, Marc Ahrens, Maja Cassidy, Toby Halam, Matt Butcher, Mladen Mitic, Søren Andresen, Lars Hanson, Thilo Reuss, Chris Escott and Andrew Dzurak.

Much of the work presented in this thesis was possible because of the quality of the labs I was able to use. For this, I thank Dave Barber, Bob Starret and Eric Gauja, who give great support and advice whenever it is needed. Eric is a walking encyclopedia of semiconductor fabrication techniques, and David and Bob could design/build/fix just about anything. Also, Marin Brauhart provided an outstandingly safe working environment, as well as a great balcony for BBQ's on a summer evening.

Without the patient advice and and hours of ion implantation by Jeff McCallum from the University of Melbourne, this thesis would not have been possible. Jeff is an invaluable source of information regarding both the practical and theoretical aspects of ion implantation, and I thank him for his time and patience.

I was fortunate to be able to spend some time undertaking experiments at the Walter Schottkty Institute of the Technische Universitat München. This was made possible by Martin Brandt whom I thank for the wonderful opportunity. I thank Hans Huebl for teaching me how to do EDMR, and for his friendship during my time in Germany. I also need to thank the diplom students of the institute, especially Andre Stegner, who went out of their way to make me feel at home.

My old friends, Ratso, PK, Trina, KP and Lisa, have been the source of necessary distraction, and I would like to thank them for the enjoyable times we have shared together.

My Family; Britty, Mum, and Nan, have supported me throughout my time at university. Thank you, I appreciate it a lot. I especially thank my mother for instilling in me a sense of inquisitiveness and a love of learning, which allows me to do what I love for a living.

Finally, Jaci, who has been there for me for the whole time, thank you for your continuous love and support. I have especially appreciated your encouragement during the writing of this thesis.

§§§

This work was supported by the Australian Research Council (ARC) and the Australian Government through the ARC Centre of Excellence for Quantum Computer Technology. It was also supported by the United States National Security Agency (NSA), Advanced Research and Development Activity (ARDA) and Army Research Office (ARO) under contract number DAAD19-01-1-0653. Work conducted at the Walter Schottky Institute was additionally supported by the Deutsche Forschungsgemeinschaft (DFG) through SFB 631.

The award of an Overseas Travel Fellowship from the Australian Research Council Nanotechnology Network is gratefully acknowledged.

CENTRE FOR
QUANTUM COMPUTER
TECHNOLOGY
AUSTRALIAN RESEARCH COUNCIL CENTRE OF EXCELLENCE

For Mum

Contents

List of Figures

List of Tables

List of Abbreviations

The following is a list of standard abbreviations used throughout this thesis.

1D	One dimensional
2D	Two dimensional
ALD	Atomic Layer Deposition
As	Arsenic
cw-EDMR	continuous wave electrically detected magnetic resonance
DAC	Digital-to-analog converter
dc	Direct current
EBL	Electron-beam lithography
EDMR	Electrically detected magnetic resonance
ESR	Electron Spin Resonance
FET	Field-effect transistor
GaAs	Gallium Arsenide
HMDS	Hexamethyl disilizane: $(CH_3)_3SiNHSi(CH_3)_3$
IPA	Isopropyl alcohol: $(CH_3)_2CHOH$
MIBK	Methyl-isobutyl-ketone: $CH_3COCH_2CH(CH_3)_2$
MIT	Metal-insulator-transition
MOS	Metal-oxide-semiconductor
MOSFET	Metal-oxide-semiconductor field-effect transistor
P	Phosphorus

p-EDMR	pulsed electrically detected magnetic resonance
PECVD	Plasma-enhanced chemical vapor deposition
PMMA	Poly(methyl-methacrylate): $H[CH_2C(CH_3)(COOCH_3)]_nH$
QC	Quantum computer/computing
QIP	Quantum information processing
QM	Quantum mechanics/mechanical
qubit	Quantum bit
rf	Radio-frequency
RT	Room temperature ($T = 20$ °C $= 293.15$ K)
SEM	Scanning electron microscope/microscopy
Si:X	Silicon doped with the chemical element X
^{x}**Si**	Isotope x of silicon
^{n}**Si**	Silicon with a natural isotopic abundance
SNR	Signal-to-noise ratio
SOI	Silicon-on-insulator
[X]	doping density of element X

List of Publications

Publications related to this research

- D. R. McCamey, M. Francis, J. C. McCallum, A. R. Hamilton, A. D. Greentree and R. G. Clark, Donor activation and damage in Si-SiO_2 from low-dose, low-energy ion implantation studied via electrical transport in MOSFETs. *Semiconductor Science and Technology* **20**, 363 (2005)
- V. C. Chan, D. R. McCamey, T. M. Buehler, A. J. Ferguson, D. J. Reilly, A. S. Dzurak, R. G. Clark, C. Yang and D. N. Jamieson, An ion-implanted silicon single-electron transistor. *eprint arXiv:cond-mat/0510373* (2005)
- V. C. Chan, T. M. Buehler, D. R. McCamey, A. J. Ferguson, D. J. Reilly, C. Yang, T. Hopf, A. S. Dzurak, A. R. Hamilton, D. N. Jamieson and R. G. Clark, Single-electron transistor coupled to a silicon nano-MOSFET. Micro- and Nanotechnology: Materials, Processes, Packaging, and Systems II, J-C. Chiao, D. N. Jamieson, L. Faraone, A. S. Dzurak, ed., Proc. of SPIE Vol. 5650 (2005) doi: 10.1117/12.583293
- D. R. McCamey, H. Huebl, M. S. Brandt, W. D. Hutchison, R. G. Clark and A. R. Hamilton, Electrically detected magnetic resonance in ion-implanted Si:P nanostructures. *Applied Physics Letters* **89**, 182115 (2006)
- V. C. Chan, T. M. Buehler, A. J. Ferguson, D. R. McCamey, D. J. Reilly, A. S. Dzurak and R.G. Clark, Ion implanted Si:P double-dot with gate tuneable interdot coupling. *Journal of Applied Physics* **100**, 106104 (2006)

Conference Presentations

- D. R. McCamey *et al*. Spin and Charge Properties of Si:P probed using ion-implanted nanostructures. Invited Oral Presentation: International Workshop on Solid State Based Quantum Information Processing, Herrsching, Germany (2006)
- D. R. McCamey *et al*. Electrically detected magnetic resonance in ion-implanted Si:P nanostructures. Poster Presentation: Workshop on ESR and Related Phenomenon in Low Dimensional Structures, Sanremo, Italy, (2006)
- D. R. McCamey *et al*. Electrically-detected magnetic resonance in ion-implanted Si:P nanostructures. Poster Presentation: Oliphant Conference on the Frontiers of Quantum Nanoscience, Noosa, Australia (2006)
- D. R. McCamey *et al*. Spin-Dependent Tunneling and Electron Spin Coupling in Si:P Devices. Poster Presentation: Quantum Computing Program Review, Tampa, USA (2005)
- D. R. McCamey *et al*. Characterization Of Si-SiO_2 Trap Density Due To Ion Implantation. Poster Presentation: 28th Annual Condensed Matter and Materials Meeting, Wagga Wagga, Australia (2004)

Chapter 1

Introduction

1.1 Silicon, Electrons, and Classical Computing

The modern semiconductor industry is based on a single element - silicon. Silicon is used to fabricate one of the most technologically important and ubiquitous electronic devices, the Silicon Metal-Oxide-Semiconductor Field-Effect-Transistor (Si-MOSFET). MOSFETs are used in operational amplifiers, as analog switches, for basic physics research and, importantly, they form the basis of modern computers.

The continuing ability of the semiconductor industry to decrease the size and increase the yield of MOSFETs has led to the increase in computing power as more devices are able to be placed on a single chip. In 1965, Gordon Moore [1] predicted that the power of personal computers would increase exponentially, with a doubling of the number of transistors (which he equated with computing power) on a chip every 18 months. This prediction, which has come to be known as Moore's Law, has held for nearly forty years.[1]

---

[1] It is important to note that Moore's law itself may be driving the roadmap for increasing power, becoming in effect a self-fulfilling prediction.

1.1.1 Decreasing the Size of Semiconductor Devices

Whilst there are difficult technical challenges to be faced in the fabrication of increasingly smaller electronic devices, there are more fundamental challenges to overcome. At the very small characteristic device sizes now being utilized, the effect of quantum mechanics begins to play a much greater role in the device operation. It is these quantum mechanical effects which presently motivate much of the research into mesoscopic devices in the physics community, and which also lead to suggestions of utilising such phenomena in quantum electronic devices.

1.2 Silicon, Spin, and Quantum Computing

Any electronic device in which the operation of that device is dominated by quantum mechanical effects can be considered a quantum electronic device. However, a more intriguing device is one in which the quantum mechanical effects allow us to do things that are not possible with classical electronics.

An example of an application of this type of device is in quantum computation. In classical computation, there exist types of problems that are difficult to solve, in effect becoming exponentially harder as the problem becomes linearly more difficult. An example of this is the factorisation of a number, n, into its prime factors. The most efficient classical algorithms to determine the factors requires an running time proportional to $\exp(c(\log(n))^{1/3}(\log\log(n))^{2/3})$, which, since n is only $\log(n)$ bits in length, increases exponentially with the size of the number [2]. This property has allowed the development of cryptographic systems that rely on the inability to efficiently factorise the product of two large numbers efficiently, such as RSA [3].

However, in 1994 Peter Shor developed a scheme for using the quantum mechanical properties of superposition and entanglement to factorise large numbers in polynomial time [4]. The development of this algorithm has led to a large amount of research into the feasibility of fabricating a system which would allow enough control of quantum mechanical properties of a system to implement this algorithm. This and other algorithms, such as the search algorithm by Grover [5] which increases the efficiency of searching unsorted lists from n-time to $\sqrt{n}$-time, showed that it was feasible to obtain improved computational outcomes using quantum mechanical systems. Schemes have also been developed to perform quantum error correction, such as the scheme of Steane[6, 7], allowing fault tolerant quantum computation [8]. These two developments, showing that in principle quantum computing is useful and achievable, have motivated much of the recent research into QC and QIP.

1.2.1 Quantum Computation

A standard formulation for the implementation of quantum computation involves using the quantum mechanical basis states of a two level system (say the spin of an electron) called for example $|0\rangle$ (for, say, spin up) and $|1\rangle$ (spin down) as a quantum bit (qubit). However, where the classical states of 0 and 1 are discrete, a qubit can exist in any arbitrary superposition of the basis states, $|\psi\rangle = \alpha|0\rangle + \beta|1\rangle$. Also important in QC is the property of entanglement, which is the ability of 2 particles to exist in a state, $|ab\rangle$, that cannot be described as a product of the two single states, $|a\rangle$ and $|b\rangle$ [9]. Using these two properties, it is possible to implement the algorithms described above which provide increased computational power for certain tasks.

It is, however, the physical implementation of such a system that remains challenging. Whilst many unique and inventive solutions have been proposed, ranging from from ion traps [10] to number of Cooper pairs on a small superconducting island [11], and even small scale demonstrations of Shor's algorithm using liquid state nuclear magnetic resonance [12], no system has been developed to an extent that fulfills the requirements set out by DiVincenzo for the realisation of a fully scalable Quantum Computer[13]. These requirements are that the proposed system:

1. is *scalable and well characterised*,
2. can be accurately placed into a *known initial state*,
3. provides the ability to *readout* the quantum state,
4. has a *long coherence time* when compared to the time taken to perform a gate operation, and
5. provides the ability to implement a *universal set of gate operations*

It is useful to use these criteria to evaluate potential QC architectures with regard to their suitability as potential QIP systems.

1.2.2 Silicon Based QC Architectures

Amongst the architectures that have been proposed, the semiconductor implementations have a number of properties that make them promising candidates. The range of proposals in this regime cover both elemental (eg silicon) and compound (eg GaAs) material systems. Numerous quantum states have been proposed as qubits, such as the number of electrons in a quantum dot [14–16], the nuclear spin state of an isotopically impure ^{29}Si atom in a spin free

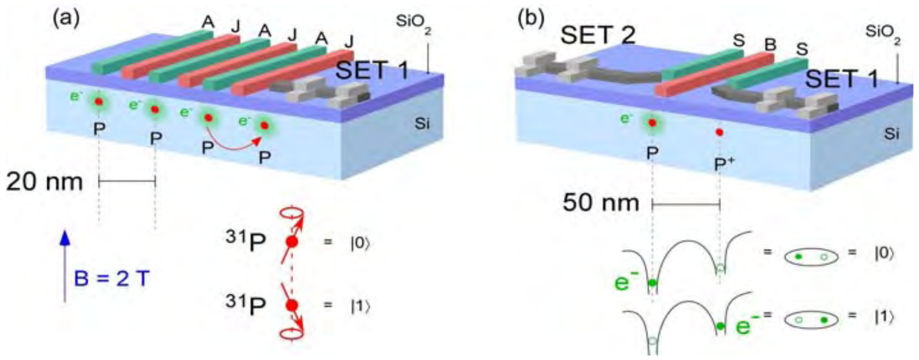

Figure 1.1: a) Schematic representation of the nuclear spin based quantum computer architecture proposed by Kane [19] and (b) the electron charge based architecture of Hollenberg *et al* [26].(Figure courtesy of V. Chan [27])

^{28}Si crystal [17] or the nuclear[18–20] and electronic [15] spin of a dopant atom in silicon or SiGe.

Benefits of a semiconductor implementation include the amount of fabrication expertise that exists due to the industrial applications of the material [21–23], the expertise in controlling both the chemical[2] and isotopic [25] purity of the constituent materials, and the ability to form high quality insulating barriers.

A typical example of a device of this type is the architecture proposed by Kane [19], which is shown schematically in figure 1.1(a). The Kane model uses the nuclear spin state of periodically arranged phosphorus donor in isotopically pure ^{28}Si as the qubits. The interaction between neighbouring qubits is provided by the the exchange interaction between the extra electron bound to each of the donors. Manipulation of the nuclear spin is achieved using electron spin resonance, the individual donors being addressed by the Stark shift of the

---

[2] For example, chemical control of the doping density in commercially available silicon is at least as good as 1 part in 10^{10} [24]

donor electron on the selected donor by surface gates aligned to each donor. The readout method proposed by Kane involved a spin to charge conversion by spin dependent tunnelling of the electron to an adjacent donor, with the position of the electron monitored with a single electron transistor.

The use of donors in silicon has the additional advantages to those that are generic to all semiconducting proposals. These include a very long nuclear spin lifetimes of at least 10 hours [28, 29]. Technologically, the availability of isotopically purified silicon with purity greater than 99.92%, which is necessary to provide the spin-less crystal, is beneficial [25], as is the ability to call on the experience gained from the use of silicon for conventional computation devices, such as the fabrication of high quality Si-SiO_2 interfaces.

A number of similar proposals use elements of the Kane architecture, but have been adapted to overcome perceived problems, such as the difficulty in implementing spin to charge conversion. An example is the charge based quantum computer proposed by Hollenberg *et al* [26]. This scheme proposes to use the position of an electron on one of two phosphorus donor atoms in silicon as the two basis states of a charge-qubit. An example of this is shown schematically in figure 1.1(b). Whilst relinquishing the benefits that come with the extremely long coherence times of the P donor nuclear spin, the readout of mechanism in this architecture should be easier as no spin to charge conversion is necessary.

The electron spin of the donor electron on phosphorus in silicon is also considered a good candidate for quantum computation [30]. This qubit has the advantage of being easier to readout than nuclear spin qubits. However, this is offset by the shorter coherence times of the electron spin, which has been measured at 3ms at 7K [31]. This however, is still much longer than the coherence times in other related structures such as coupled quantum dots in GaAs, where coherence times of 1μs are considered long [32]. Silicon also has an extremely small spin-orbit interaction [33], which allows spin to move about the device with less effect on the spin than in other, high spin-orbit materials.

It is important to note that the ability to fabricate a donor based charge or electron spin qubit is a prerequisite for the fabrication of a Kane architecture device.

1.3 Aim and Outline of the Thesis

The aim of this thesis is to investigate the spin and charge properties of phosphorus donors in silicon. If a silicon based quantum computer is to be built, it is important that the properties of the system that are important for quantum information processing be well understood. To that end, this thesis investigates the charge and spin properties of phosphorus donors in silicon.

Chapter 2 provides background information on electron spin resonance (ESR), electrically-detected magnetic resonance (EDMR) and a brief survey of methods for detecting single spins in the solid state.

Chapter 3 gives details of the experimental techniques used for both fabrication and measurement of the devices that will be used to investigate the properties of the Si:P system. This involves the use of standard micro- and nano-scale processing techniques, as well as customised fabrication and electrical measurement techniques.

Chapter 4 looks at the effect of incorporating phosphorus into silicon, particularly creation of charge defects caused by ion implantation. This is achieved through investigating the low temperature transport properties of ion implanted silicon MOSFETs. The ability to electrically incorporate donors into the silicon crystal matrix with minimum damage is critical for the fabrication of a working donor based QC.

Chapter 5 investigates the effect that different barrier dielectric material has on device performance. This is important in developing device fabrication schemes for future silicon based devices.

Chapter 6 investigates the spin dependent transport properties of ion implanted Si:P nanostructures. Electrical detection of magnetic resonance is the method used for these investigations, a technique which is shown to be sensitive enough to investigating systems with fewer than 100 donors. These results provide a pathway towards the detection of a single donor spin, which is necessary for QC.

Chapter 7 looks at the effect of isotopic purification on the same types of devices investigated in chapter 6. Isotopic purification of silicon removes the nuclear spins that normally surround donors, leading to increased coherence times.

Chapter 8 reports a proof-of-principle implementation of pulsed EDMR in an ion implanted structure. This demonstration shows that it is possible to use the standard manipulation techniques available in ESR in the EDMR regime.

Chapter 9 contains conclusions and final remarks, and is supplemented by **Appendix A** which contains initial experimental work towards a new scheme for fast timescale EDMR, which is reported here to motivate future work.

Chapter 2

Theory and Background

This chapter introduces the Zeeman and hyperfine interactions, and the effect these have on the energy level spacing of a donor electron. The theoretical end experimental background of electron spin resonance are reviewed, and the effect that electron spin resonance has on the photoconductivity of a doped semiconductor is outlined.

This chapter gives an outline of the basic principles of magnetic resonance as well as its experimental realisation. It first looks at the energy level distribution of an electron coupled to a spin 1/2 nucleus in a magnetic field. It then outlines the process involved in electron spin resonance, which enables the energy level spacings of systems to be extremely accurately determined. A method of detecting magnetic resonance via its effect on photoconductivity is then described, as this experimental technique will be utilised extensively in this thesis.

2.1 Energy Levels of an Electron in a Magnetic Field

Of fundamental importance in the study of semiconductor systems is the distribution of energy levels, as this knowledge allows the exploitation of semiconductor devices in numerous ways. For example, knowledge of the energy level distribution of dopants in semiconductors led to the development of the p-n junction diode. More complex devices, such as resonant tunneling diodes, which consist of two closely spaced tunnel barriers separating the source and drain from a quantum well, operate by allowing a current to flow only when the energy levels in the source and drain are aligned with the energy level of the well. To obtain optimal operation of such devices, it is necessary to both know the distribution of the energy levels, and be able to modify them by varying the device parameters, such as the thickness of the quantum well [22].

In the section below, the electron energy level distribution for an electron bound to a donor in the presence of a magnetic field is discussed in more detail.

The Hamiltonian of a free electron in a magnetic field due to the Zeeman interaction of the electron spin and the field is:

$$\mathcal{H}_{\mathrm{EZ}} = g_e \mu_B \mathbf{B}.\mathbf{S} \tag{2.1}$$

where $\mathbf{S}$ is the spin of the electron, g_e the electron g-factor, μ_B the Bohr magneton and $\mathbf{B}$ the magnetic field vector. The magnetic field is conventionally defined to be pointing in the z-direction ($\mathbf{B} = \{0, 0, B\}$). The eigenstates of this system are spin up, $|\uparrow_S\rangle$, and spin down, $|\downarrow_S\rangle$, which leads to:

$$E_{\mathrm{EZ}} = g_e \mu_B B S_z \tag{2.2}$$

where S_z is the magnitude of the electron spin in the z-direction which may only take the values $S_z = +1/2, -1/2$.

Additional terms of the Hamiltonian are needed when electrons are bound to nuclei which also have a spin. The first is due to the nuclear Zeeman interaction, given by:

$$\mathcal{H}_{\mathrm{NZ}} = g_n \mu_n \mathbf{B}.\mathbf{I} \tag{2.3}$$

where $g_n = 1.13$ is the nuclear g-factor, μ_n the nuclear magneton, and $\mathbf{I}$ the nuclear spin. However, this interaction is negligible when compared to the electron Zeeman interaction ($g_e \mu_B / g_n \mu_n = 3250$), and is thus ignored.

The energy of the electron is also changed due to the contact hyperfine interaction resulting from the overlap of the electron wavefunction with the nuclear wavefunction. Effectively, the electrons see the magnetic field from the nuclear spin magnetic moment, and an additional term needs to be added to the energy to account for this:

$$\mathcal{H}_{\mathrm{HF}} = A\mathbf{S}.\mathbf{I} \tag{2.4}$$

where A is the magnitude of the hyperfine coupling, $\mathbf{I}$ is the nuclear spin. A is found by determining the overlap of the electron and nuclear wavefunction[34]:

$$A = \frac{8\pi}{3}(g_n.\mu_n).(g_e.\mu_B).|\psi_{\mathrm{electron}}(0)|^2 \tag{2.5}$$

where $\psi_{\mathrm{electron}}(x)$ is the electron wavefunction. Thus, the Hamiltonian of the system is given by:

$$\mathcal{H} = \mathcal{H}_{\mathrm{EZ}} + \mathcal{H}_{\mathrm{HF}} = g_e \mu_B \mathbf{B}.\mathbf{S} + A\mathbf{S}.\mathbf{I} \tag{2.6}$$

The basis states of the electron-nucleus spin pair are defined to be the four possible projections of the nuclear and electron spin doublet onto the z-direction

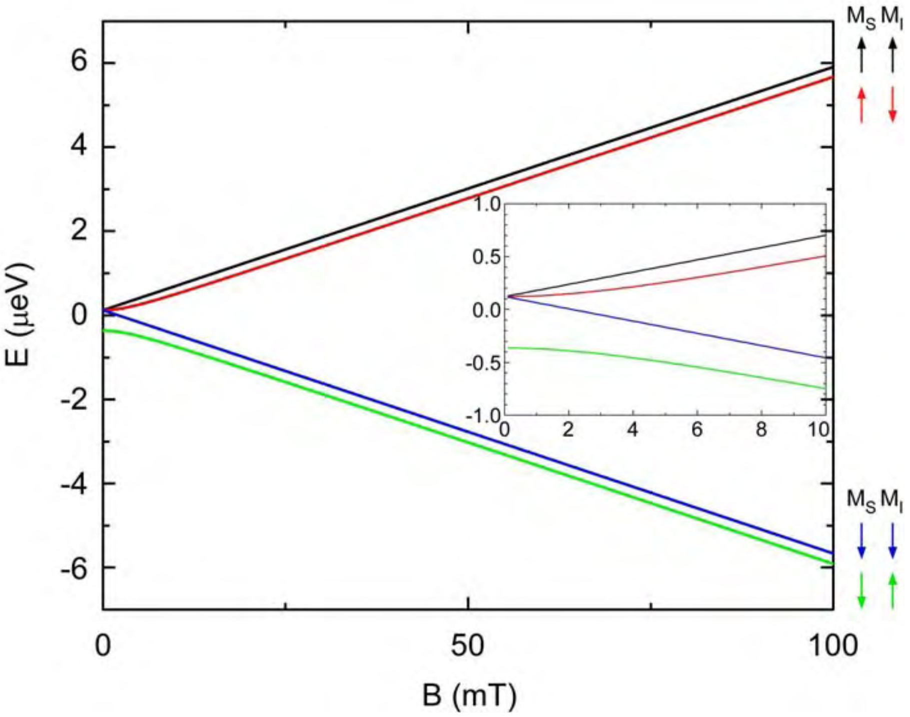

Figure 2.1: Energy levels for a spin 1/2 electron donor on a spin 1/2 Nucleus. The inset shows the deviation from the linear Zeeman splitting at low field where the hyperfine interaction and the Zeeman interaction have a similar magnitude.

in the absence of any interaction:

$|\uparrow_S, \uparrow_I\rangle, |\uparrow_S, \downarrow_I\rangle, |\downarrow_S, \uparrow_I\rangle, |\downarrow_S, \downarrow_I\rangle$.

The eigenstates of this system are [35, 36]:

$$\psi_1 = |\uparrow_S, \uparrow_I\rangle \tag{2.7}$$

$$\psi_2 = \alpha|\uparrow_S, \downarrow_I\rangle + \gamma|\downarrow_S, \uparrow_I\rangle \tag{2.8}$$

$$\psi_3 = |\downarrow_S, \downarrow_I\rangle \tag{2.9}$$

$$\psi_4 = \alpha|\uparrow_S, \downarrow_I\rangle - \gamma|\downarrow_S, \uparrow_I\rangle \tag{2.10}$$

where [35]:

$$\alpha = \left\{1 + \left[\frac{g\mu_B B}{A} - \sqrt{1 + \frac{(g\mu_B B)^2}{A^2}}\right]^2\right\}^{-1/2} \tag{2.11}$$

$$\gamma = \left\{1 + \left[\frac{g\mu_B B}{A} - \sqrt{1 + \frac{(g\mu_B B)^2}{A^2}}\right]^{-2}\right\}^{-1/2} \tag{2.12}$$

In the high field limit, $g\mu_B B \gg A$, $\alpha \rightarrow 1$ and $\gamma \rightarrow 0$, and the basis states become the eigenstates. In effect, the Zeeman interaction dominates over the hyperfine interaction, and the two spins are effectively uncoupled. When $B = 0$, $\alpha = \gamma = \frac{1}{\sqrt{2}}$. In this limit, there are three triplet (total spin $\mathbf{F} = \mathbf{S} + \mathbf{I} = 1$) states:

$$\psi_1 = |\uparrow_S, \uparrow_I\rangle \tag{2.13}$$

$$\psi_2 = \frac{1}{\sqrt{2}}(|\uparrow_S, \downarrow_I\rangle + |\downarrow_S, \uparrow_I\rangle) \tag{2.14}$$

$$\psi_3 = |\downarrow_S, \downarrow_I\rangle \tag{2.15}$$

and one singlet ($\mathbf{F} = 0$) state:

$$\psi_4 = \frac{1}{\sqrt{2}}(|\downarrow_S, \uparrow_I\rangle - |\uparrow_S, \downarrow_I\rangle) \tag{2.16}$$

At $B = 0$, the energy of the three triplets, $E_1 = E_2 = E_3 = A$, and the energy of the singlet, $E_4 = -3A$, where A is the hyperfine coupling constant. However, in this thesis all resonance experiments will be performed in the high field limit ($B \sim 300mT$, $g\mu_B B/A \sim 70$) where the Zeeman energy dominates, and the energy of the levels is:

$$
\begin{aligned}
E_1 &= g\mu_B B + A && (2.17) \\
E_2 &= g\mu_B B - A && (2.18) \\
E_3 &= -g\mu_B B + A && (2.19) \\
E_4 &= -g\mu_B B - A && (2.20)
\end{aligned}
$$

The energy distribution as a function of magnetic field for the donor electron on a P donor (with nuclear spin 1/2) in silicon is shown in figure 2.1.

2.2 Introduction to Electron Spin Resonance

This section provides an introduction to electron spin resonance, following those given in references [35],[37] and [38]. First, the energy level structure determined in the previous section is used to determine the requirements for ESR regarding the energy and selection rules of ESR transitions. This section, which uses an approach based on the resonant absorbtion of microwave photons, allows the expected resonance spectra to be easily determined. Later, the phenomenological approach to ESR, which involves solving the Bloch equations [39] for the classical motion of magnetization in a magnetic field, is outlined. This approach treats the microwave photons as an oscillating magnetic field, and has the advantages of allowing greater understanding of the dynamics of the spin system due to the resonant excitation, as opposed to the spectra that results from the system being measured.

2.2.1 Photon energy

ESR uses the resonant absorbtion of photons to experimentally determine the energy level spacings. Usually, the sample is irradiated with microwaves of a fixed frequency, f. If the energy of the photons:

$$E = hf \tag{2.21}$$

is identical to the energy level separation of the system then an increase in the absorbtion of microwaves by the sample will be observed. However, whilst it is necessary for the photon energy to equal the energy level spacing, this in itself is not the complete requirement for ESR. There exist further selection rules based on the quantum properties of the system that determine the actual allowed transitions, and these are discussed below.

2.2.2 Selection Rules for Allowed Transitions

Spin is a conserved quantum number. As a result, any transitions involved with ESR must conserve spin. The resonant absorbtion (or induced emission) of a photon with spin 1 can only have a change in spin, $\Delta M = \pm 1$. Figure 2.2 shows the change in spin for transitions between the four eigenstates of the P donor in silicon in the high field limit. The allowed transitions for electron spin resonance, $\Delta M_S = \Delta M = \pm 1$, are shown by the green arrows. Corresponding nuclear magnetic resonance transitions, which are due to changes in the nuclear spin state, $\Delta M_I = \Delta M = \pm 1$, are indicated by the blue transitions.

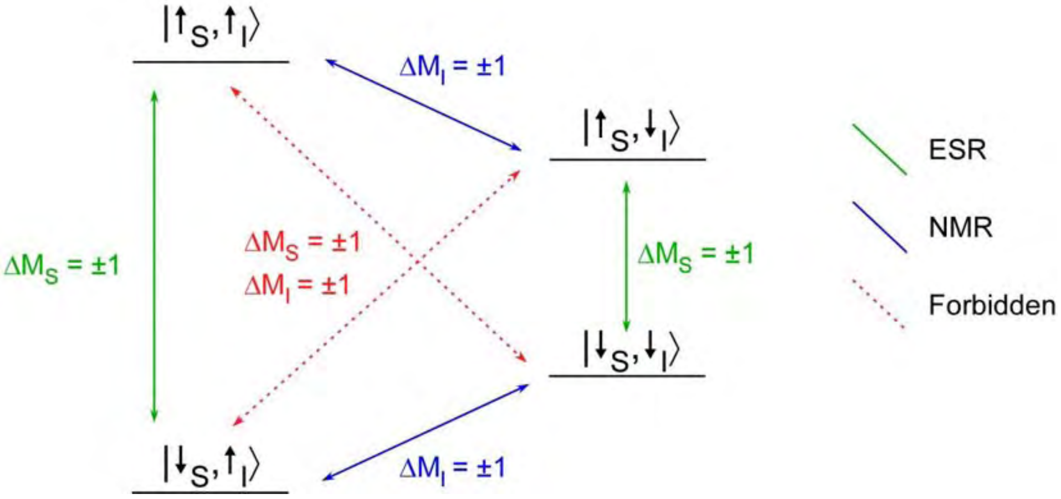

Figure 2.2: Schematic representation of the allowed ESR transitions between the four spin eigenstates of the P donor in Si in the high field limit.

Transitions involving a simultaneous change in both the nuclear and electron spin are forbidden ($\Delta M_S = \Delta M_I = \pm 1, \Delta M = 0, \pm 2$)

To observe ESR experimentally, a sample is usually placed in a resonant circuit (eg a resonating cavity) and a quasi-static (DC) magnetic field applied. Microwaves are applied to the cavity at a fixed frequency. The quasi-static magnetic field is swept slowly, and any change in the absorbtion or dispersion circuit (due to the sample) is recorded. Since such a change will only occur when the resonance condition of the are met, and the spin system is able to absorb and dissipate the microwave power, the absorbtion spectra indicates that the energy level spacing of the system is identical to the energy of the applied microwaves.

Figure 2.3 shows the energy level spacing and spin configuration for Si:P at $B \sim 300$mT. The selection rules for transitions allow only transitions between states ($| \downarrow_S, \uparrow_I \rangle$and $| \uparrow_S, \uparrow_I \rangle$) and ($| \downarrow_S, \downarrow_I \rangle$and $| \uparrow_S, \downarrow_I \rangle$). At a fixed microwave energy (frequency), in this case $38.2\mu\ eV$(9.23GHz), there is only one magnetic field that satisfies $\Delta E = hf$ for each transition. The spectrum expected for this system is thus two absorption peaks spaced by 4.2mT, shown in figure 2.3b.

To allow greater sensitivity, the DC magnetic field can be modulated and the change in absorbtion of the cavity monitored by a lockin technique[40, 41]. This results in the measurement of the change in absorbtion, dA/dB, which is shown schematically in figure 2.3c.

Whilst it was necessary to consider the presence of the nuclear spin in determining the energy level structure, this section has shown that, in the high field limit in ESR, only changes in the electron spin are observed. In the remainder of the treatment of ESR, the nuclear spin component of the eigenstate will be neglected, and discussion limited to the changes in the electronic spin.

2.2.3 Transition Probabilities and Detection of ESR

The probability for a transition from $|\downarrow\rangle$to $|\uparrow\rangle$(resonant absorption), $W_{\downarrow\Rightarrow\uparrow}$, is equal to the probability of a transition from $|\uparrow\rangle$to $|\downarrow\rangle$(induced emmission), $W_{\uparrow\Rightarrow\downarrow}$. In ESR, this probability is given by:

$$W_{EPR} = \frac{1}{4}(\frac{-g\mu_B}{\hbar})^2 B_1^2 g(\nu) \tag{2.22}$$

where B_1 is the magnitude of the oscillating magnetic field perpendicular to B_z and $g(\nu)$ is a form function for the transition, which is normalised by:

$$\int_0^\infty g(\nu)d\nu = 1 \tag{2.23}$$

If the occupation of $|\uparrow\rangle$and $|\downarrow\rangle$were equal, then no energy could be transfered to the spin system. However, the energy level seperation caused by the application of a magnetic field gives rise to a Boltzmann distribution of elec-

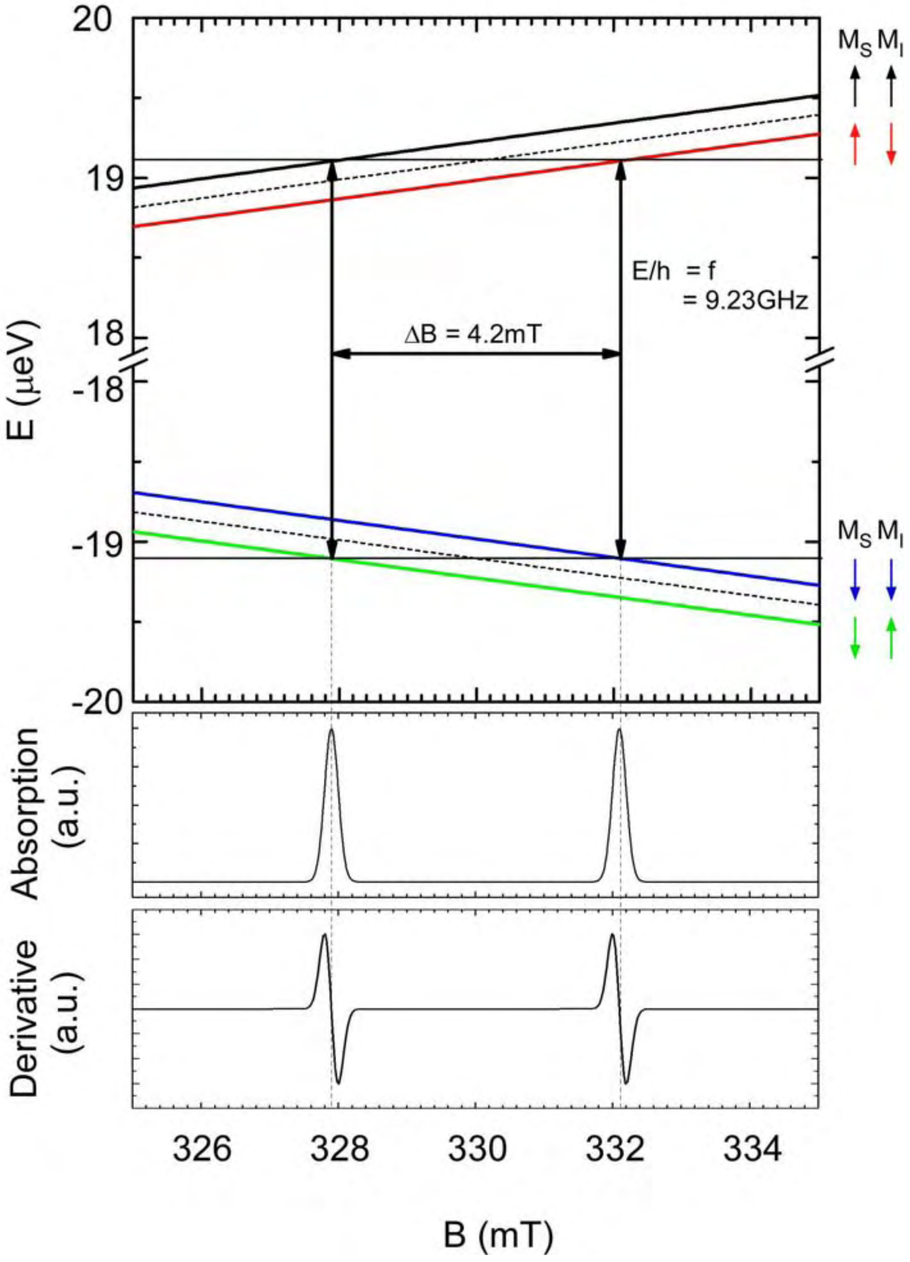

Figure 2.3: Energy levels for a spin 1/2 electron on a spin 1/2 nucleus showing the two resonances for a fixed microwave frequency.

trons in the two levels. This polarisation gives rise to a net absorbtion in the spin system.

This polarisation need not be very large for ESR to be observed. Considering the electron bound to P in Si at 4.2K, with an applied magnetic field of 330mT (a common experimental regime), then the polarisation of the system $P = \frac{N_{|\uparrow\rangle} - N_{|\downarrow\rangle}}{N_{|\uparrow\rangle}} = 0.053$, which indicates that only approximately 3 in 100 spins are oriented differently than they would be if the system was unpolarised.

In the absence of any other dissipation method, as the spins absorb the resonant microwaves the population will move towards equality, at which point net absorbtion will vanish and the ESR signal become unmeasureable. However, realistic physical systems have a variety of other dissipation methods, usually involving inelastic spin scattering with the phonon bath, that allow relaxation from the excited to the ground states, allowing a polarised equilibrium population distribution to form. The effect of this dissipation on the dynamics of the spin system is discussed later in the next section.

2.3 Bloch Formalism

Whilst it is relatively simple to determine the ESR spectra that will result using the method outlined above, little information is gained about the dynamics of the spin system under ERS conditions. In this section, the phenomenological Bloch equations are introduced, following the outline in references [37] and [38].

By considering the spin system as an ensemble of magnetic moments, Bloch [39] showed that the equation of motion of a free spin system was given by:

$$\frac{d\mathbf{M}}{dt} = \frac{-g\mu_B}{\hbar}(\mathbf{M} \times \mathbf{B}) \tag{2.24}$$

where **M** is the net magnetization of the ensemble of spins. The net magnetization is related to the expectation value of the spin system by $\mathbf{M}_S = -g\mu_B\langle\mathbf{S}\rangle$.

In the case with the magnetic field in the z-direction and the spin in either of the two basis states ($|\uparrow\rangle$or $|\downarrow\rangle$), the magnetization is found to precess around the magnetic field vector with frequency $\omega_{\mathrm{L}} = g\mu_B B_0/\hbar$, the Larmor frequency.

The effect of the application of microwave radiation can be considered by the addition of a small oscillating component to the magnetic field, perpendicular to the static field. The magnetic field vector becomes $\mathbf{B} = B_0\mathbf{z} + B_1(t)\mathbf{x}$. In the laboratory frame, the microwave field can be considered as the combination of two circularly polarised fields rotating about the z-axis:

$$\mathbf{B}(t) = \begin{pmatrix} B_1\cos(\omega t) \\ B_1\sin(\omega t) \\ 0 \end{pmatrix} + \begin{pmatrix} B_1\cos(\omega t) \\ -B_1\sin(\omega t) \\ 0 \end{pmatrix} \tag{2.25}$$

By recasting the reference frame to be rotating about the z-axis at the microwave frequency (the rotating frame approximation), the microwave field becomes:

$$\mathbf{B}_{eff} = \begin{pmatrix} B_1 \\ 0 \\ B_0 + (\frac{\omega}{-g\mu_B/\hbar}) \end{pmatrix} \tag{2.26}$$

where $\mathbf{B}_{eff}$ is the effective magnetic field and ω the frequency of the applied microwaves, and neglecting the component rotating at -2ω as it has no

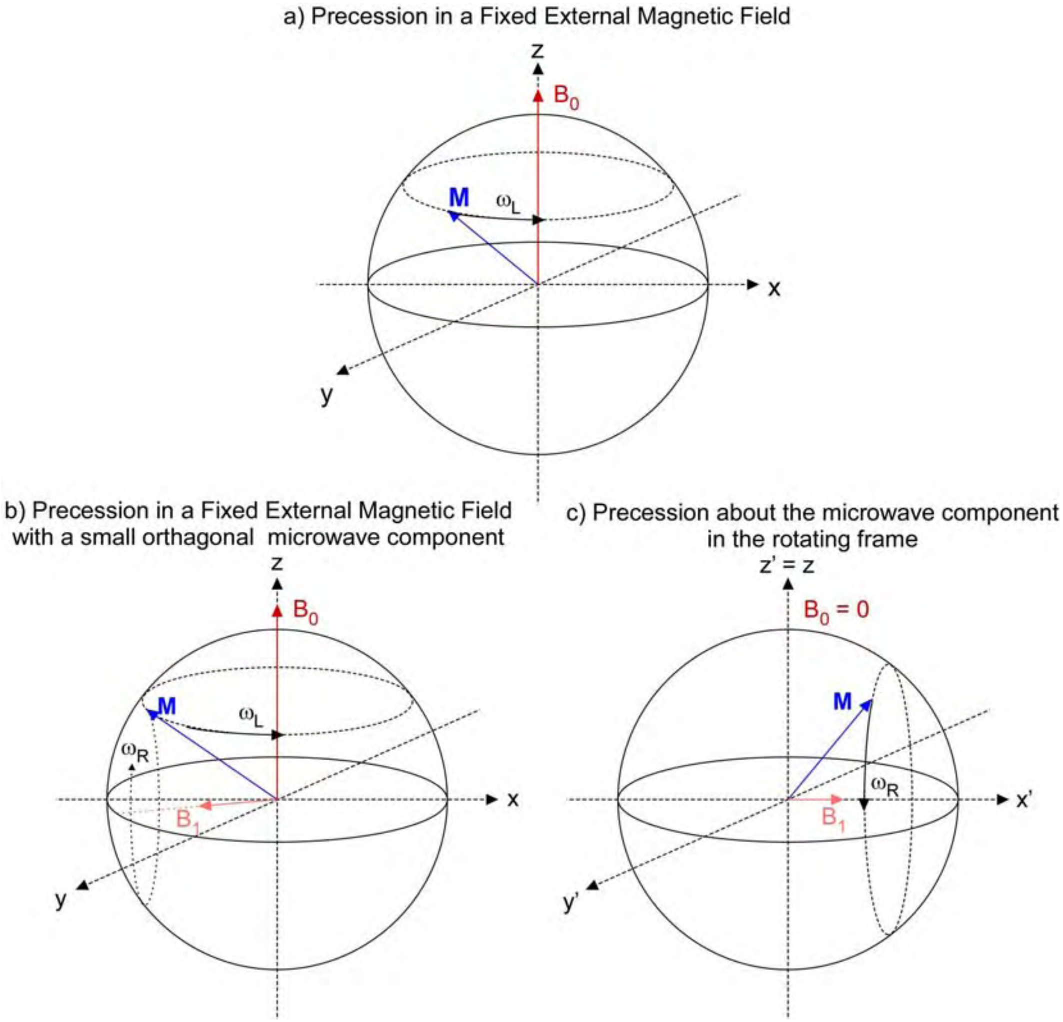

Figure 2.4: Motion of the net magnetization vector with a variety of different applied magnetic fields: a) in the presence of a fixed magnetic field, b) in the presence of a fixed magnetic field with an orthogonal microwave field, and c) with the reference frame rotating with frequency w_L with respect to the laboratory frame.

noticable effect on the spin system [37].

Following the adoption of the rotating frame, the dynamics of the spin system are given by:

$$\frac{d\mathbf{M}'}{dt} = \frac{-g\mu_B}{\hbar}(\mathbf{M}' \times \mathbf{B}_{eff}) \tag{2.27}$$

where $\mathbf{M}'$ is the magnetization in the rotating frame.

When the microwave frequency is equal to the Larmor frequency, $B_z = 0$, and no precession of the magnetization about the z-axis is observed. The presence of a fixed magnetic field, B_1 in the x' -direction results in the precession of $\mathbf{M}'$ about the x' axis with frequency $\omega_\mathrm{R} = g\mu_B B_1/\hbar$, the Rabi frequency. It is this precession which results in the oscillations of the spin (magnetization) between $|\uparrow\rangle$and $|\downarrow\rangle$.

It is useful to now introduce the two relaxation times, T_1 and T_2. T_1, the longitudinal relaxation time, is the time taken for the z-component of the magnetization to return to thermal equilibrium after being disturbed. T_2, the transverse relaxation time, is the characteristic time for the transverse magnetization to return to zero. When these times are included into the Bloch equations, the equations of motion become:

$$\begin{aligned}
\frac{\partial\, M_x}{\partial\, t} &= \frac{-g\mu_B}{\hbar}(M_x \times B_x) - \frac{M_x}{T_2} && (2.28)\\
\frac{\partial\, M_y}{\partial\, t} &= \frac{-g\mu_B}{\hbar}(M_y \times B_y) - \frac{M_y}{T_2} && (2.29)\\
\frac{\partial\, M_z}{\partial\, t} &= \frac{-g\mu_B}{\hbar}(M_z \times B_z) - \frac{M_z - M_z^0}{T_1} && (2.30)
\end{aligned}$$

where M_z^0 is the equilibrium magnetiation in the z-direction when no microwaves are applied.

It is illustrative to consider what will happen when a microwave pulse is applied for just enough time for the magnetization to move to the x′-y′ plane (a $\pi/2$-pulse). Following the microwave pulse, the magnetization will begin to precess about the (now non-rotating frame) x - y plane with frequency ω_L. In this case, T_2 is the characteristic time for the magnetization in the x - y plane to return to zero. T_1 processes, which change the energy of the system, may only be inelastic, whereas T_2 processes, which do not change the energy, can be either elastic or inelastic. As a result, T_2 is usually much shorter than T_1 in semiconductor systems. For example, experimental observation of the relaxation times in isotopically purified ^{28}Si doped with 10^{16}P/cm^{-3} gives $T_1 \sim 100ms$ and $T_2 \sim 25\mu\ s$ [31]. As the density of donors is reduced, the (elastic) dipolar coupling between spins is reduced, leading to longer T_2 times. In systems with donor densities of 10^{15}P/cm^{-3}, $T_2 \sim$ 3ms [31].

2.4 Experimental Electron Spin Resonance

Electron spin resonance was first observed experimentally in an iron compound by Zavoisky in 1945[42]. It was also observed soon after by Cummerow and Halliday in the manganous salts $MnSO_4.4H_2O$ and $MnCl_2.4H_2O$ [43]. The first measurement of ESR of donors in silicon (in this case As and P) was reported by Fletcher *et al* [44] in 1954. They observed the resonance of both arsenic and phosphorus doped silicon at low temperature, and were able to determine the hyperfine splitting, 7.2 mT and 4.2 mT respectively.

The most significant early contributions to the ESR studies of donors in silicon were made by Feher in the mid to late 1950's. [28, 45–49]. These include a method to determine the donor electron wavefunction using electron nuclear double resonance (ENDOR) on Si:P [50], investigation of the coherence times of donor electrons as a function of donor density [51], and a method to polarise the nuclear spin of the P donors via ESR [52], all of which are directly relevant to the nuclear spin QC discussed in section 1.2.2.

More recently, investigations of the temperature dependence of the coherence times of the P donor electron in silicon have been undertaken, showing T_2 of up to 3ms at 7K in low doped isotopically purified ^{28}Si. Also, investigation of the effect of isotopic purification have been undertaken, showing that the coherence time increases as $1/f^{0.86}$, where f is the fraction of ^{29}Si present [53, 54].

2.5 Detecting Small Numbers of Spins

Whilst ESR is a remarkably useful tool for investigating the properties of large ensembles of spins, it has limitations when the number of spins to be investigated is small. The number of spins that can be detected by standard ESR is generally considered to be limited to $\sim 10^9$[40, 55].

Clearly, if the aim, as in quantum computing, is to manipulate and detect the spin state of single spins, this technique will be of little value. However, the precision with which spins can be manipulated by ESR make it a difficult technique to discount.

One way to overcome the number limitation is to use ESR to manipulate the spins, but to use another method to detect the spin state. Koppens *et al* [56] have demonstrated ESR manipulation of a single spin in one of two coupled GaAs quantum dots. These dots are tuned so that the different spin states at the Fermi energy of two coupled dots are opposite, leading to blockade of electron transport through the dots. By flipping the spin of the electron in one of the dots, a detectable current is able to flow. Rugger *et al* [57] have used Magnetic Resonance Force Microscopy (MRFM) to detect the spin of a single E' defect in $\mathrm{SiO_2}$. Xiao *et al* [58] have detected the spin of a single paramagnetic trap in a small ($\sim 0.3 \times 0.24 \mu m^2$) MOSFET by its effect on the conductivity of the device, again using ESR to manipulate the spin. The concept of independent manipulation and readout can also be extended to manipulation methods. For example, Yang *et al* [59]have used photoluminescence excitation spectroscopy to to manipulate the P donor electron spins in isotopically purified ^{28}Si , with readout via the change in conductivity of the samples.

In the next section, the detection of ESR by its effect on the photoconductivity of a sample is discussed in detail. This technique, generally referred to as Electrically Detected Magnetic Resonance, will form the basis of the experimental work reported in later chapters.

2.6 Electrically Detected Magnetic Resonance

In 1966, Schmidt and Solomon [60] first demonstrated the detection of ESR by its effect on the electrically conductivity of a sample. They noted that the photoconductivity of Si:P with $[P] = 5 \times 10^{13}\mathrm{cm}^{-3}$ changed when the resonance conditions of the P donor electron was satisfied. They claimed a sensitive of at least 10^8 spins, well below that possible with conventional ESR, based on their ability to detect the small number of exchange coupled P pairs expected at this doping density [61].

Subsequent studies of P in crystalline Si (c-Si) using EDMR were performed both at very high [62] and very low magnetic fields[63], as well as of P in amorphous[64] (a-Si) and microcrystalline[65] (μc-Si) silicon. Electrical detection of electron-nuclear double resonance (EDENDOR)[66] has been also been demonstrated on Si:P.

Attempts to reduce the number of donors in a sample for EDMR have been reported. Kawachi *et al* [67] were able to observe EDMR from about 10^4 dangling bond defects in micron-size a-Si thin-film transistors. Stich *et al* [66] reported successful detection of EDMR in Si:P samples containing as few as 10^6 donors, by using a focused laser beam to restrict the area of the sample that was illumination.

The study of Si:P via EDMR has previously been reported in samples with bulk doping [60, 63, 66]. For example, Stich *et al* [63] have shown that EDMR of Si:P is possible at radio frequencies ($f = 280$MHz). This allowed them to determine that the observed EDMR signal was independent of the magnetic field, supporting a spin independent pair formation model for EDMR (This is discussed in more detail below).

EDMR of samples with very high dose (metallic) implants [68] with no photoexcitation have shown that the EDMR signal in these sample is a strong function of the doping density, with the change in conductivity $\Delta\ I/I$ decreasing from 10^{-7} at $[P] = 6 \times 10^{18}$ cm^{-3} to $\lesssim 10^{-10}$ at $[P] = 3 \times 10^{19} cm^{-3}$.

EDMR has been used to investigate the hyperfine interaction of P in highly strained silicon [69]. The effect of strain on the donor wavefunction is relevant to QIP, as it has been proposed as a solution to possible problems related to the oscillating strength of the exchange interaction between neighbouring donors [70, 71]. To achieve high strain, an Si:P epilayer was grown on a SiGe substrate. EDMR was used to detect the ESR spectra due to the high sensitivity to the small number of donors in the epilayer.

A good review of EDMR is given in reference [72].However, no reports of the EDMR of low density (non-metallic) implants are know to the author.

The first attempt to explain the mechanism for the observed change in the photocurrent was by Lepine [73], and is outlined below.

The Lepine Model

Lepine [73] proposed that free electrons in the conduction band recombine to form singlet or triplet states with bound electrons on recombination centers, and that the triplet state was only weakly bound (shown schematically in figure 2.5a). This leaves the singlet state as the only possible end state from which one of the bound electrons is able to recombine with a hole from the valance band (Figure 2.5b). In a magnetic field, there are more spin down electrons than spin up, resulting in an increased probability of triplet formation. ESR will cause a move towards an unpolarised system, resulting in more singlet formation and thus more recombination. This decrease in the carrier density leads to a decrease in the current of the system.

The capture cross section for the conduction electrons is given by:

$$\Sigma = \Sigma_{\circ}(1 - pP) \tag{2.31}$$

where p and P are the spin polarisations of the conduction electrons and recombination centre electrons respectively, and $\Sigma_{\circ}$ the spin independent capture cross section.

The recombination time, τ, of the conduction electrons is related to the capture cross section and to the first order, a change in the capture cross section:

$$\Delta\Sigma/\Sigma = -\Delta\tau/\tau \tag{2.32}$$

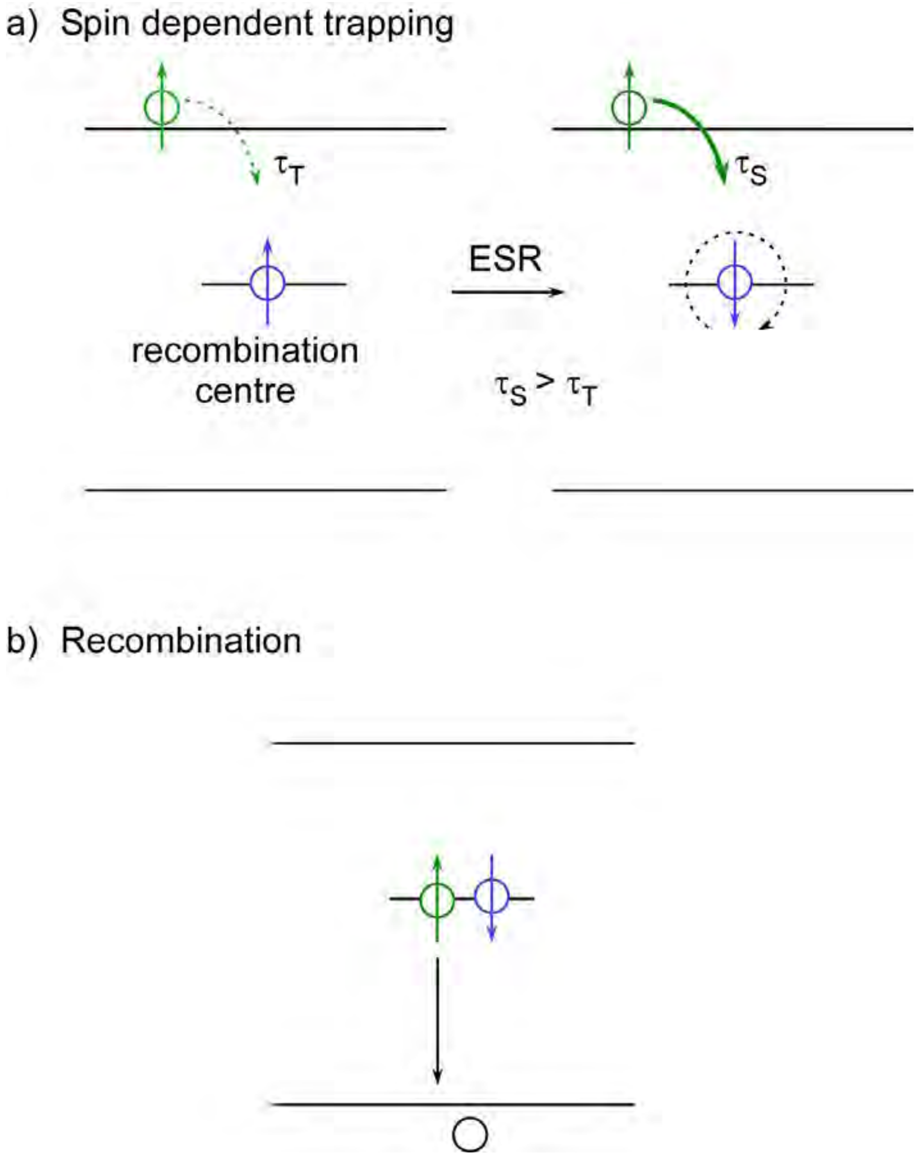

Figure 2.5: Schematic of the spin dependent recombination process proposed by Lepine.

The steady state number of photoexcited electrons in the conduction band,

$$n_{photo} = G\tau \tag{2.33}$$

where G is the photocarrier generation rate.

The transient behaviour of the carrier number is described by:

$$\frac{dn}{dt} = G - \frac{\Delta\, n}{\tau} \tag{2.34}$$

Since the photoconductivity is related to the excess number of photocarriers, $\Delta\sigma = \Delta\, ne\mu$, any change in the recombination cross section will lead to a change in the number of photocarriers and hence the photoconductivity.

The polarisation can be changed by ESR, which serves to move the spin populations towards equality. In the limit of no polarisation, the change in the current is proportional to the product of the original polarisations; for system with a g-factor of 2 at 300mT, $pP \sim 10^{-6}$ at 300K, increasing to $\sim 10^{-3}$ at 5K.

According to this model, the change in conductivity should be proportional to $(B/T)^2$. However, in low magnetic field experiments by Stich *et al* [63] and Greulich-Weber *et al* [74], this dependence is not observed experimentally. Also, the change in the conductivity should be limited to $\Delta\sigma/\sigma \sim pP \sim 10^{-6}$ for $g = 2$ species in x-band measurements, which disagrees with measurements showing $\Delta\sigma/\sigma > 10^{-3}$ in a-Si[75].

The Kaplan, Solomon and Mott Model

An improvement to this model was made by Kaplan, Solomon and Mott (KSM), who proposed that the initial formation of pairs was not spin dependent. The conduction electron would become bound to the recombination centre, and would then recombine to a ground state depending on the spin configuration of the two electrons (effectively, only spin pairs in a singlet configuration would be allowed to recombine). Only after recombination would it be possible for one of these electrons to then recombine with a hole.

The difference in this model is that only the two electrons on a particular recombination centre are involved in a spin dependent process. For the either member of the pair to become involved in a process with any other electron, the pair must first dissociate and a new pair form.

This model allows a spin dependent process with no polarisation of the spin ensemble, as each of the two constituents of the spin pair are by definition fully polarised.

Figure 2.6 shows a schematic representation of four parts of EDMR using the KSM model, with P doped silicon as the model system. The recombination centre is the mid-gap P_b defect level. a) The initial formation of a spin pairs, which is independent of the spin of each of the two spins. One of the two electrons is bound to the P donor and one is bound to the P_b defect. b) Manipulation of one of the spins via ESR, as discussed earlier in this chapter. Either of the spins can be manipulated, as both contribute to the probability that the pair can form a singlet. c) Spin dependent formation of the two electron singlet, $|\uparrow\downarrow\rangle$, on the defect site. The probability of this formation is the related to the probability that the electrons will form a singlet state, $P_1 \propto |\langle S|\psi_{pair}\rangle|^2$. d) Recombination of one of the singlet electrons with a hole, and formation of a new spin pair by the (spin independent) recombination of a conduction band electron into a bound P donor state.

Since this model does not require spin dependent pair formation, the change in current is not dependent on the polarisation of the spin ensembles, but instead the relative orientations of the two spins in the pair. This allows a larger current change than that allowed by the Lepine model, in line with experimen-

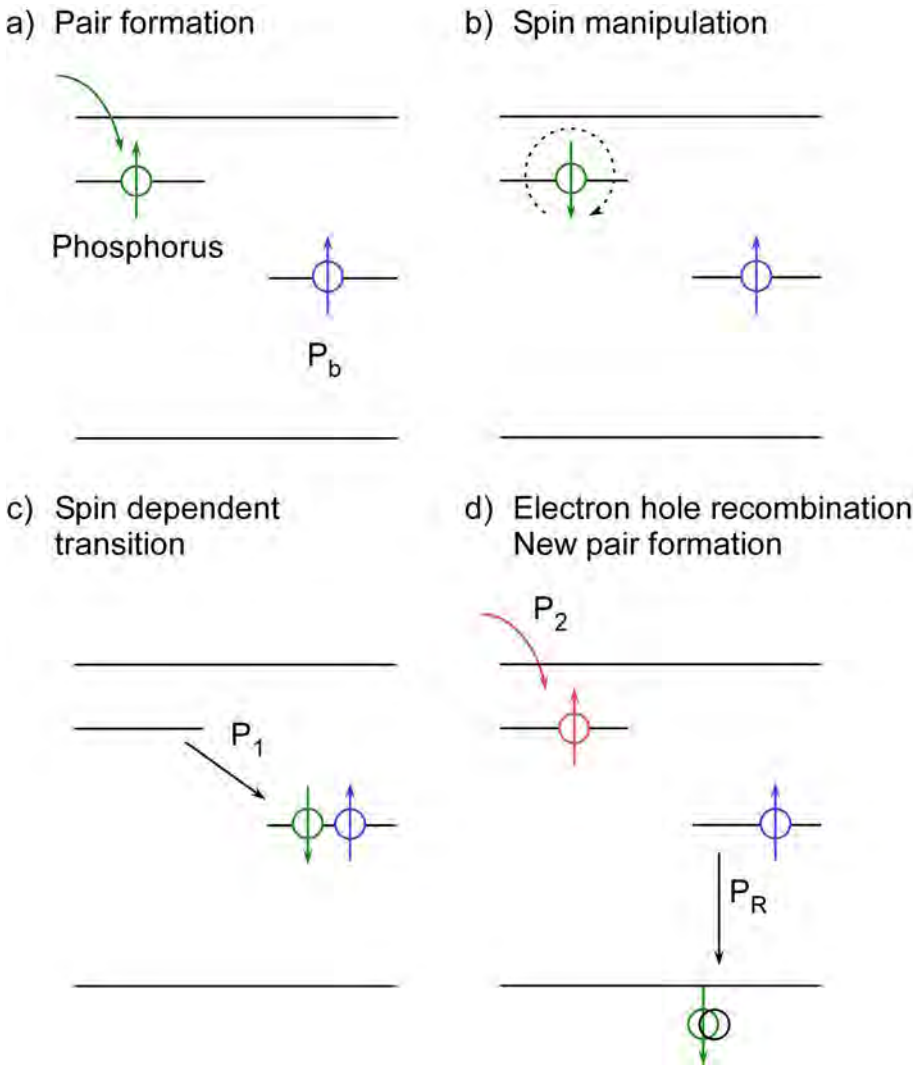

Figure 2.6: Schematic of the four different stages in EDMR using the KSM model of spin dependent recombination. The stages are discussed in detail in the text.

tal results in a-Si discussed above[75].

In the next section, the temporal evolution of this model is discussed, in the case of pulsed EDMR.

2.6.1 Pulsed - Electrically Detected Magnetic Resonance

Of interest due to possible future applications is the work of Boehme and Lips [76] on the electrical detection of pulsed ESR. This technique uses the time resolved current transients due to recombination of electrons to probe the spin dynamics of the systems. The recombination pathway for the model system Si:P, as for the KSM model, is shown in figure 2.6. Under cw-ESR, a steady state equilibrium will result in a fixed change in the current. However, following the application of a short microwave pulse, a complex current transient results due to several recombination processes with different time constants. For simplicity, a system comprising only P-P_b electron pairs in a singlet or triplet configuration will be considered. The recombination probability for the singlet pairs is much higher than the triplet pairs, resulting in a steady state excess of triplet pair states. Using a π-pulse applied to the P-electron as an example, the the triplet and singlet population densities will be swapped. The increase in singlet content will lead to an increase in recombination, whereas an increase in triplet content will lead to a decrease in recombination. Initially, the now larger singlet population will lead to an increase in population. However, this will return to its steady state value faster than the triplet population. This difference in recombination rate allows a period of decreased recombination to be observed, until the triplet population also returns to its steady state value. To summarise, following a microwave pulse, the photocurrent is seen to decrease (increased recombination), then increase (decreased recombination) then return to its steady state value, due to the different recombination probabilities of the singlet and triplet spin pair configurations.

The ability to observe the current transient in real time provides information about the different recombination processes that occur ion the sample. Also, by varying the microwave pulse length, the dynamic evolution of the spins can be observed by monitoring the resulting current transient. This can be used to observe driven Rabi oscillations of the electron spin, as has recently been demonstrated on Si:P [77]. The ability to electrically detect the coherent spin motion of donor electrons makes this technique an important tool for the investigation of the spin properties of materials, such as Si:P, proposed for use in solid state QIP devices.

2.7 Summary

In this chapter, the spin and energy eigenstates of a spin 1/2 electron bound to a spin 1/2 nucleus in a magnetic field has been determined. By invoking conservation of spin, selection rules for the allowed transitions between spin states in the high magnetic field limit were formulated. These two properties were used to determine the spectra that would be expected in electron spin resonance experiments on such a system. The dynamic evolution of the spin system was discussed using the phenomenological Bloch equations, which led to the introduction of the longitudinal and transverse relaxation times, T_1 and T_2 respectively.

An experimental and theoretical overview of electrically detected magnetic resonance was given, as this technique will be used throughout this thesis. Also, the temporal evolution of the EDMR signal due to pulsed EDMR was outlined, as this will be necessary in chapter 8.

Chapter 3

Experimental Methods

This chapter gives details of the device fabrication and measurement methods used in the work presented in this thesis.

The majority of the fabrication of the devices used in this thesis was carried out in the Semiconductor Nanofabrication Facility (SNF) at the University of New South Wales (UNSW). This facility contains a large array of semiconductor fabrication equipment including ultraclean furnaces, optical photolithography tools, SEM and EBL tools, evaporators, test and support equipment, all housed in a class 3.5 clean room.

Ion implantation was performed by Dr Jeffery McCallum from the University of Melbourne, using ion implanters at the Australian National University.

Measurements reported in chapters 4 and 5 and Appendix A were undertaken in the National Magnet Laboratory (NML) at UNSW . This facility allows measurements to 50mK at fields of up to 10T. Those measurements reported in chapters 6 and 7 were undertaken by the author at the Walter Schottky Institute, Technische Universität München, Germany.

3.1 Fabrication

This section focus on the process details and equipment used for fabrication of devices. Details of the devices are included in the chapters reporting the experimental results, due to the number of different devices investigated. A good reference for more details of micron-scale processing can be found in the books by Sze [22, 78], and a comprehensive overview of electron beam lithography in Chapter 2 of the SPIE Handbook of Microlithography, Micromachining and Microfabrication [79].

3.1.1 Micron-scale Processing

Wafer Cleaning

All wafer were cleaned prior to fabrication and where necessary throughout the fabrication process. Cleaning involved submersing the wafer in SP (Sulphuric acid : Hydrogen Peroxide, 3:1) for 10 minutes, followed by a 10 minute rinse in deionised (DI) H_2O, a ten minute clean in RCA2 solution (DI H_2O 170mL, Hydrochloric Acid 30mL and Hydrogen Peroxide 30mL) and a final ten minute DI H_2O rinse. Also, the first clean of a new wafer involved a final 10 second dip in Hydrofluoric Acid to remove the native oxide.

Optical Lithography

Optical lithography was undertaken using chromium masks designed by the author, using AZ 6112 photoresist (Microchem) for positive lithography and AZ 5214E resist for negative lithography. Two lithography tool, a Quintel 404 and a Quintel 6000, were used. Exposure energies of approximately 15 $\mathrm{mJ/cm^2}$ were able to provide high resolution lithography results, with features of order

1 micron possible. Development was performed by soaking in AZ 300 MIF developer for 60 s, followed by rinsing in DI H_2O.

Thermal Oxides

For the growth of critical oxides, a triple walled furnace was used. The triple walled furnace has a gas flow between the walls of the furnace to limit the diffusion of impurities into the furnace, resulting in a higher quality oxide. For a similar reason, the operating temperature of this furnace is also kept low, resulting in slower oxide growth. To reduce fabrication times, a second single walled furnace with a higher operating temperature was used for the growth of thick, non-critical oxides, such as those used for diffusion masking.

In the single walled furnace, oxides were grown at 1000°C in an oxygen ambient that had been passed through a DI H_2O bubbler; in the triple walled furnace, oxides were grown at 800°C in an atmosphere of Oxygen and DCE.

The quality of the resulting oxide is discussed in detail in chapter 4.

Dopant Diffusion

Diffusion at 950°C for 30 minutes using a ceramic solid-source of phosphorus (P1025, Saint-Gobain Ceramics[1]) was performed for fabrication of Ohmic contacts. Following predeposition, a short HF etch (HF 10%, 20s) was used to remove the P glass formed, followed by thermal drive-in of the dopants at 1000°C for 1 hour in an N_2 ambient results in high quality ohmic contacts.

---

[1] http://www.bn.saint-gobain.com/

Metal Deposition and Lift-off

Metal deposition was performed using a Lesker thermal evaporator. Evaporation rates of 5Å/second were typical. Lift-off was achieved by soaking the devices in acetone for approximately 30 minutes, followed by a small amount of ultrasonic agitation. The devices were then rinsed in IPA before being dried with N_2.

Rapid Thermal Annealing

Rapid thermal annealing (RTA) was undertaken in a Jipelec Jetfirst Rapid Thermal Annealer[2]. The nominal anneal was 1000°C for 5 seconds. A typical temperature profile, measured by a pyrometer looking at the backside of the support wafer, is shown in figure 3.1.

3.1.2 Nano-scale Fabrication

Nanoscale fabrication was undertaken using electron beam lithography, a standard tool in mesoscopic research. EBL was undertaken on an FEI XL 30 SFEG with a Nabity pattern generation system [3]. This system allows features as small as 12nm to be fabricated, and features as small as 2nm are resolvable when imaging [80]. The details of the various processes used are given below:

Resists and Development

For EBL, a polymethyl-methacrylate (PMMA) resist layer(A3, 950k) was spun (2500RPM, 60s) onto the wafer, resulting in a 160nm resist thickness. After

---

[2] http://www.jipelec.com/products/jetfirst/JIPELEC_jetfirst.pdf

[3] www.jcnabity.com

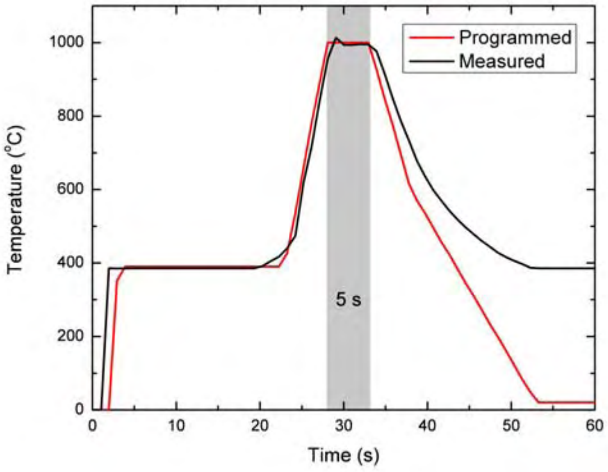

Figure 3.1: Temperature as a function of time for a typical 1000°C, 5 second Rapid Thermal Anneal. The red line shows the set point, while the black line shows the actual temperature measured by a pyrometer looking at the back side of the support wafer.

EBL, this resist was developed in a combination of isopropanol (IPA)/ methyl-isobutyl-ketone (MIBK) (3:1) for 40s, followed by 20s in IPA. This combination of resist and development allows features at least as small as 12nm to be fabricated.

This resist is also able to act as an implantation mask for P ions at 15keV, completely blocking both the ion and forward recoiled resist atoms [81, 82].

Electron Beam Lithography

EBL was undertaken using an FEI XL30 SEM controlled using the Nabity Nanometer Pattern Generation System (NPGS). Beam currents of 50pA and doses of 500μCoulombs/cm^2 were typically used. The working distance was between 5mm and 7mm.

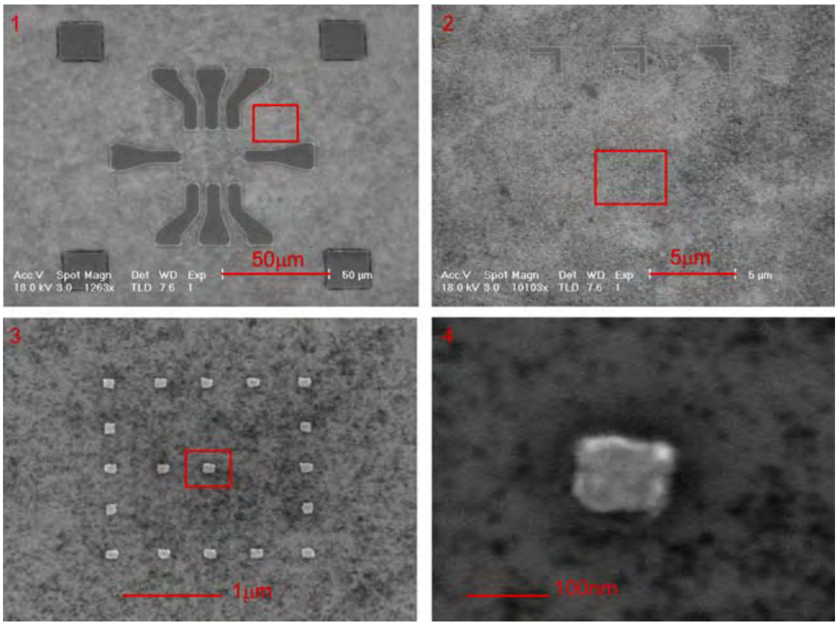

Figure 3.2: Standard EBL alignment marks used in the fabrication of devices for this thesis. The magnification increases from 1 -4. The marks are fabricated from Ti/Au.

Alignment Marks

Alignment marks were fabricated from Ti/Au (∼20nm/40nm) and were capable of alignment accuracy of 50nm [83]. A typical alignment mark, shown in figure 3.2, consists of a 3 × 3 array of nine unique sets of 100nm × 100nm squares, allowing the position of the alignment window to be easily determined over a 10μm × 10μm region with 50nm accuracy.

3.1.3 Ion Implantation

All the ion implantation in this thesis was performed by Dr Jeff McCallum from the University of Melbourne. The implantation was performed at the Australian National University on two different implanters: a 1.7MV NEC Tandem High Energy Ion Implanter and a 175 kV Low Energy Ion Implanter,

Species	Energy (kV)	Range (Å)	Straggle (Å)	Use
^{31}P	15	235	110	Ohmic Leads and Low Density Doping
^{31}P	16	248	115	Low Density Doping
^{75}As	15	161	58	Ohmic Contacts
^{75}As	20	196	69	Ohmic Leads
^{28}Si	15	242	116	Control Implant

Table 3.1: Details of the ion-implantation used in this thesis. Range and Straggle details from SRIM [84].

both with SNICS II ion sources. The choice of implanter depended on availability, as both are capable of implant energies lower than 15kV.

The standard implant species and energies used are given in table 3.1

Non-amorphising Implantation

The highest phosphorus implantation dose-energy combination used in this thesis, 10^{14}P/cm^2 at 15 keV, was chosen such that the implant would have a metallic conductivity at low temperature, but would not cause the Si substrate to become amorphous due to the implantation.

Figure 3.3 shows a TEM, prior to rapid thermal annealing, of a 5nm oxide after P implantation at 15keV at a dose of 10^{14}P/cm^2. The crystal structure of the Si is preserved, indicating that this dose and energy are appropriate parameters to meet the non-amorphising requirement.

Also, measurements of Si:P wires, fabricated by implantation with the same parameters, indicates metallic conductivity with a resistivity $\rho_{sheet} \simeq 900\Omega/\Box$ at 4.2K.[27]

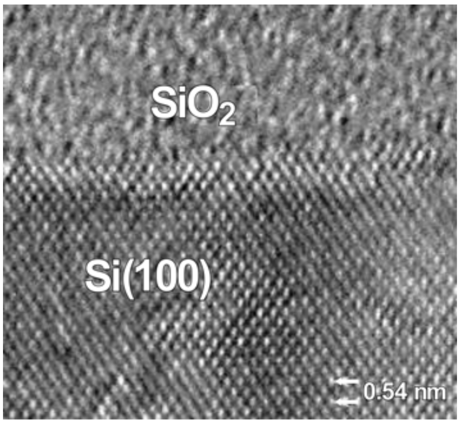

Figure 3.3: TEM of a 5nm oxide interface after P implantation at 15keV at a dose of 10^{14}P/cm^2, and before rapid thermal annealing. The Si crystal structure is not affected by this combination of implant energy and dose.

Arsenic Implantation

During the work presented later in this thesis, it became clear that it would be useful to be able to produce locally doped conducting regions with a dopant other than phosphorus. Arsenic was chosen it is a commonly used donor in silicon.

However, since the implantation of As is not commonly used by this research group, it was necessary to check that the implant was indeed metallic. To this end a Hall Bar, shown in figure 3.4, was fabricated. The device was fabricated in two steps; first the ohmics were implanted at an energy of 15keV and a dose of 10^{14}Ascm^{-2}, followed by implantation of the hall bar at an energy of 20keV at the same dose. The carrier density at 4.2K was found, by a standard Hall effect measurement, to be 6.33×10^{13}cm(-2). This equates to an activation of 63.3% of the arsenic donors. When the implant parameters are considered, the minimum possible value of the maximum doping density is 4.2×10^{19}cm^{-3}, well above the MIT of Si:As (The critical density for the MIT in

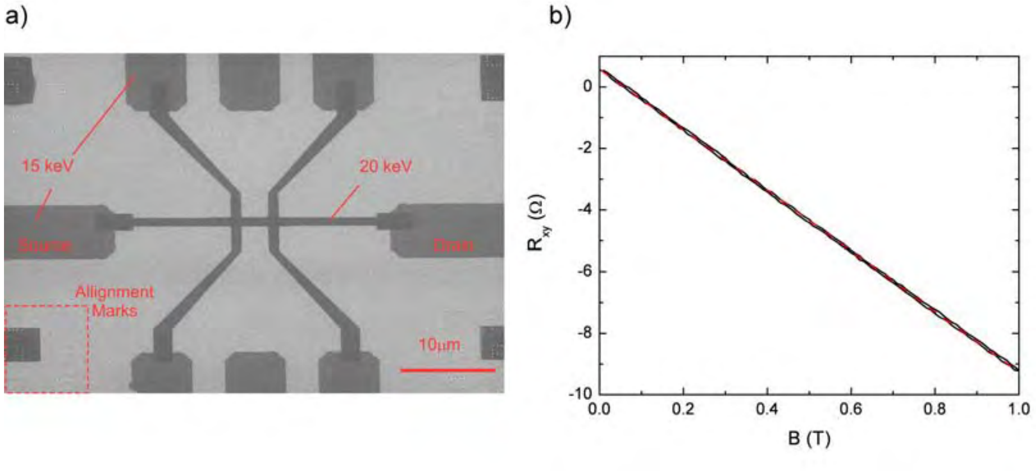

Figure 3.4: a) SEM of the arsenic hall bar used to characterise the arsenic metallic implant. The implant energies are shown for the two different regions. b) the results of Hall measurements on the samples.

Si:As is $8.6 \times 10^{18}\mathrm{cm} - 3$ [85]). The metallic conductivity was also confirmed by the sample conducting in the dark at 4.2K.

This implant density was used for all As implants discussed in later chapters.

3.2 Measurement Equipment and Setup

3.2.1 Low Temperature Measurements

For both conductivity and magnetoresistance measurements at low temperature, a purpose built magnet dip rig was constructed [4]. The stick has a 2T electromagnet surrounding the sample holder. This is placed into a dewer of liquid helium for measurement at 4.2K. A photograph of the setup is shown in

---

[4] The magnet dip rig was constructed by R. Starrett and D. Barber

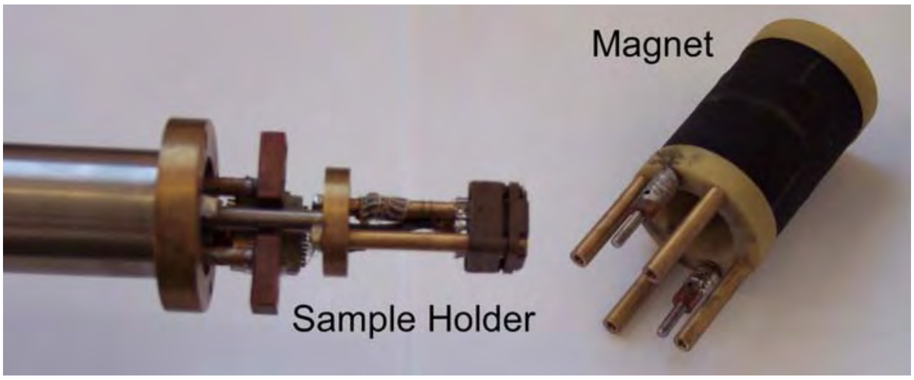

Figure 3.5: Magnet Dip Rig used for 4.2K magnetoresistance measurements. When operated, the magnet is bolted to the end of the stick, with the sample at centre field.

figure 3.5.

Measurements in Appendix A were undertaken in dilution refrigerator, allowing access to temperatures as low as 30mK. Measurements of EDMR were undertaken using a helium flow cryostat, and is discussed in section 3.3 below.

3.2.2 Electrical Measurments

Lockin Amplifiers

For measurements requiring lock-in amplification, a Stanford Research Systems SR830 was used. The modulation frequency was chosen to be 13.8Hz for the measurements on MOSFETs, and driving voltages in the range 100 μV to 500 μV were used as appropriate.

Source-Measure Unit

For the application of DC voltages, a Keithley 236 Source Measure Unit was used, providing a voltage with an accuracy of ±0.033%.

3.3 EDMR Measurement

The experimental setup, which is shown in figure 3.6, can be broken into three discrete systems: ESR Manipulation, Temperature Control, and Electrical Measurement.

ESR Manipulation

Measurement of EDMR spectra was accomplished by placing the samples in a dielectric ring microwave resonator, with a HP83640A microwave source. An external magnetic field is applied using a stable electromagnet, and a small amplitude magnetic field modulation, controlled by a Stanford Research Systems SR830 lock-in amplifier, was applied. The resonant cavity has a window allowing illumination of the sample with white light from a tungsten lamp.

Temperature Control

The cavity is placed inside an Oxford Instruments Continuous Flow Cryostat, with the temperature controlled by an Oxford ITC 501 temperature controller. The temperature can be varied from less than 5K to over 35K, and is stable to less than 0.1K.

Electrical Measurement

Another important part of the electrical measurement is the ability to make electrical connection to the sample. Figure 3.7 shows the sample glued to the end of a quartz tube. This tube is small enough to fit into the resonant cavity. It is also hollow, allowing wires to be passed down to the sample for electrical connection.

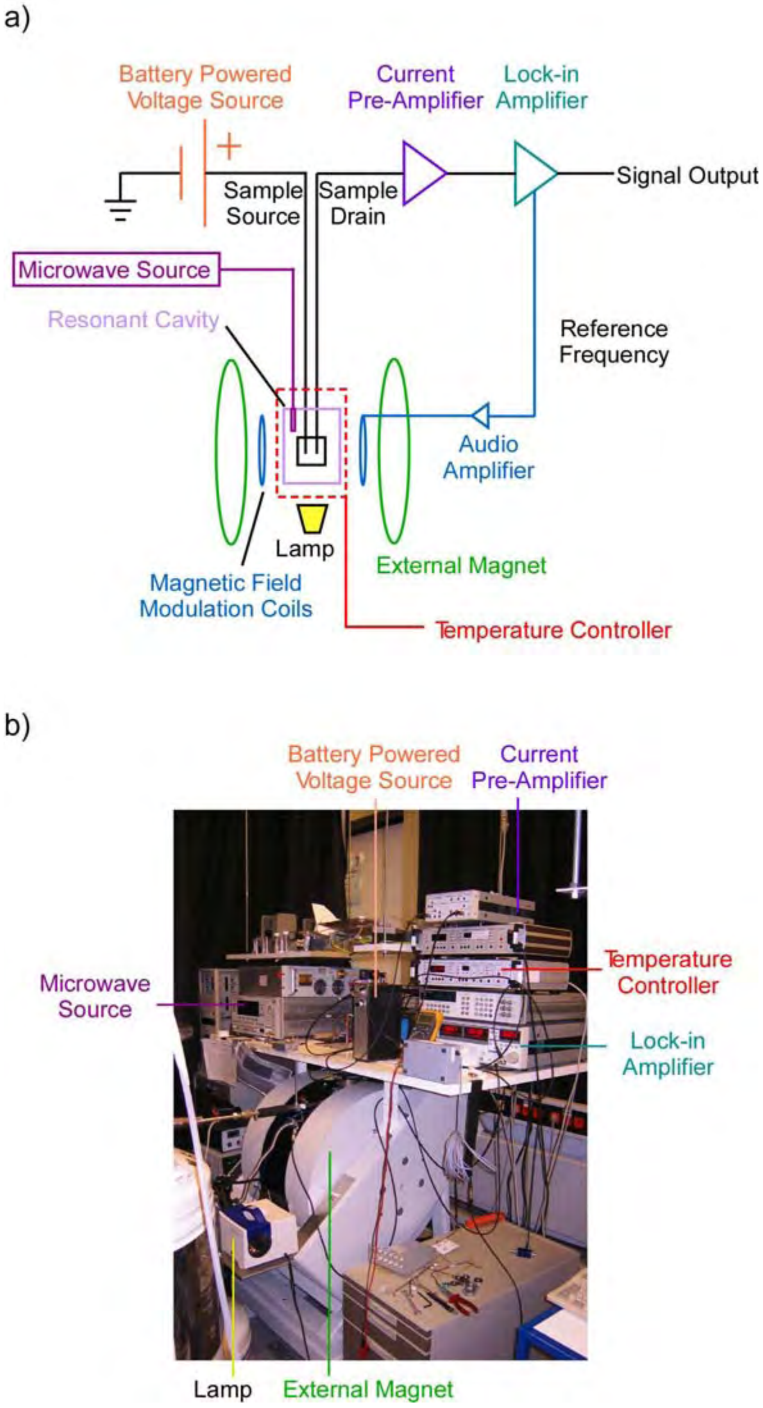

Figure 3.6: a) Schematic and b) photograph of the setup used for the EDMR measurements reported in this thesis. The equipment is located at the Walter Schottky Institute, Technical University of Munich, Germany.

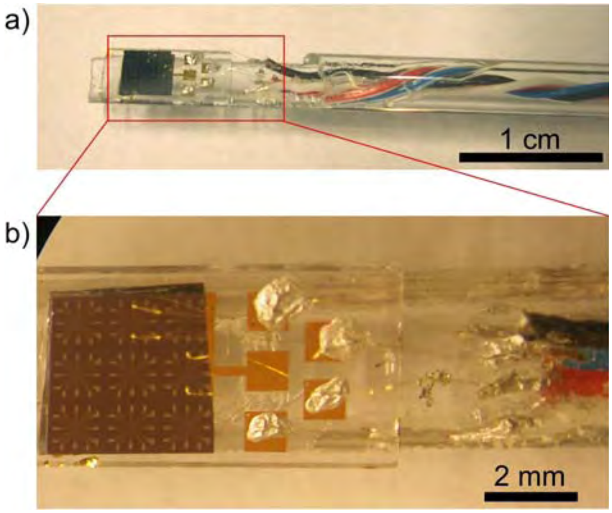

Figure 3.7: a) Photograph of a sample attached to the quartz tube. The sample sits on a glass slide with gold pads for bonding. Wires running through the tube are also fixed to the gold pads with conductive epoxy. The magnified view (b) shows how electrical contact is made to the device through a combination of bonding and gluing of this gold wires. The sample in this case consists of a 3×3 array of devices, of which 2 are independently contacted.

DC voltages are applied to the sample using a battery, as they provide a very low noise voltage source. The measurement electronics, shown schematically in figure 3.6, are relatively simple. The output of the sample is connected to a current preamplifier, which outputs a voltage proportional to the input current. This voltage is fed into the SR830 lock in amplifier that is used to control the small oscillating magnetic field, with lockin detection at the reference frequency. The output of the lockin amplifier is scaled to give dI/dB, the change in the device current caused by the oscillating magnetic field. A linear background is subtracted to obtain the change due to the resonant phenomena.

Chapter 4

The Effect of Ion Implantation on Device Performance

In this chapter, the quality of the thermal oxide is determined using low temperature I-V measurements of Si-SiO$_2$ MOSFETs. The effect of ion implantation on the quality is determined, and the implications for Si QIP hardware fabricated with this technique are discussed.

Parts of this chapter have been published as:

Donor activation and damage in Si-SiO$_2$ from low-dose, low-energy ion implantation studied via electrical transport in MOSFETs
D. R. McCamey, M. Francis, J. C. McCallum, A. R. Hamilton, A. D. Greentree and R. G. Clark
Semiconductor Science and Technology **20**, 363-368 (2005).

4.1 Introduction

Before beginning studies of devices fabricated on phosphorus doped silicon, it is important that the material system and key fabrication processes are well characterised. As future work will strongly depend on the ability to fabricate devices via ion implantation, it is important that the effect of implantation be well understood. This chapter presents results on the effect of ion implantation on device performance.

Device fabrication involving ion implantation is widespread in the semiconductor industry, with applications ranging from ohmic contacts to shallow junctions [78, 86]. Methods to increase the performance of classical transformers [87], new types of classical computation [88], and a number of solid state implementations of quantum computation (QC) [15, 19, 26, 89–91], all involving ion-implantation of few or single ions, have been proposed. Some of these were discussed in detail in chapter 2.

In all of these devices, electrically active defects caused by ion implantation must be eliminated so that operations involving single electrons are not compromised. To ensure that this requirement is met, it is important to characterize the effects of ion implantation on the trap density. It is also important that all implanted donors be activated for the device to function correctly. Given that these devices are intended to be operated in the few or single electron regime, a non-activate donor anywhere in the device would strongly inhibit device function.

Previous studies of damage caused by ion implantation have mainly involved capacitive measurements (eg capacitance-voltage, Deep Level Transient Spectroscopy [92]) or have focused on room temperature measurements

[93]. The following section focuses on the characterization of implantation-induced defects in MOSFET devices using DC transport measurements at low-temperature, where silicon-based quantum computer devices are most likely to be operated. The donor activation in these devices is also studied.

4.2 Method

4.2.1 MOSFETs

Metal-Oxide-Semiconductor Field-Effect-Transistors (MOSFETs) are convenient to fabricate, have widely understood characteristics, and allow electrical measurements to be restricted to near the Si-SiO_2 interface [94], the area of interest for low-energy implantation studies. The processing is also identical to the processing used for devices presented in later chapters. Additionally, the processing used in the fabrication of MOSFETs is expected to be compatible with the fabrication processes used, for example, in silicon-based quantum computer devices. This allows the possibility of fabricating on-chip characterization devices. For these reasons, MOSFETs were used to characterize the implant damage.

Device Fabrication

The devices used in this study, Hall-bar geometry MOSFETs, were fabricated on a high resistivity ($> 5000\Omega$.cm) n-type Si <100> substrate. After etching in a 10% HF solution for 10 seconds to remove the native oxide, a 5nm thermal oxide layer was grown. Two implant species, P and Si, were used; P as this is the most common donor in silicon and has important applications in QC pro-

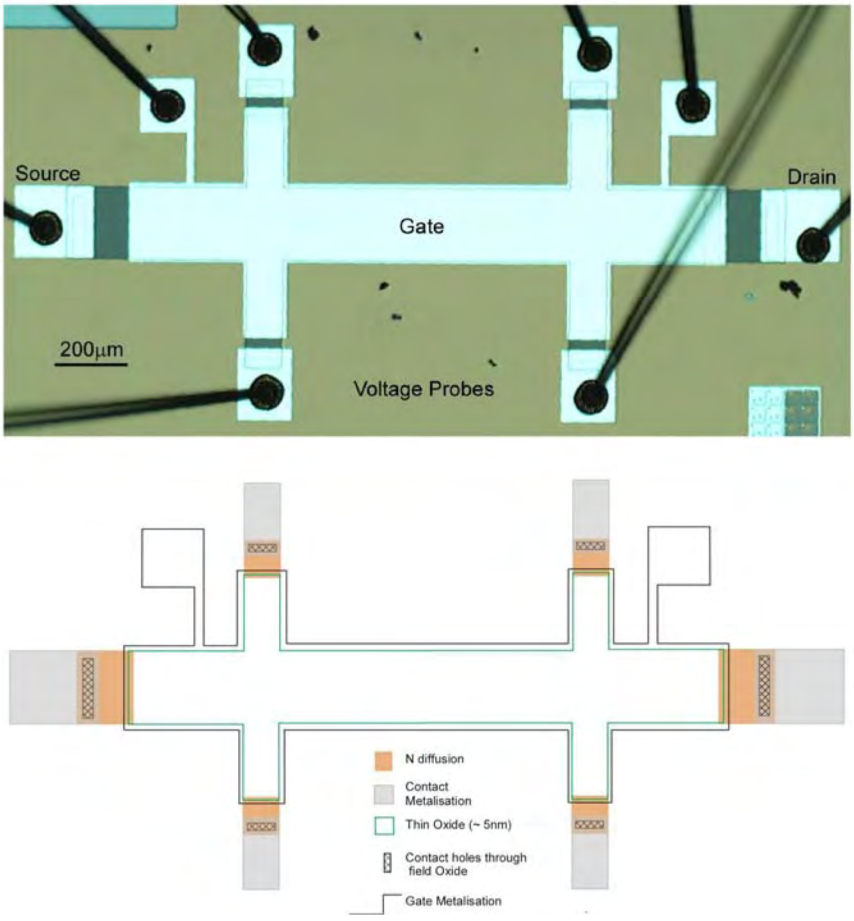

Figure 4.1: Image (top) and layout (bottom) of a silicon Hall-bar MOSFET identical to those used for the measurements presented in this chapter.

posals, and the Si as a control. A number of devices were then implanted with either P at 16keV or Si at 15keV. This results in an implant distribution centered approximately 20nm into the silicon, with a straggle of approximately 7nm [78]. A number of different doses were implanted, ranging from no implant to $5 \times 10^{12}\text{cm}^{-2}$. Rapid thermal annealing at 1000^{O}C for 5 seconds in a N_2 ambient was then applied to all devices. For both the gate and ohmic metallization 200nm of Aluminium was used. Following metalisation, the devices were annealed at 400°C for 15 minutes in forming gas (5% Hydrogen, 95% Nitrogen).

4.2.2 Mobility and Critical Density at 4.2K

Numerous methods exist for characterizing the electrically active defects in Si-SiO_2 at room temperature [95]. At cryogenic temperatures, where standard capacitance based methods fail due to the long thermal emission time, a number of more complex methods also exist [96]. Some simpler methods using the Hall effect involve comparing measured values of carrier density with theoretical predictions [97, 98]. This work use a method that involves only conductance and Hall measurements, removing errors associated with comparison to theory and allowing for ease of measurement.

At low temperatures, the mobility, μ, of an electron in the inversion layer of a MOSFET as a function of the carrier density, n, is characterized by a critical density, n_{crit}, below which no conduction occurs. The lack of conductivity below the critical density is due to a freeze out of free carriers due to impurity binding [99]. The method used to characterize the trap density in this work is based on the above property. The mobility as a function of the carrier density was determined from Hall measurements. The critical density was then determined by extrapolating the linear region of μ vs $\log(n)$ above the critical density to zero. The trap density of the device is taken to be the critical density.

Measurements at 4.2K were performed to determine the number of electrically active traps present at low temperature. The 4-terminal resistivity, ρ, of the inversion layer was measured at numerous gate voltages (see figure 4.2A,B for characteristic measurements). Hall measurements (Figure 4.2C) were taken from B=0 to 0.5T, for at least 5 gate voltages per sample. The carrier density as a function of gate voltage was determined from these measurements (Figure 4.2D). The mobility was determined using both the resistivity and the carrier density by the relation [78]

$$\mu = 1/(\rho n e). \tag{4.1}$$

4.2.3 Threshold Voltage Shift at Room Temperature

To determine the fraction of implanted ions that were activated, the threshold voltage shift was analyzed. Assuming the ions are implanted to a constant depth (ie a delta function approximation), the relation between doping and threshold shift is given by [78]

$$n_{\mathrm{act}} = \frac{\Delta V_{\mathrm{th}} C_{\mathrm{imp}}}{q} \tag{4.2}$$

where n_{act} is the number of activated donors per unit area, ΔV_{th} is the change in threshold voltage, and C_{imp} the capacitance per unit area between the implanted ion layer and the gate. As the implant distribution sits 20nm into the silicon, the capacitance is the sum of that due to the oxide and the silicon layer, ie

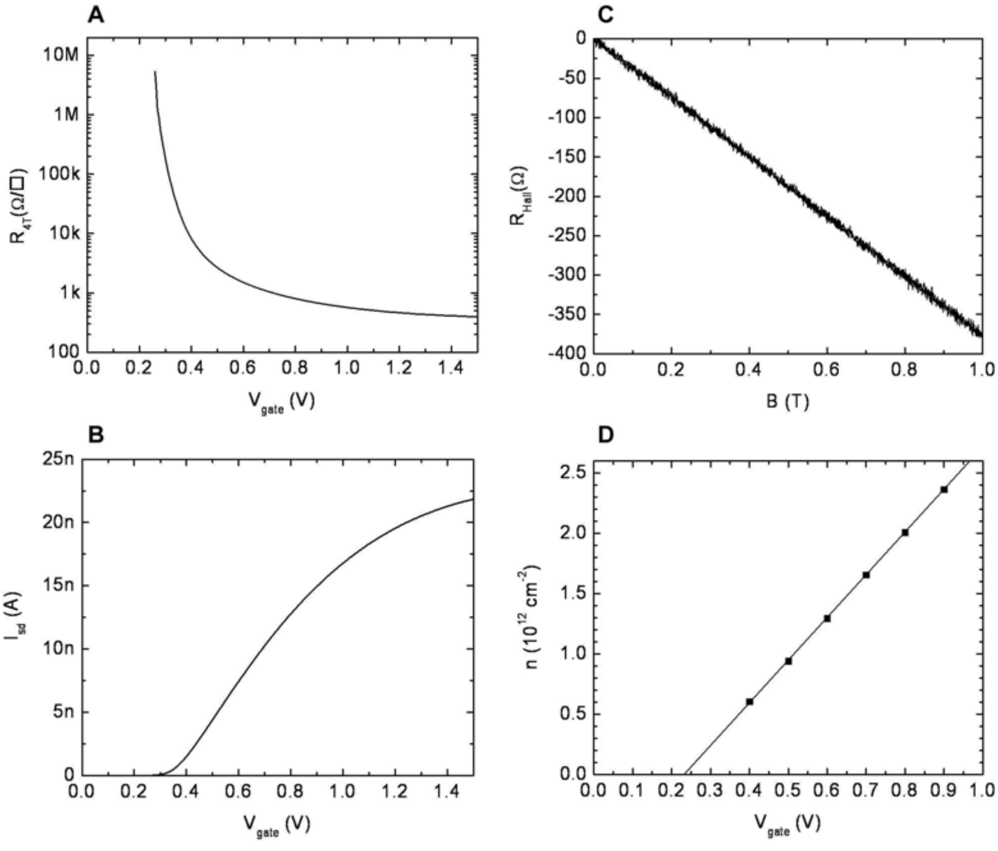

Figure 4.2: Characteristic example of measurements used to determine the effect of ion implantation on device performance. Examples show A) 4-terminal resistance, B) Source drain current, C) Hall resistance at a fixed gate voltage and D) using the carrier densities determined at a set of gate volatges to determine the carrier density for all gate voltages.

$$C_{\text{imp}} = [(1/C_{\text{ox}}) + (1/C_{\text{Si}})]^{-1} = [(d_{\text{ox}}/\epsilon_{\text{ox}}\epsilon_0) + (d_{\text{Si}}/\epsilon_{\text{Si}}\epsilon_0)]^{-1} \tag{4.3}$$

where d_{ox} is 5nm, ϵ_{ox} is 3.7, d_{Si} is 20nm and ϵ_{Si} is 11.9.

It is important to note that this method is only valid for ionised impurities, and for this reason the measurements were performed at room temperature. The effect of incomplete ionisation [100] is discussed in section 4.3.

To confirm the validity of the delta approximation, once the number of ionised impurities was determined, the expected threshold shift was calculated using a model for the implants that consisted of a series of very thin, uniform implant regions that very closely followed the actual implant distribution. The threshold shift due to each of these was determined and the total shift found. There was a negligible ($< 1\%$) difference between these methods, indicating that the original single delta approximation was sufficient.

Modelling, using a one-dimensional Poisson solver [101], of both implanted and unimplanted devices was also performed. The carrier density as a function of depth for a number of gate voltages was determined, and integrated to find the carrier density as a function of gate voltage. The threshold in these simulations was compared to the experimentally measured threshold, again confirming the density of activated ions.

4.3 Implant Activation at Room Temperature

The I-V characteristics of the MOSFETs were measured at room temperature. The results for different P implant densities are shown in figure 4.3. The threshold voltage was taken to be the intersection of the linear fit to the sub-threshold

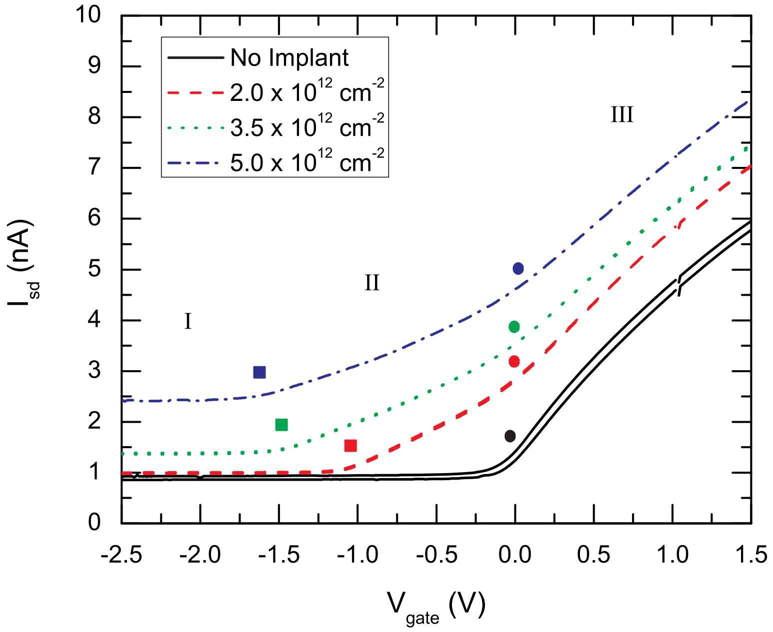

Figure 4.3: Source drain current as a function of Gate voltage, showing threshold voltage shift as a function of implant density. Measurements taken with a 100μV source drain voltage at room temperature. The squares indicate the threshold voltage after implantation. The circles show the location of the kink in the current at a similar voltage to the threshold in the unimplanted device.I, II, and III indicate three different conduction regimes, which are discussed in the text.

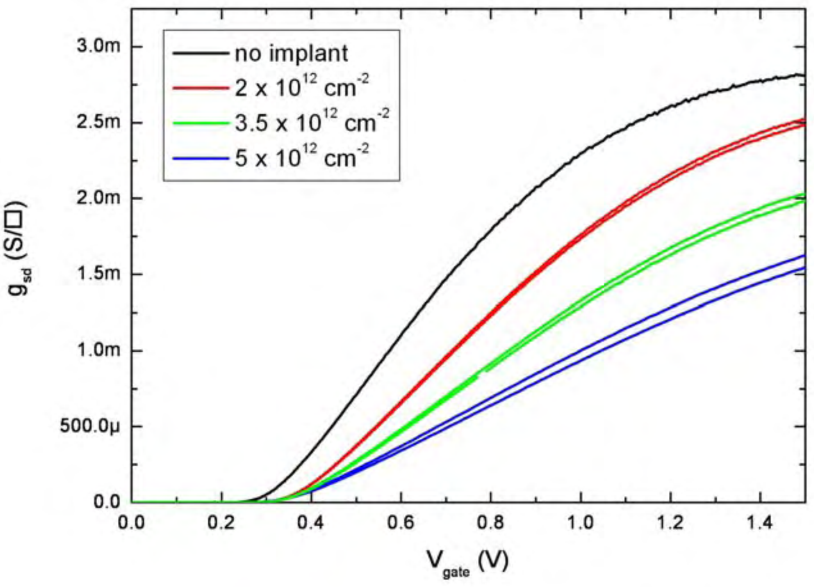

Figure 4.4: Source drain conductivity as a function of Gate voltage, showing no threshold voltage shift as a function of implant density. Measurements taken with a 100μV source drain bias at 4.2K.

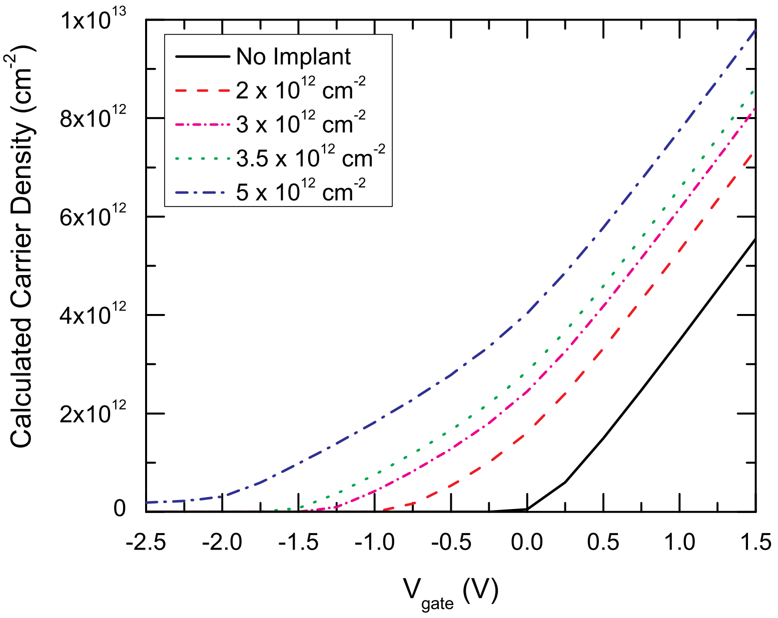

Figure 4.5: Calculated carrier density vs gate voltage, T=300K, implant range = 20nm, implant straggle = 7nm.

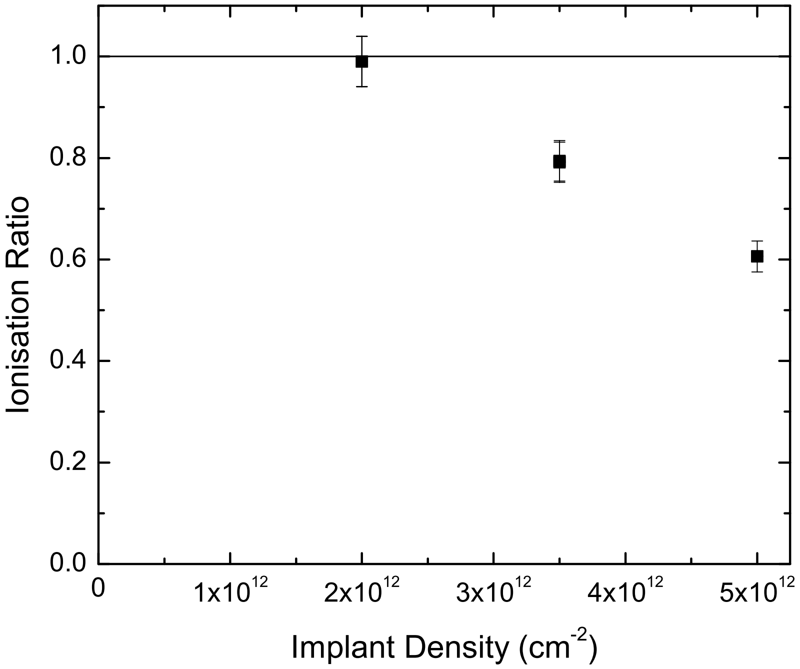

Figure 4.6: Measured ionisation ratio (number of activated ions times probability of ionisation divided by number of implanted ions) as a function of implant density for P implants at 16keV after rapid thermal annealing.

current and the linear fit to the current in the region just above the point where the current deviates from the sub-threshold current. As expected, the threshold voltage is decreased by the addition of n-type dopants. The Si implanted control devices did not show a decrease in threshold voltage, which shows that the change in threshold is due to the incorporation of donors, and not the creation of charged damage during implantation.

The activation ratio is defined as the number of activated P atoms (ie those sitting in substitutional sites) divided by the number of implanted P ions. The threshold voltage shift is determined by the number of charged P donors, which is the product of the number of activated donors and the probability that they are ionised. Figure 4.6 shows the measured ionisation ratio (activation ratio times probability of activation) as a function of the implant dose. The ionisation ratio is found to decrease with increasing implant dose. This is expected, given that the fraction of ionised donors is known to decrease with increasing density of donors [102], due to the increased number of dopant states available, even at room temperature [100]. The ionisation fraction is given in reference [102] as:

$$\frac{n_d}{n + n_d} = \frac{1}{\frac{N_c}{2N_d}\exp\left[-\frac{(E_c - E_d)}{k_B T}\right] + 1} \tag{4.4}$$

Recent studies of P-implanted silicon by spreading resistance analysis (SRA) have shown the opposite trend - that the apparent activation ratio increases with increasing implant dose [90, 103]. This discrepancy might possibly be explained by the presence of a native (poor quality) oxide with a high trap density in very close proximity to the implanted region, caused by cutting the wafer at a very shallow angle. If a significant density of electrons are caught in traps at the native oxide interface they do not contribute to conduction, so that the number of free electrons appears lower than that expected due to the implant dose. This effect would be particularly significant at low implant dose, where the native oxide trap density is much higher than the P density, but would be less important at high doses, leading to an apparent activation ratio that increases with increasing implant dose, as observed by Schenkel *et al* [90, 103]. If this is the case, it means that spreading resistance measurements are not well suited to measurements of low dose, near surface implants. This conclusion has also been reached recently by the authors of the studies mentioned [104], however they cite the ionisation of electrons due to band bending near an ungated interface as the cause.

It is significant however that after RTA and for an implant dose of $2 \times 10^{12}\text{cm}^{-2}$ with an average spacing of $\sim$ 7nm, the ionisation ratio is 0.99 ± 0.05, indicating almost complete activation and ionisation. Assuming that this near complete activation holds for doses below $2 \times 10^{12}\text{cm}^{-2}$, this result suggests that it will be possible to fabricate a device where the donor spacing is $\sim$ 20nm, such as the qubit proposed by Kane [19], with almost complete donor activation.

Another interesting feature to note is the appearance of three distinct conduction regimes in the implanted devices, labeled I, II and III in figure 4.3. In region II, from threshold to the threshold associated with the unimplanted device, the device current increases near linearly. Above the unimplanted threshold, when the device enters inversion, the device current returns to the expected form but with an offset (region III). In region I, below threshold, there is a constant current unaffected by the gate voltage, but which increases with implant density. The source of this current is unknown. A possible explanation is that the silicon dioxide used as an implant mask was not thick enough, resulting in an implant in the area outside of the gated area. However, the thickness of the implant mask ($\sim$ 200nm) should be more than adequate to stop all of the implanted ions, which have a range of $\sim$ 15nm in SiO_2 at 15keV [78]. Alternatively, Poisson modelling shows that there is a small increase in the carrier density deep in the silicon ($\sim$ 50nm)for implanted devices at negative gate voltages (see figure 4.7). This would explain the increased conduction, except that the carrier density at negative voltages is 5 orders of magnitude smaller than that at positive voltages, which does not explain the high current observed. More work is needed to understand the cause of this conduction.

Modelling of the devices using a one-dimensional Poisson solver [101] was undertaken, and the carrier density as a function of depth for a number of gate voltages are presented in figure 4.7. In the implanted devices, an increase in the carrier density, centered at the mean implant depth, d_{Si}, is observed. The density in this region increases with gate voltage, until the unimplanted threshold is reached. For higher gate voltages, the carrier density is dominated by the inversion layer adjacent to the Si-SiO_2 interface.

The total carrier density at a given gate voltage and implant density was determined by integrating the calculated carrier density to a depth of 100nm. The results are shown in figure 4.5. These traces have a similar form to the measured current (figure 4.3) showing the two distinct conduction regimes above threshold, but not the sub-threshold current. The effect of scattering can be seen in the deviation of the measured current from the calculated carrier density. The threshold however should not be effected by the scattering mechanisms, and the current should go to zero at the same gate voltage as the carrier density.

Calculations were performed for devices with P implants of 2, 2.7 and

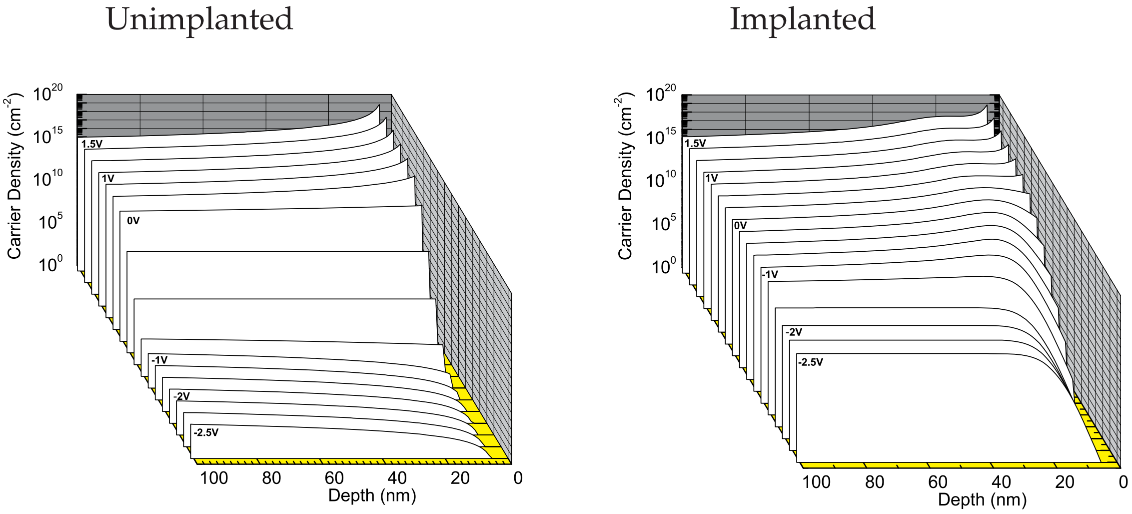

Figure 4.7: Calculated carrier density as a function of depth and Gate Voltage, at room temperature for an unimplanted MOSFET (left) and for a MOSFET with a P implant dose of 3.5×10^{12} cm^{-2} (right). T = 300K.

$3{\times}10^{12}$ cm^{-2}, the density of activated donors determined from the threshold voltage shift. The threshold found in these calculations was in good agreement with that observed experimentally, and better than those simulations where the incomplete ionisation of donors was not considered. This indicates that the analysis of the activation ratio is correct.

In summary, there is a decrease in the threshold voltage due to the implantation of donors, although the magnitude of the decrease is smaller than expected. This may be due to the incomplete ionisation of the implanted donors, which serves to limit their effect on the threshold voltage. For an implant of $2{\times}10^{12}$ cm^{-2}, the activation is near 100%.

4.4 Damage due to Implantation

This section considers the damage caused by the implantation process. Figure 4.8 shows the mobility of P implanted MOSFETs, at a number of different doses. The traces show the usual form of the low temperature mobility, that is, at low density, an increasing mobility limited by impurity scattering, and at high density, a decreasing mobility limited by scattering due to interface roughness. Traces for a number of different implant densities are shown.

In the P implanted devices, the maximum mobility is seen to decrease and move to higher carrier densities (figure 4.9) as the implant dose is increased, indicating an increase in ionized impurity scattering. For Si implanted devices the mobility, shown in figure 4.8, does not show this effect. As the Si and P ions are of similar mass, and are implanted at similar energies, they should cause similar damage to the Si lattice during implantation. As the decrease in mobility is not seen in the Si implanted devices, the cause of the increased scattering does not appear to be the implantation process. This result suggests that the RTA is able to repair all damage from implantation. An alternate explanation is that stable P-related defects may form during the annealing process accounting for the increased trap density, but we believe that this will be a secondary effect when compared to the lattice damage caused during implantation.

It is important to note that there are variations in the mobilities across wafers and from chip to chip, however, the deviation between devices on a similar chip is much smaller than that from chip to chip from the same wafer, which is smaller again than that from wafer to wafer. To combat this, the measurements for a given implant species were taken from single wafers. The wafers were cleaved into quarters, with three quarter pieces implanted at a different dose, and one quarter being left unimplanted. As a result, it is difficult to compare numerically the results from wafer to wafer. This explains the higher peak mobility in the Si implanted devices compared to the P implanted devices.

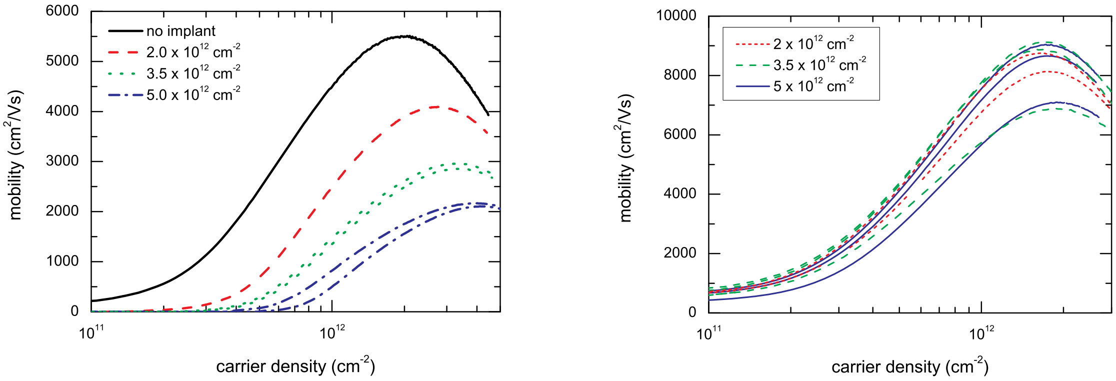

Figure 4.8: Mobility as a function of carrier density for MOSFET's with various P (left) and Si (right) implantation densities.

The critical density of both P and Si implanted devices is shown in figure 4.10. For P implanted devices, the critical density increases linearly with implant density. Equating the critical density with the trap density [99] shows that each implanted ion has an equivalent effect to the creation of 0.08 ± 0.03 additional traps. For Si implanted devices, this effect decreases to 0.009 ± 0.005 additional traps.

The above results can be explained by the straggle of the implanted ions. Modelling of the implanted ion distribution using data from [78] shows that, for the implant energy used, approximately 10% of implanted ions sit within 10nm of the interface. Modelling of the wavefunction using [101] and other

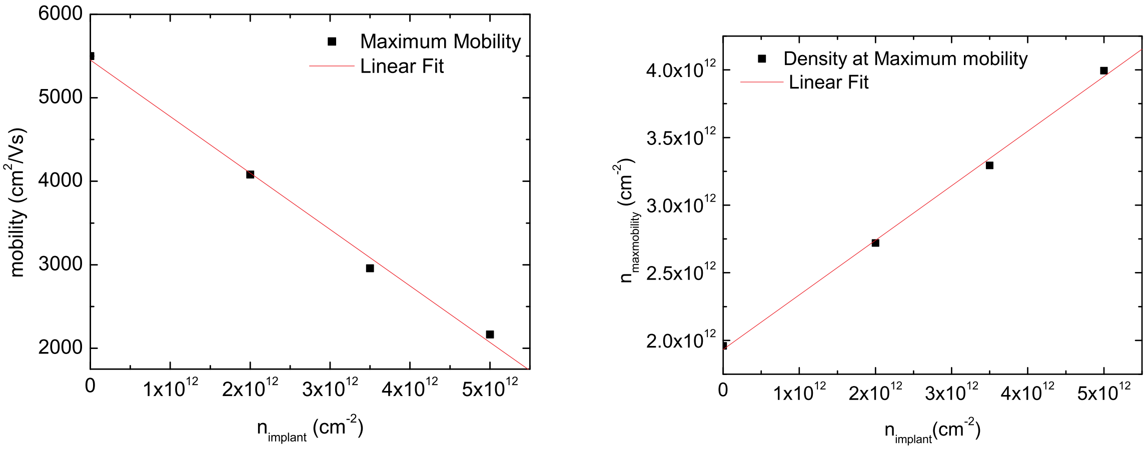

Figure 4.9: Maximum mobility (left) and carrier density at which maximum mobility occurs (right) as a function of P implant density. Both the decrease in mobility and the movement of peak mobility to higher density indicate an increase in charged impurity scattering as the implant dose is increased.

studies [105] shows that electrons in the inversion layer are localized to within approximately 10nm of the Si-SiO$_2$ interface. Hence, only about 10% of the implanted ions will interact strongly with the electrons in the inversion layer.

Below threshold, there are no electrons in the 2DEG, and all donor electrons are bound to the P implants. Above threshold, when the channel is populated with electrons, the additional electrons serve to screen the P donors, and they are unable to localize any electron [105]. At this point, the ionized P donor scatter the electrons in the 2DEG, leading to the increased ionized impurity scattering seen in figure 4.8. This also explains the movement of the critical density, as the electrons that are localized below the threshold are free to contribute to the Hall voltage, and thus the carrier density, above threshold.

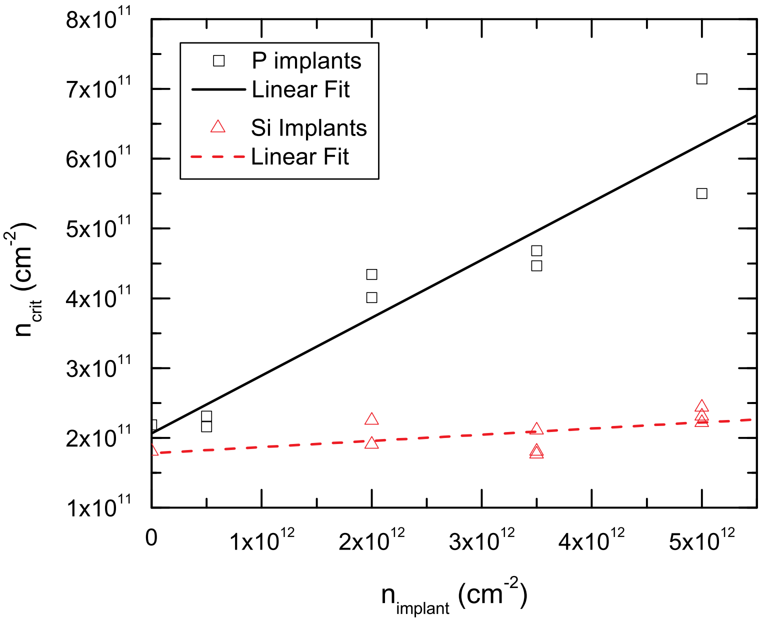

Figure 4.10: Trap density vs Implant density for both P and Si implanted devices. Linear fits to the data are shown. The data for P implants at $5 \times 10^{11}\text{cm}^{-2}$ is for a device fabricated on a separate wafer.

The increase in the critical density (8% of implant) is in good agreement with the number of implanted donors near the 2DEG ($\sim$ 10% of implant), again suggesting that RTA is able to remove all damage caused by implantation, and that the increased scattering and trapping is due only to the P donors close to the Si-SiO$_2$ interface.

Another important characteristic is the density of electron traps in the unimplanted device. This was found to be $2.1(\pm 0.3) \times 10^{11}\text{cm}^{-2}$. This equates to a trap spacing of 21.8 ± 1.7 nm. For a Kane architecture quantum computer, this is approximately the qubit-qubit spacing (20nm). This means that for every implanted P donor there is approximately one electron trap, which will interfere with device operation, either by localizing the donor electron or by other methods. While this density of traps may be suitable for fabrication of a small number of silicon-based qubits, it will need to be reduced, for example by improving the oxide quality, for the large scale (many qubit) implementations that are proposed.

4.5 Shift in threshold of low dimension MOSFETs

During experiments on thin, long MOSFETs at 4.2K that are not described in this thesis, an interesting feature was seen in the I-V characteristics of the devices. If the device was cooled from room temperature to 4.2K with the gate grounded, the IV characteristic of the device was seen to shift to a slightly higher gate voltage on the second and subsequent sweeps of the gate, compared with the first sweep.

Figure 4.11 shows the results for a device with a 100nm wide gate and an oxide thickness $t_{\text{OX}} = 5$nm.

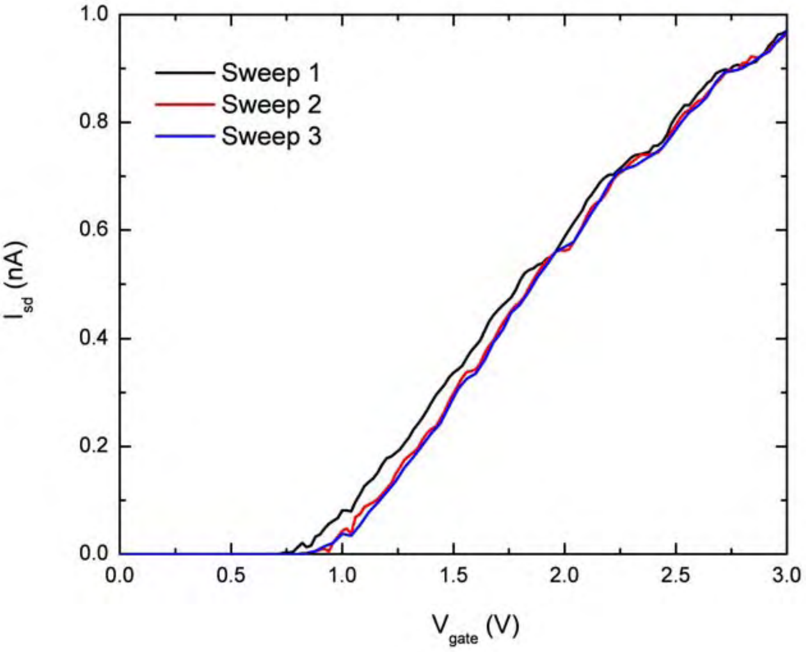

Figure 4.11: Shift in threshold voltage between first and subsequent sweeps of the gate voltage in a thin gate MOSFET.

As can be seen, the threshold moves upwards by 0.05V. A simple model for this behaviour is that the traps at the interface, which act as an additional positive charge, are filled with donors when the 2DEG is formed, as at this point conduction electrons are able to reach the location of the trap. Due to the extremely long trapping time at 4.2K, these electrons then become permanently bound to the trap. As the gate is turned off, the electrons stay on the traps. Thus, a slightly larger gate voltage is required on the next sweep to compensate for the decrease of positive charge on the traps. Also, note that the curves for the first and subsequent trace converge at high gate voltage. This is expected, as the number of traps not filled at higher voltage would be greatly reduced.

Assuming this model, then the voltage shift should relate to the defect density by

$$n_{\text{trap}} = \Delta V_{\text{th}} \text{Cox}/e \tag{4.5}$$

We find that the change equates to a defect density of $2 \times 10^{11}\text{cm}^{-2}$, which is in good agreement with the values determined in section 4.4 above.

This shift was seen in a large number ($\sim$ 10) devices, and in all of these gives a value for the trap density in the range $1 - 4 \times 10^{11}$ defects cm^{-2}.

4.6 Conclusion

In this section, the density of electrically active traps at low temperature was characterized, using DC conductance measurements in silicon MOSFETs. By studying the effect of low-energy low-density Si and P ion implantation into a Si-SiO_2 system, it was found that the Si implantation had no effect on the low temperature trap density, whilst the P implantation resulted in an additional

$0.08(\pm0.01)$ traps per implanted ion. We interpret these additional traps to be P donors in the conduction channel acting to localize donor electrons, and not damage due to implantation.

The 'as grown' defect density is $2.1(\pm0.3) \times 10^{11}\text{cm}^{-2}$, determined from MOSFET conductivity measurements and supported by low temperature shifts in thin MOSFET threshold voltages.

We also find that the electrical activation of the implanted donors to be near complete at a dose of $2 \times 10^{12}\text{cm}^{-2}$, falling to approximately 60% at a dose of $5 \times 10^{12}\text{cm}^{-2}$. This indicates that a device that requires a donor spacing of approximately 20nm, such as the Kane quantum computer, can be fabricated with near 100% activation using ion implantation.

Chapter 5

Effect of Dielectric Choice on Device Performance

In this chapter, the efect of various barrier dielectric on the electrical properties of Si-MOSFETs is studied. This has implications for the fabrication of devices reported later in this thesis, where the highest quality oxides are required, as well as informing the fabrication processes used in devices where limited thermal diffusion of donors is critical.

One of the most important features of a MOS structure is the dielectric oxide layer, and its interface with the semiconductor. The correct choice of dielectric can change the transport properties of a device by orders of magnitude. Dielectrics are also important in solid state QC as they are a major source of decoherence. For example, the dielectric loss of a spacer dielectric in Josephson qubits is found to strongly effect the coherence times that the system exhibits [106].

In this chapter, measurements of the transport properties of MOSFETs with three different dielectric materials are presented. The method used is the same as in the previous chapter (see section 4.2.2). Briefly, the mobility-carrier den-

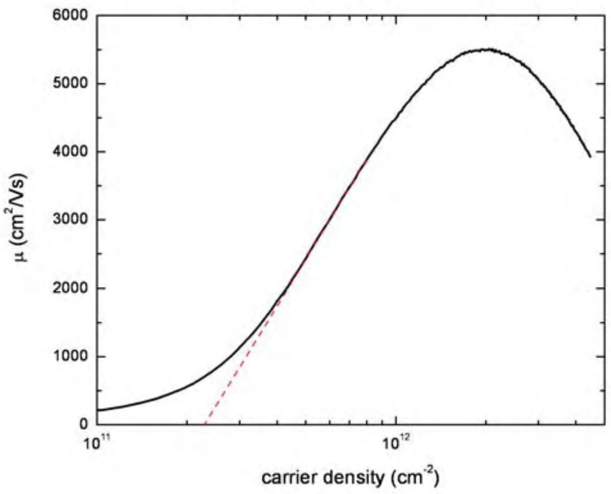

Figure 5.1: Mobility vs carrier density of a Si-Thermal SiO_2 MOSFET at 4.2K. $T_{ox} =$ 5nm.

sity relationship of the MOSFET is determined at 4.2K. The critical density where the mobility goes to zero is taken to be the trap density.

5.1 SiO_2 - A high temperature Thermal Oxide

Thermal growth of SiO_2 is a widely used method of obtaining a high quality oxide on silicon, as the processing is relatively simple and highly controllable.

MOSEFTs were fabricated on Si wafers with thin (5nm) thermal oxides. The details of the oxide growth were given in section 3.1.1. The results of measurements on these devices were discussed in detail in the last chapter. A characteristic mobility-carrier density plot is shown in figure 5.1.

The trap density was found to be $2.1(\pm 0.3) \times 10^{11}\text{cm}^{-2}$ for as grown thermal oxides. The maximum mobility was 5501 cm^2/Vs, at $n = 1.96 \times 10^{11}\text{cm}^{-2}$. This compares well to other reported values of the mobility in MOSFETs with thermal SiO_2 as the dielectric. However, there have been reports of mobilities of up to $\sim$ 70000 cm^2/Vs in MOSFETs with $n_{crit} = 0.7 \times 10^{11} cm^{-2}$ in some cases[107], indicating that there is room for improvement in the oxide growth.

5.2 Low temperature deposition of Oxides

An important consideration when an oxide is deposited is the diffusion of dopants in a device. As the size of electrical devices are decreased, control of the placement of dopants becomes more important. For phosphorus doped silicon, a thermal treatment at 950°C for 10 minutes will give a diffusion length of 15nm. Recent advances in the placement of single dopants in silicon with atomic precision by STM lithography require that any future processing be at low temperature to limit diffusion of the dopant atom [108]. One way to achieve this is to deposit oxides at low temperature. The following section will focus on dielectric barriers formed by low temperature deposition.

5.2.1 Plasma Enhanced Chemical Vapor Deposition (PECVD) of SiO_2

Chemical vapor deposition is a widely used technique for depositing dielectrics. The sample to be deposited is placed into a vacuum chamber, which is filled with a combination of precursor gases. For silicon dioxide, the precursors widely used are silane, SiH_4, and oxygen. The reaction of these two gases forms the SiO_2 layer, with hydrogen produced as a byproduct. Plasma enhancement provides energy additional to the thermal energy, which helps in the growth of oxides at low temperature [22].

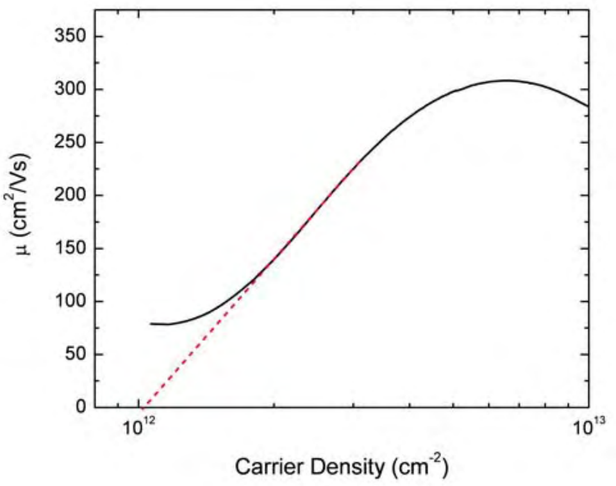

Figure 5.2: Mobility vs carrier density of a Si-PECVD SiO_2 MOSFET at 4.2K. T_{OX} = 39nm.

SiO_2 deposited via PECVD is widely used as a dielectric barrier, with uses ranging from ion implantation masking to passivation layers [22]. It is useful in that it can be deposited at very low temperatures (∼ 400°C), which serves to limit diffusion of donor species within the sample. However, the quality of PECVD SiO_2 is generally considered to be worse than thermally grown SiO_2 [22].

Using the same Hall bar structure as in section 5.1, PECVD SiO_2 of nominally 40nm thickness was deposited at 400°C. From the linear n vs V_g relationship, the thickness of the oxide is found to be 39nm. The mobility as a function of carrier density was determined at 4.2K, and is shown in figure 5.2.

The critical density of this device is 1×10^{12}cm^{-2}, and its peak mobility is 308cm^2/Vs. This indicated a significantly worse trap density than for the thermally grown oxide. The shift of the mobility peak to higher carrier density indicates an increase in impurity scattering, probably due to defects at the interface. This is in contrast with previous reports of the mobility in PECVD SiO_2 MOSFETs, with mobilities of up to 1300 cm^2/Vs at 4.2K [109]. This may be due to the surface preparation of the silicon substrate, which has a large effect on the electrical properties of the Si-SiO_2 interface due to the additive nature of deposition compared to thermal oxidation which tends to improve the interface as the silicon is consumed during growth [109].

5.2.2 Atomic Layer Deposition of Al_2O_3

Another method of growing a low temperature dielectric is atomic layer deposition [110–112]. In this method, a sample is sequentially exposed to two precursor gasses, building up a compound dielectric layer by layer. For example, with Aluminium oxide, the gases $2Al(CH_3)_3$ and $3H_2O$ are alternatively exposed to the sample, resulting in the formation of a monolayer of Al_2O_3 on the surface and $6CH_4$ as a bye-product [110, 113]. By repeating this process many times, an arbitrary thickness of oxide can be deposited. ALD, like PECVD, can be performed at low temperature, which limits donor diffusion. However, its advantage is that the thickness of the dielectric layer can be controlled to the monolayer.

Due to these features, the variety of uses of ALD for oxide formation is increasing. ALD Al_2O_3 has been used as a gate dielectric in Si-SiGe heterostructures [114], allowing the 2DEG density to be changed in a linear, instantaneous and non-hysteretic fashion. It has been used in superconducting qubits to form single crystal tunnel barriers, resulting in junctions with very high quality factors [115]. MOSFETs fabricated by ALD of Al_2O_3 on Si(100) have been demonstrated, with mobilities of up to 100cm^2/Vs at room temperature [116].

To investigate the quality of the oxide available, a 50nm layer of Aluminium

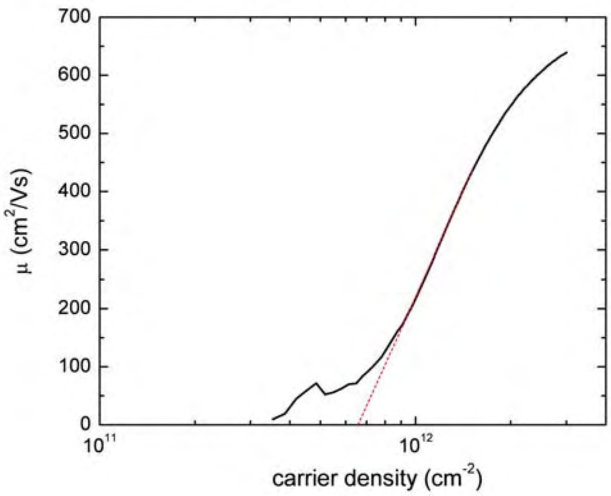

Figure 5.3: Mobility vs carrier density at of a Si-ALD Al_2O_3 MOSFET at 4.2K. T_{OX} = 50nm.

Oxide was deposited, using ALD, onto Si(100) substrates with pre-diffused Phosphorus source and drain ohmic contacts. These wafers were subsequently processed into MOSFETS with a 200nm thick layer of Al as the gate metallization. Following this, low temperature measurements of the mobility as a function of carrier density were undertaken. The results are shown in figure 5.3.

The trap density of the ALD Al_2O_3 MOSFET is 6.6×10^{11} cm^{-2} and the maximum mobility is 639cm^2/Vs . This agrees well with the previously reported mobilities, as a higher mobility at low temperature will be expected.

5.2.3 Comparison of the Different Oxides

In this section, the three different dielectrics are discussed in relation to each other. For comparison, the plots for the three different dielectrics are shown

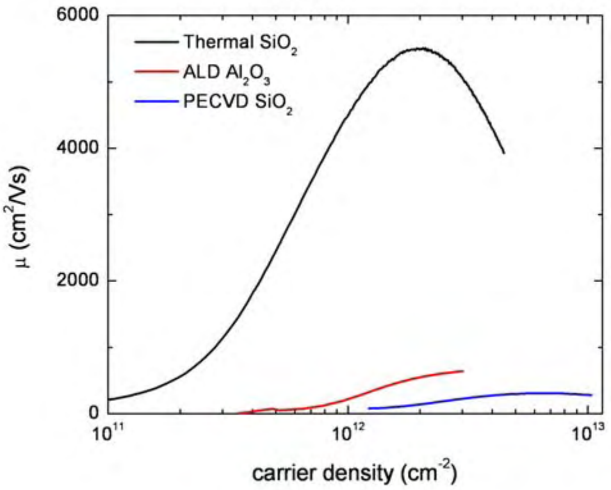

Figure 5.4: μ vs n plots for the three different dielectrics measured.

together in figure 5.4, and the defect density and maximum mobility shown in table 5.1. It is clear from the much lower defect density and higher mobility that if there is no concern for dopant diffusion, a high temperature thermal growth of SiO_2 provides the best properties of the dielectrics studied. Indeed, for most of the work to be presented later in this thesis, the oxide is grown on undoped Si, where diffusion is not a problem, with implantation of donors after oxide growth.

However, the results on ALD Al_2O_3 are promising, and more research into the improvement of this material for use as a barrier when limited dopant diffusion is necessary is warranted. This material may be of benefit in devices where the donors are precisely placed before oxide growth. An example of this is in scanning tunneling microscopy (STM) lithography[117], where the donors can be placed with atomic precision [108, 118]. Any thermal processing after the donor placement will lead to unwanted donor diffusion, mak-

Dielectric	Trap Density 10^{11} cm^{-2}	Maximum Mobility cm^2/Vs
Thermal SiO_2	2.1	5501
PECVD SiO_2	10.3	308
ALD Al_2O_3	6.6	639

Table 5.1: Comparison of the defect density and maximum mobility of MOSFETs with three different dielectric barriers.

ing ALD a highly relevant deposition method. PECVD, which is the worst of the dielectrics investigated, has shown better transport characteristics in other studies, but will require much optimisation of the deposition parameters and surface preparation if it is to compete with thermal SiO_2 .

5.3 Summary

In this chapter, the effect of three different dielectric materials on the low temperature transport properties of Si-MOSFETs has been investigated. Atomic layer deposition of Al_2O_3 is shown to be a viable barrier, and may be of benefit in devices where limited thermal diffusion of dopants is necessary. PECVD SiO_2 may also be used, but the large parameter space in which to optimize the growth conditions are a disadvantage. Of the three barriers investigated, thermal SiO_2 is found to have the lowest defect density and highest mobility, and is thus the dielectric of choice when thermal diffusion of dopants is not a consideration. As such, thermal SiO_2 was chosen as the preferred dielectric for the remainder of the experiments reported in this thesis.

Acknowledgements

The author wishes to thank Edward Laird, Department of Physics, Harvard University, for the deposition of the Al_2O_3 and Chris Kaalund, School of Electrical Engineering and Telecommunications , UNSW, for the deposition of the PECVD SiO_2 .

Chapter 6

Electrically Detected Magnetic Resonance of ion implanted Si:P nanostructures

This chapter looks at the detection of magnetic resonance via its effect on the photoconductivity of ion implanted Si nanostructures. It investigates the effects of various experimental parameters on the observed signal. Devices designed to allow detection of a small number of spins by restriction of current are discussed. These devices are demonstrated to allow the detection of electron spin resonance from ~ 100*) donors.*

Parts of this chapter have been published as:

Electrically detected magnetic resonance in ion-implanted Si:P nanostructures
D. R. McCamey, H. Huebl, M. S. Brandt, W. D. Hutchison, J. C. McCallum, and R. G. Clark and A. R. Hamilton
Applied Physics Letters **89**, 182115 (2006)

6.1 Motivation

With the interest in using ion implanted Si:P for spin based QIP [19, 26], it is important that the spin properties of the system, such as phase coherence and spin lifetimes, be well understood. As an example, recent work by Schenkel *et al* [119] has shown that the choice of ion implantation parameters can influence the phase coherence time of the donor electron of antimony in silicon, which must be considered when fabrication of QC devices via ion implantation is proposed. However, since standard ESR is limited in sensitivity to $\sim 10^9 - 10^{10}$ spins [40, 55], experiments using this method are only possible on systems with a large number of spins. This problem can be overcome by detecting magnetic resonance via the effects of spin selection rules on other observables, such as magnetic force [57], radiative transitions [120], or charge transport [58, 72, 121].

One such technique, electrically-detected magnetic resonance, detects ESR by its effect on the conductivity of a sample (see chapter 2 for a detailed introduction). This method has the advantage of being able to detect the signal from far fewer spins than conventional ESR [72]. However, the study of Si:P via EDMR has previously been limited to samples with bulk doping [60, 63], or to samples with very high dose (metallic) implants [68]. In this chapter, the detection of EDMR in silicon doped by low-dose low-energy ion implantation is reported. Also reported is a method to reduce the number of donors that can be detected by masking the implant area to reduce the number of donors implanted into the substrate.

This work is also motivated by experiments currently being undertaken in the Centre for Quantum Computer Technology at the University of New South Wales [27, 83, 122–125]. The aim of this work is to investigate the movement of charge between locally doped silicon regions, with the ultimate aim of moving a single electron between two individual P donors in silicon. A challenge for this task is the ability to determine the source of the observed charge motion: donor-to-donor, defect-to-donor or defect-to-defect are all possibilities which are presently determined by inductive reasoning. The use of a resonant technique that allows the spectroscopic determination (such as through the unique value of the hyperfine coupling) of the donor species which contributes to the observed signal will be beneficial to these experiments. Whilst EDMR may not in itself achieve this result, experimental work in this are will inform researcher, and perhaps lead to a useful method of spectroscopically identifying the source of the charge movement in the experiments listed above.

6.2 Concept

EDMR is a sensitive probe of spin resonance as it can be restricted to flow completely through the material being investigated. Thus, restriction of the current to a very small sample are containing few spins should allow detection EDMR of small number of spins in the small sample volume. To achieve this restriction, nanoscale devices fabricated by ion implantation will be used to provide current restriction to small areas of lightly doped silicon (Section 6.3). By scaling the lead size with the size of the sample volume, the number of spins that can be detected should be able to be reduced (Section 6.8).

6.3 Fabrication

For this study, devices consisting of metallic doped Si:P leads leading to the non metallic doped sample region were used (see figure 6.1).

Devices were fabricated on a high resistivity (> 8kΩ.cm) n-type silicon wafers. Firstly, ohmic contacts for the source and drain leads of the device were defined via phosphorous diffusion (see figure 6.1). A 5 nm gate oxide was then grown using a wet oxidation process. High-resolution TiPt (20 nm Ti, 15 nm Pt) alignment markers, 100 nm x 100 nm in dimension, were defined by electron-beam lithography (EBL). These markers were used to align subsequent EBL steps with an accuracy of 50nm, and are able to withstand rapid thermal annealing. A 150 nm poly-methyl-methacrylate (PMMA) resist was applied and patterned by EBL for use as a mask for ion implantation of the leads.

Phosphorus ions at 14 keV were implanted with an areal dose of approximately 1×10^{14} cm^{-2} (maximum actual doping, approximately 5×10^{19} cm^{-3})and a mean implantation depth $\sim$20nm. The straggle associated with implantation at this energy is $\sim$7nm [84].

This process was then repeated for the sample region, but the implant was reduced to 5×10^{11} cm^{-2}, giving a maximum donor density of approximately 2×10^{17} cm^{-3}. For a number of samples, the second EBL step was omitted, resulting in implantation all over the wafer, and a number of devices had no second implantation. These three types of devices are referred to as " implanted", "field-implanted" and "control" devices. For clarity, this device naming convention is is shown schematically in figure 6.2.

Finally, Al/Au contacts to the diffused regions were fabricated.

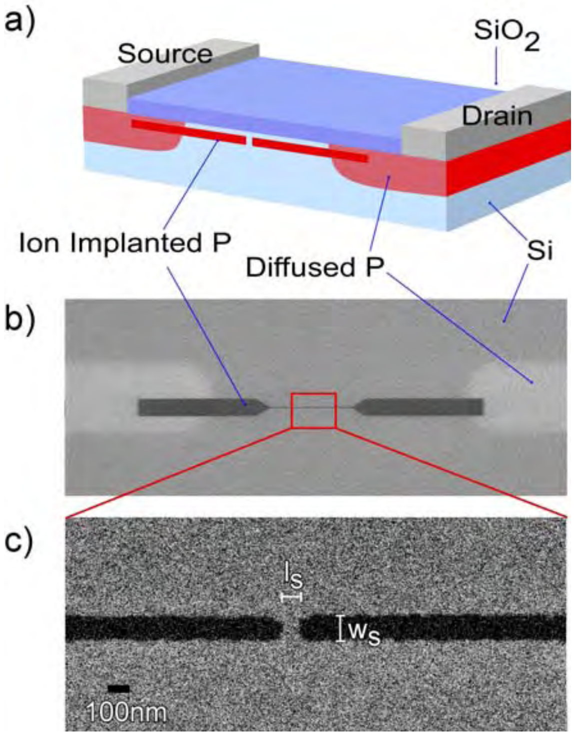

Figure 6.1: a) A schematic of the completed device showing P diffusion and implated region. The sample region, of size $l_s \times w_s$, is between the implanted leads. b)SEM (top view) of the device showing the implanted leads pre-RTA, and c) an expanded SEM (top view) of the sample region.

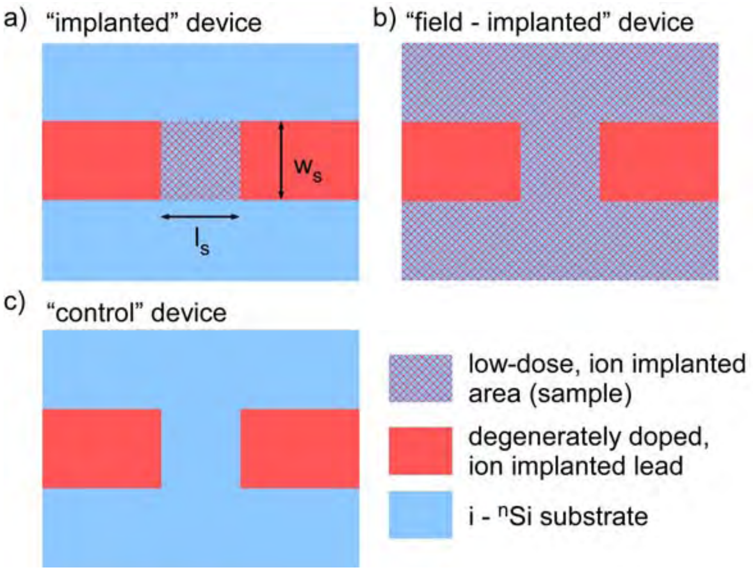

Figure 6.2: Schematic representation of the sample area (top view) in a) a ”mask-implanted”, b) a ”field-implanted” and c) ”control” devices. The solid blocks represent the degenerately doped source and drain leads. The hashed area is the area that was implanted with the second, low dose implant in each case.

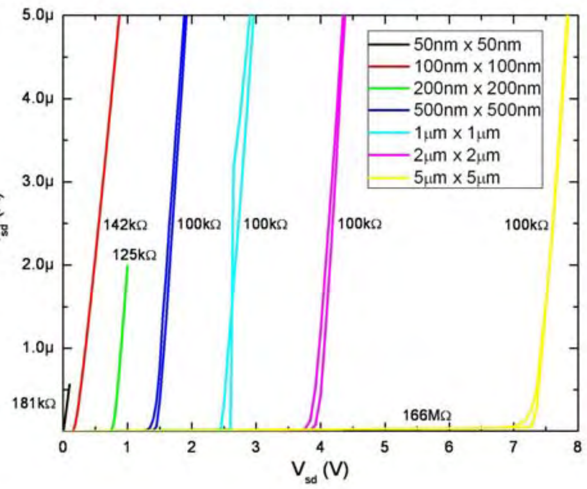

Figure 6.3: IV characteristics of intrinsic (control) EDMR devices at 4.2K for different sample area size.

6.4 Device Testing

Measuring the IV characteristics of the devices at 4.2K and with no light confirms that the leads work as expected. Figure 6.3 shows the IV characteristics of samples fabricated on intrinsic wafers. The IV characteristic is non-ohmic for all but the device with a 50nm gap, which is ohmic.

The 50nm gap device is ohmic as the sample region is connected due to the straggle of the implanted leads, which has been seen previously [82]. The resistance of the leads is approximately $180k\Omega$.

Focusing, on the 1um sample as an example of the remaining devices, we see that for bias voltages less than 2.5V there is no current through the sample. Above this voltage, the sample conducts ohmically, with a resistance $\sim 100k\Omega$. The same resistance is seen for all sample sizes between 500nm and 5um, indicating that the resistance is dominated by the gap region.

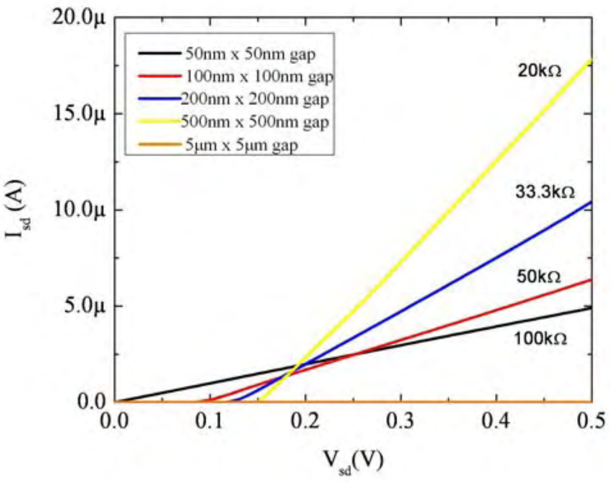

Figure 6.4: IV characteristics of bulk doped EDMR devices at 4.2K for different sample area size.

The IV characteristics of the bulk doped samples, shown in figure 6.4, are different In this case, the turn on voltage is an order of magnitude smaller than for the implanted devices, and the resistance increases as the sample size decreases. This can be explained by avalanche breakdown across the gap, which explains the increase of turn on voltage with gap size, after which the resistance of the device is dominated by the lead resistance. This gives a lead conductance per unit width of $\sim 200nS/nm$.

EDMR signal size from a device perspective

It is important that the dominant source of resistance is determined, as this will greatly effect the signal seen. Since the change in resistance of the sample, ΔR_{sample} is measured, and the resistance is given by $R_{sample} + R_{leads}$, the change in total resistance when ESR conditions are satisfied is given by:

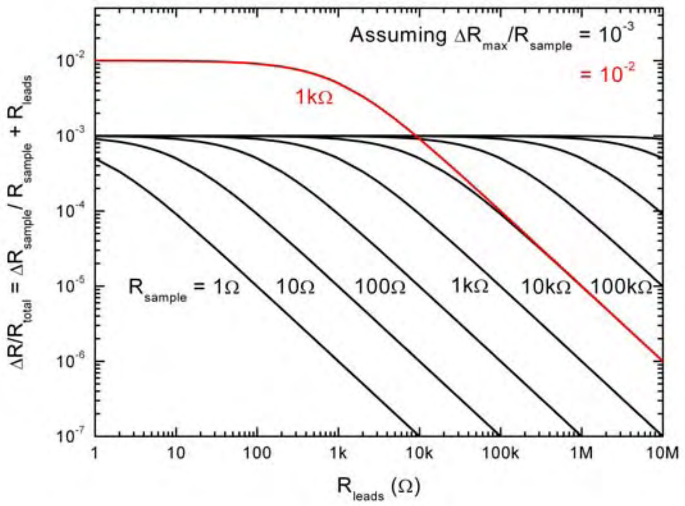

Figure 6.5: Effect of lead resistance and sample resistance on the observed change in the resistance of the system.

$$\Delta R/R = \Delta R_{sample}/(R_{sample} + R_{leads}) \tag{6.1}$$

If we assume that the change in resistance of the sample is constant, then the ratio of the sample resistance to the lead resistance is important, as it determines the maximum change in the resistance of the system that can be observed. This is illustrated in figure 6.5, where $\Delta\ R/R$ for the system is shown as a function of the lead resistance for different sample resistances.

According to this analysis, to obtain the maximum signal it is important that ratio of the lead resistance to the sample area resistance be as small as possible.

6.5 EDMR of bulk P doped silicon

As an initial test of the ability to use EDMR on Si:P devices, samples were fabricated on silicon wafers grown with a P doping density [P]= 10^{17} cm^{-2}. The measurement setup and technique was outlined in section 3.3. An EDMR signal from these samples is shown in figure 6.6. Three main resonances are present. The two resonances at 345.2mT and 349.4mT, separated by 4.2mT, are from ensembles of single donors. The two lines arise from the hyperfine coupling of the donor electron with the spin 1/2 nucleus. This leads to a splitting of the line by 4.2mT, as discussed in section 2.1. The central line is due to strongly exchange coupled pairs of P donors (exchange coupling energy $>$ hyperfine interaction energy) which leads to an effective nuclear spin of zero when the two P pairs have opposite spin. Phenomenologically, one can consider the electron to be moving back and forth between the two donors much faster than the larmor frequency, in effect experiencing an average nuclear spin of zero over the course of the measurement.

Note that in the case where the spins of the two exchange coupled donors are not opposite, the average spin is either $1/2$ or $-1/2$ and the resonance aligns with the single donor resonance. Higher order exchange coupled groupings can occur (e.g. three closely coupled donors) [45] but these clusters are statistically unlikely to form at these doping densities [61].

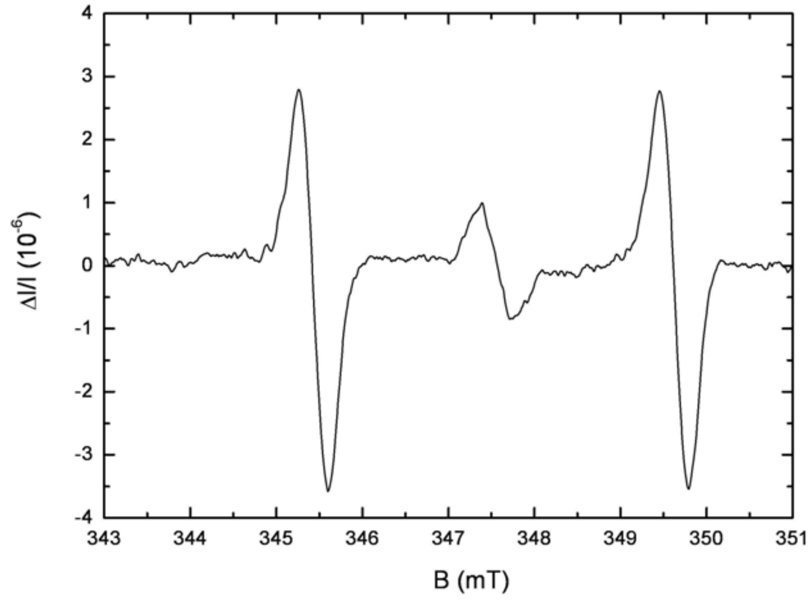

Figure 6.6: The EDMR signal from bulk P doped Si. The two hyperfine P lines are split by 4.20 mT, as expected.

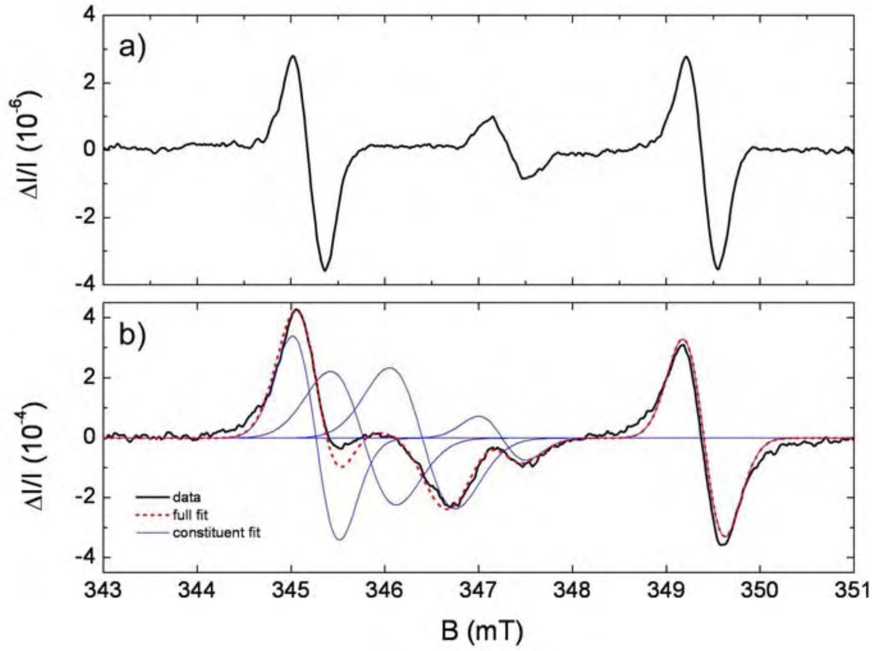

Figure 6.7: a) Bulk doped substrate with implanted leads and b) Intrinsic substrate with field implant and leads. The red dashed line is a fit to the spectra, and the blue lines each of the individual resonances used in the fit. The most obvious difference is the additional resoannces between 345mT and 347mT, which are attributed to the P_b defect. The details are discussed in the text.

6.6 Comparison of Bulk Doped and Implantation Doped Devices

Figure 6.7 shows the comparison between a bulk doped and field implanted device. In the field-implanted sample, the two P lines with a hyperfine splitting of 4.2mT are again visible. There are however two clear differences in the data. Firstly, the two additional resonances at $B = 346.4$ and $B = 345.8mT$ which are present in the field-implanted device but not the bulk doped device. These two resonances are attributed to the P_{b0} and P_{b1} defects [126, 127]. These defects are due to silicon dangling bonds at the silicon-silicon dioxide interface, with the different g-factors resulting from the different crystallographic directions in which the dangling bond points [126]. Due to the nature of the defect, any future reference to the P_b defect should be taken to be a reference to all of the P_b , P_{b0} and P_{b1} defects unless explicitly stated.

Next, the magnitude of the observed signal is much larger in the field-implanted sample when compared to the bulk doped sample. To explain this difference, we must consider the difference in the conductivity of the two devices, which was discussed in section 6.4. The sample region of the bulk doped device has a much smaller resistance than the sample region of the field-implanted device. Equation 6.1 shows that this decrease in the sample resistance will lead to a decrease in the observed signal in the bulk doped sample. However, due to the inability to determine the actual resistance in the presence of the applied light, this difference is not able to be quantified.

An alternate explanation is that the mechanism by which EDMR is observed in the bulk doped sample is different from that in the field-implanted sample. This is supported by the lack of a P_b defect signal in the bulk doped sample. Since the KSM model described in section 2.6 requires a photoexcited carrier to recombine through a phosphorus-Pb defect pair, the P_b resonance should be visible in the EDMR spectra. This is the case in the field-implanted samples, where the P and P_b resonances have a similar magnitude. However, the lack of a P_b resonance in the bulk samples indicates that the EDMR mechanism differs from the KSM model. Indeed, there are other mechanisms, such as the Lepine model of EDMR [73] or bolometric detection of ESR [128], which do not require the photoexcited electron to recombine through a pair of carriers.

6.7 Characterising EDMR of ion-implanted P donors in Si

Little work has gone into characterisation of the effect of various experimental parameters on the observed EDMR signal in Si:P. In this section, common parameters are investigated in a phenomenological approach, informing the experimental parameters to be used in later work. The parameters investigated here are Bias Voltage, Measurement Frequency and Measurement Temperature.

6.7.1 Effect of Bias Voltage

This section will investigate the effect of the magnitude of the current flowing through a device on the EDMR signal seen. Figure 6.8 shows the EDMR spectra obtained for an implanted sample, under illumination, with two different currents flowing.

Due to the complicated nature of the spectra at low field due to the over-

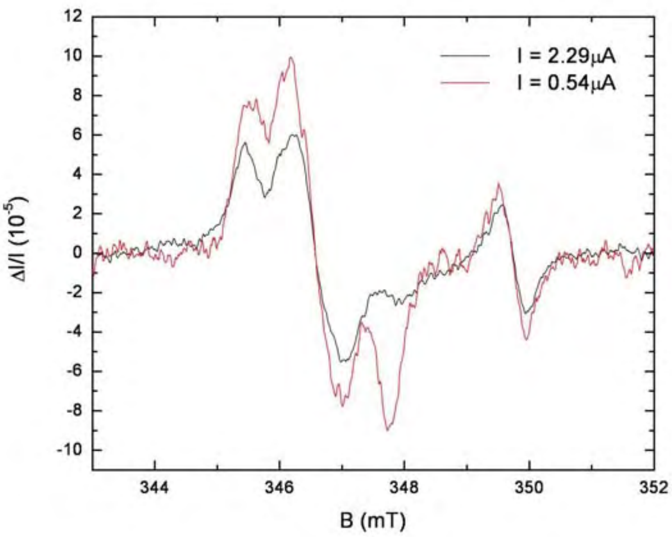

Figure 6.8: The EDMR signal from an implanted sample with two different currents, $I = 2.29\mu$A (black)and $I = 0.54\mu$A (red).

lapping spectra of the P_b defect resonances and the low field P resonance, the high-field P resonance will be used for comparing the different spectra.

In figure 6.9a, ΔI/I for the high field resonance is shown in more detail. Figure 6.9b shows the absolute change in current, ΔI, for the two spectra.

The relative change in signal, ΔI/I is constant, whereas the absolute change in current, ΔI, scales with the absolute current, I. This is expected from the discussion given in section 2.6, where the change in the recombination rate leads to a change in the relative current, ΔI/I . This suggests that for larger absolute changes in signal (which should be easier to detect), it is best to have larger absolute currents.

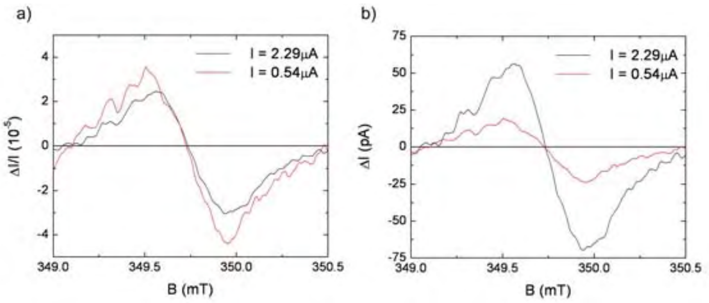

Figure 6.9: a) The relative change in current, ΔI/I , and b) the absolute change in current Δ I, of the high field P resonance for two different values of I, 2.29μA (black)and 0.54μA (red).

6.7.2 Effect of Measurement Frequency

An important characteristic of any electrical measurement is how the measurement changes with frequency. In EDMR, the frequency dependence is able to provide information about the recombination times of the spin dependant processes that are being investigated [129]. However, it is important that the measurement of frequency dependent phenomena is not dominated by the characteristic times related to the RC time constant of the measurement setup.

It has been shown [129], that for a recombination process with characteristic time τ_r, the signal amplitude scales as

$$(\Delta I/I)_{max} = S_{max}((\omega\tau)^2 + 1)^{-1} \tag{6.2}$$

where S_{max} is the maximum amplitude at the low frequency limit and ω is the angular modulation frequency of the B field.

Figure 6.11 shows a plot of the maximum peak height of the high field P signal as a function of measurement frequency. Also shown is the fit to this data of the form given in Equation 6.2 above. The fit yields $S_{max} = 6.5 \pm 0.8 \times 10^{-4}$ and $\tau_r = 7.5 \pm 3\mu s$.

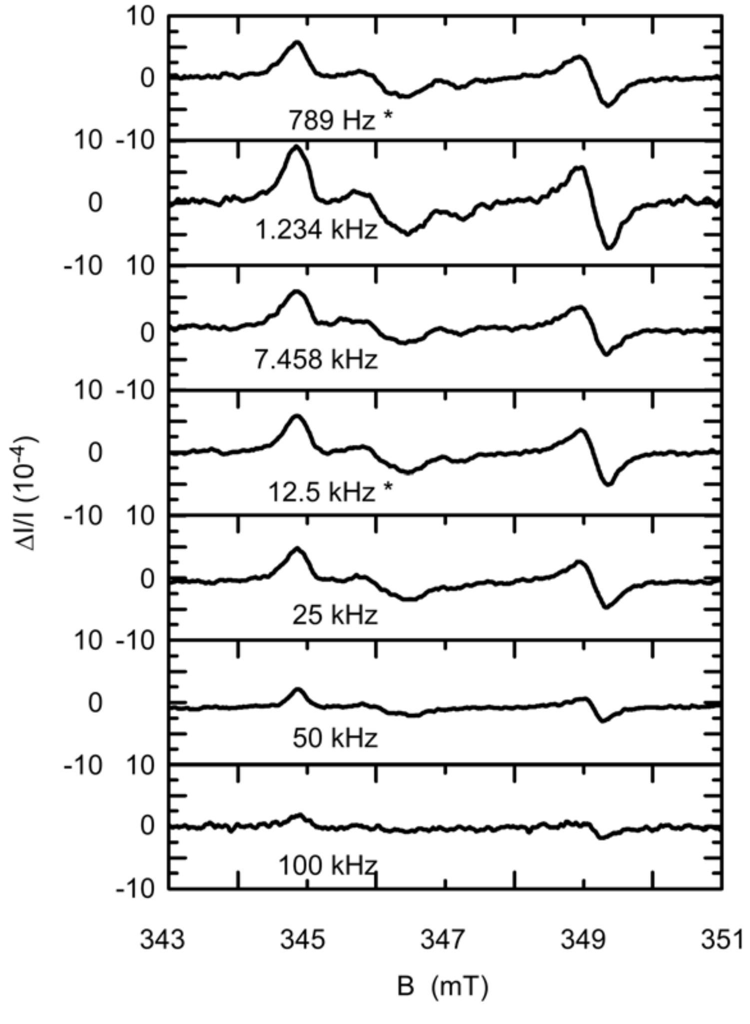

Figure 6.10: The EDMR signal from ion implanted Si:P for different B-field modulation frequencies, measured at T= 5K. The two traces marked with a $*$ were measured in a different measurement run.

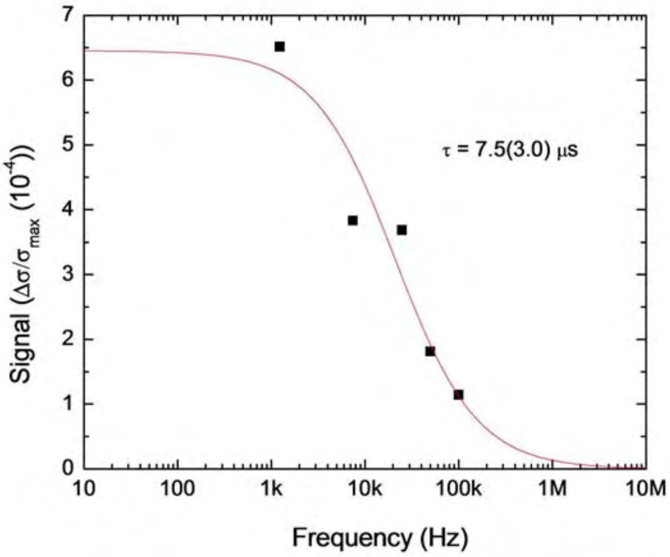

Figure 6.11: The signal size of the high field P line as a function of measurement frequency.

However, if this is the case, it is important to remove the possibility that the decrease in signal is due to the RC time of the system. The sample used for the above measurements has a resistance of order $1M\Omega$. The characteristic time, $7.5\mu s$, would require the device capacitance to be much smaller than 10 pF to be able to exclude the RC constant as the source of the observed decrease in signal. However, this value is a quite reasonable value for the system (comprising the sample as well as the connecting wires). Further work will be required to unambiguously determine the source of the frequency dependence.

From these measurements, it is seen that the best frequencies to measure the EDMR signal is at frequencies below 20kHz. In light of this result, future measurements will be undertaken with $\mathrm{B}_{\mathrm{mod}} = 1$kHz, unless specifically stated.

6.7.3 Effect of Temperature

The temperature dependence of the measured EDMR signal for a field implant is shown in figure 6.12. Focusing on the high field resonance, the strength of the resonance is seen to decrease as the temperature is increased from 5K to 30K. However, in this range the P_b resonance does not change appreciably. The signal amplitude of the high field P is shown in figure 6.13.

The data was fit with functions of the form $\Delta I/I = AT^n$ and $\Delta I/I = Ae^{(-T/T1)}$; of these it was best fit with an exponential decay of the form

$$\Delta\ I/I = (1.30 \pm 0.05) \times 10^{-4}[e^{(-T/10.6 \pm 1.2)}] \tag{6.3}$$

The characteristic temperature for the decrease in the signal, T= 10K, equates to an energy of 0.8meV. This energy scale is not associated with any characteristic energies of the system: electron ($\sim\ 37\mu\ eV$)or nuclear ($\sim$ 20neV) zeeman, donor electron binding energy ($\sim\ 44meV$), or hyperfine interaction ($\sim 0.48\mu\ eV$).

Morooka *et al* [130] have previously investigated the effects of temperature on the ESR signal from bulk doped Si:P with a doping density of $1.3 \times 10^{17}\text{cm}^{-3}$. They observe a peak in the intensity of the hyperfine split lines at 11K, which becomes smaller as the temperature is moved away from this point. They attribute this dependence to the change in the relaxation time of the P donor electrons, which in turn effects the magnetic susceptibility of the system. However, in EDMR where the susceptibility of the system is not important to the detection of a signal, we must look further for the source of the temperature dependence.

Dugdale *et al* [131] have also investigated the temperature dependence of the hyperfine signal. They observe a decrease in the hyperfine splitting as the

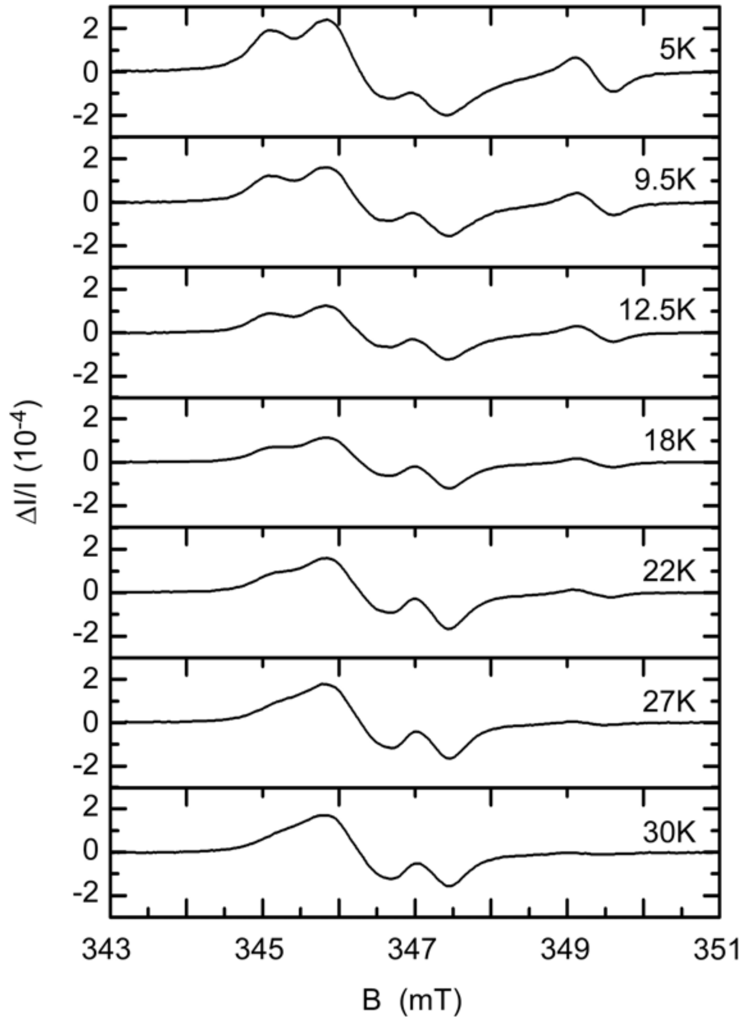

Figure 6.12: The effect of measurement temperature on the observed EDMR signal of Si:P.

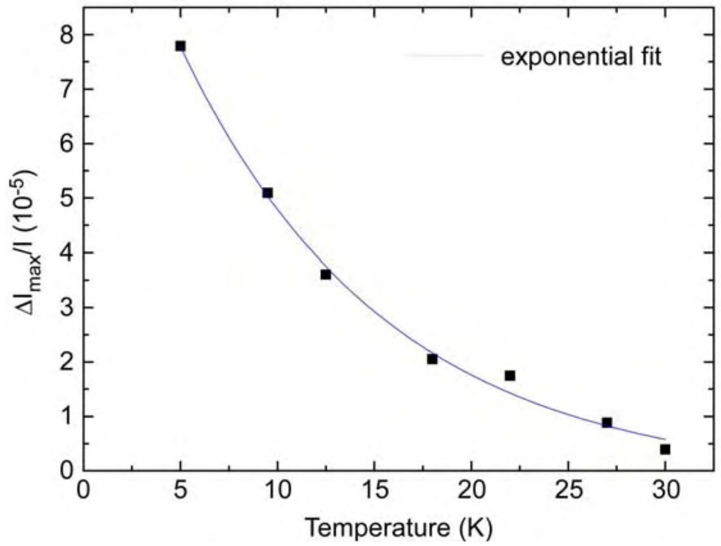

Figure 6.13: High field P resonance amplitude as a function of measurement temperature. The Blue line is an exponential fit.

temperature is increased, which they attribute to motional averaging due to the donor electron hopping rate between donors increasing with temperature. However, large changes in the magnitude of the hyperfine splitting, up to 1mT, are also observed. No shift is seen in the measurements presented here.

A reasonable explaination for the decrease in the resonance amplitude is a decrease in the coherence time of the donor electrons. Feher [51] demonstarted that the decoherence rate of the donor electron has a T^7 dependence in the temperature range 3-4K. This rapid decrease in coherence time in the vicinity of 10K leads to a large decrease in the observed resonance signal, due to the spin lifetime becoming much shorter than the measurement time.

The measurements presented in this section have focused on the phenomenological effect of various measurement parmeters with the aim of increasing the signal quality. It is seen that the best parameters involve using low frequency

($\sim$1kHz) B field modulation, low temperature (e.g. 5K) and high current. This information will allow effective collection of future EDMR spectra.

6.8 Decrease of number of donors

This section investigates in detail the implanted device type. These devices, which use a PMMA mask to ensure that P is implanted only into the sample region between the implanted leads, allow the number of donors that are being investigated to be determined precisely. Previous measurements to determine the number of donors have required that the measurement region be estimated. This problem is overcome by implanting a (statistically) known number of donors into the sample region of the device.

Figure 6.14a is the spectra from a field-implanted sample, which was discussed in detail in section 6.6 above, and is shown here for comparison purposes. Figure 6.14b shows the relative current change for a mask-implanted device with $w_s = l_s = 100$ nm. The number of P implanted into the active region is 50±8, as determined from the implant parameters. Even with such a small number of phosphorus donors in the active region, an EDMR signal intensity given by the peak-to-peak current change of the high-field hyperfine-split P resonance of $\Delta I/I = 1.5 \times 10^{-5}$ is easily detectable. The defect signal observed in the mask-implanted samples is dominated by a single resonance at $g = 2.005$, characteristic of the dangling bond signal widely observed at Si/SiO$_2$ interfaces [132].

Due to the use of P in the lead fabrication, the effect of the straggle of the lead implantation in contributing donors to the active sample area must be taken into account. Figure 6.14c shows the EDMR signal from a control device,

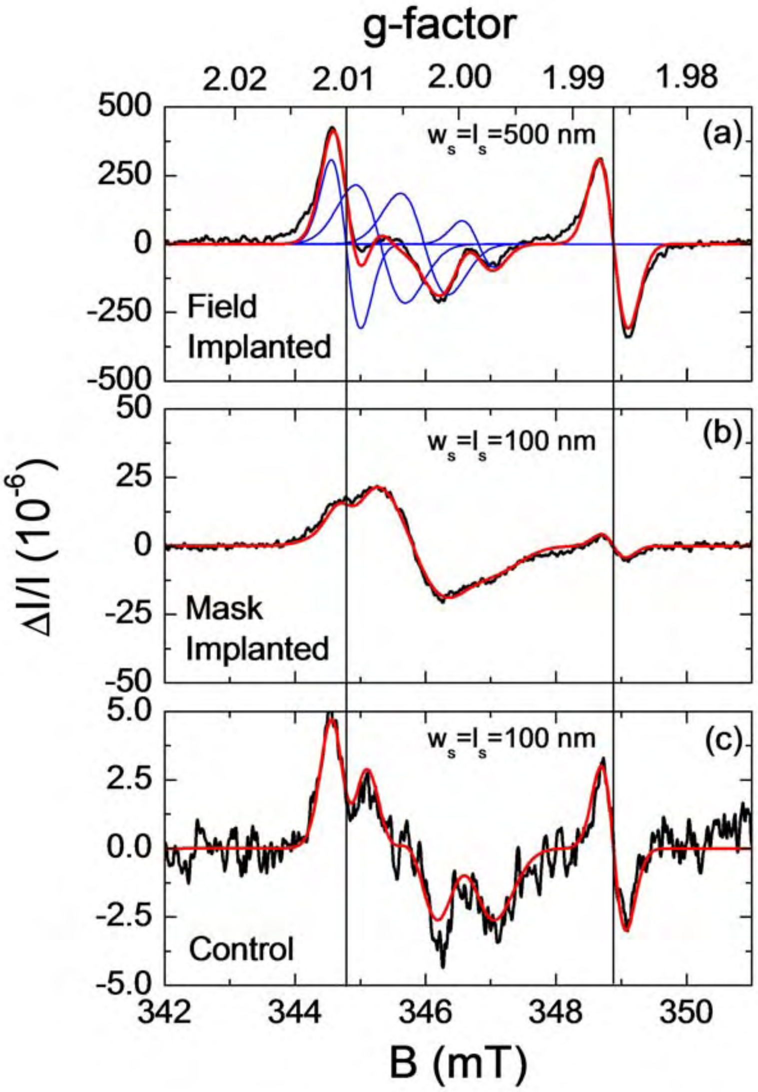

Figure 6.14: EDMR signal I / I vs magnetic field for (a) a type 1 sample with $w_s = l_s =$ 500nm and (b) a type 2 and (c) a type 3 device both with ws=ls=100 nm. The red lines are fits to the experiment. The blue lines in (a) show the constituent lines of the fit. The constituent line at B=349 mT completely coincides with the full fit, and is therefore not visible.

also with $w_s = l_s = 100$ nm, where there is no second implant of P into the gap area. The characteristic signature of hyperfine-split P is still observable, however with a smaller $\Delta I/I = 6 \times 10^{-6}$. This signal is due to the straggle of the leads, which will now be consider in detail.

Effect of Lead Straggle

Spin-dependent hopping in Si:P at very high P concentrations has been studied in detail, including samples where P incorporation was obtained by implantation [68, 133]. An increase of the dark conductivity was observed under ESR conditions at the central, exchange coupled resonance with $g \approx 1.9985$ [134] for metallically doped samples, with typical values for $|\Delta I/I|$ decreasing from $10^{-5} - 10^{-7}$ at [P]$\simeq 6 \times 10^{18}$ cm^{-3} to 10^{-10} at [P]$>$ 3×10^{19} cm^{-3} [68, 135, 136]. Therefore, a contribution from the leads in these experiments will be limited to the central line at $g = 1.9985$ due to the high doping concentration. In contrast, hyperfine-split lines can only arise from P with a local concentration below 10^{18} cm^{-3} [137]. The amount of P with [P]$\leq 10^{18}$ cm^{-3} in a control device with $w_s = l_s = 100$ nm in the sample area between the leads and due to straggle can be estimated from SRIM simulations[84] for these implantation parameters to be about 50 ± 8 considering the surface of the leads facing the sample area. Finally, due to the overlap of the two implantation processes a total of about 85 ± 10 P donors in the sample area from the leads and the secondary implant are present in the implanted device with $w_s = l_s = 100$ nm.

Since resonant changes in the photoconductivity are monitored, the possibility of diffusive transport and spin-dependent recombination throughout the whole sample cannot be neglected. To study this quantitatively, $\Delta I/I$ is determined as a function of the size of the device. Figure 6.15 shows the EDMR

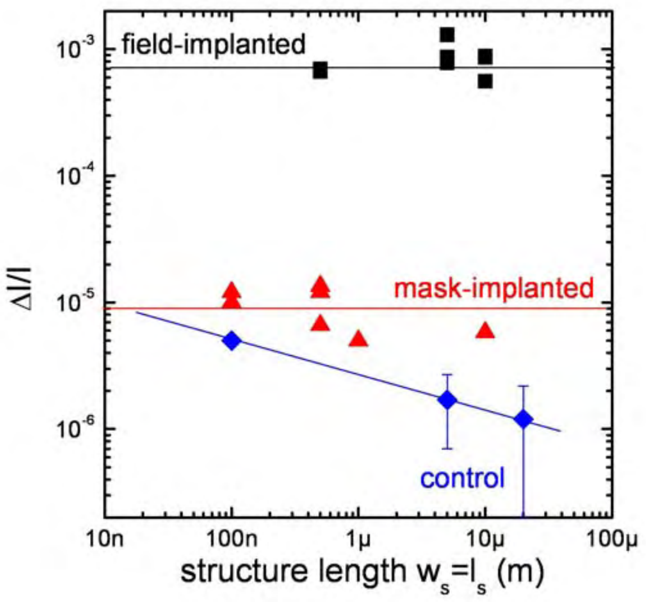

Figure 6.15: Scaling of the EDMR signal intensity ($\Delta\ I/I$) with varying structure size w_s for a series of devices of all three types investigated. The lines are guides to the eyes.

signal intensity of the P hyperfine-split peak at $B = 348.88$ mT for all types of samples as a function of $w_s = l_s$. Notably, the EDMR intensities of the mask-implanted and field-implanted devices cluster at $\Delta I/I \approx 10^{-3}$ and at $\Delta I/I \approx 10^{-5}$ respectively, independent of $w_s = l_s$. Due to Ohm's law and the quadratic geometry of the gap, the resistance of each type of device studied in a purely drift based model is independent of the characteristic size and therefore the resonant changes in the current should indeed be size independent. This demonstrates that with the restriction of the current path to areas containing few P donors, Pauli-blockade effects lead to an effective influence of the transport properties of the device. Differences in the EDMR signal intensities between the different device types are expected due to the different areas implanted with P and the current path not being restricted completely to the gap area. Where multiple measurements were performed, the spread of $\Delta I/I$ for fixed sample size of a given type is less than 40%. However, the fact that in the experiments on control devices, a significant spin-dependent recombination is only observed for the smallest structure length, where the relative contribution of the straggle to the P donors in the sample area is largest, clearly indicates that the P donors in the active area contribute most to the EDMR signal, while the recombination near the leads or diffused contacts only plays a minor part.

6.8.1 Noise Considerations for Single Spin Detection

To show that single spin detection is possible with this technique, we consider the signal-to-noise ratio S/N of the spectra measured and determine from them a signal-to-noise ratio $S/N|_1$ for a single magnetic field scan based on

Poisson statistics:

$$S/N|_1 = S/N|_n/\sqrt{n} \tag{6.4}$$

where n is the number of measurements averaged.

This yields a typical $S/N|_1 \approx 5$ for field-implanted and $S/N|_1 \approx 0.5$ for mask-implanted samples, again independent of size. If the independence of the signal intensity on the structure length persists at smaller lengths, single P donors could be monitored in mask-implanted samples with $w_s = l_s = 14$ nm at the same S/N ratio. Fabrication of devices at this scale is achievable with modest improvements to the current implantation scheme.

The relative signal intensities of the P_{b0} and the P hyperfine-split lines found in our experiments on ion implanted samples are of the same order of magnitude, independent of the overall signal intensity and the type of the device. This provides further evidence that the spin-dependent recombination process investigated is indeed a P-P_{b0} pair process, where a photogenerated excess electron is captured by a P donor and forms a spin pair with a P_{b0} defect, a process also proposed as a readout scheme for silicon QIP hardware[138]. Furthermore, P-P_{b0} pair recombination can only occur near the Si/SiO$_2$ interface, and therefore any P donors in the bulk of the sample, underneath the implanted leads and the diffused contacts do not contribute to the EDMR signal.

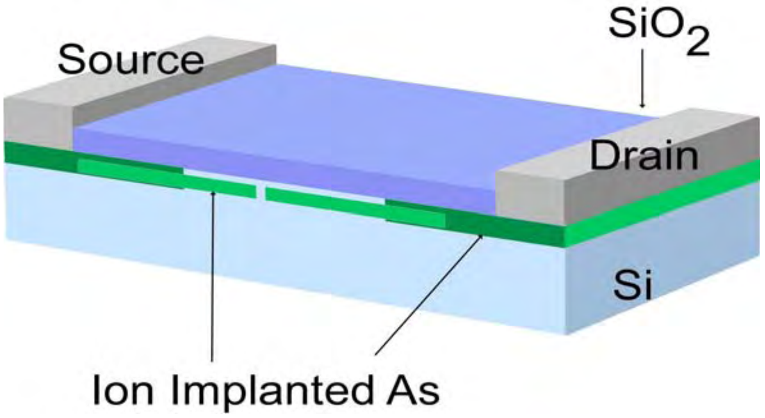

Figure 6.16: Schematic of the devices with Arsenic source-drain leads. The two different implantations are shown. The sample region is the region between the source and drain leads.

6.9 Devices with Arsenic Leads to Confirm small number of donors

6.9.1 Concept

Whilst the results shown in figure 6.15 indicate that the signal is in fact due to the low-dose implant into the sample region, further investigations were warranted. One way to do this is to fabricate devices where the donor species used for the ohmic contacts and leads is different from that in the active area, so that any resonance detected can be attributed to the active area unequivocally. Arsenic lends itself to this purpose, as it is a donor in silicon, can be implanted, and has a different hyperfine splitting than phosphorus [28, 139].

6.9.2 Device Fabrication - Implantation of Arsenic Ohmics and Leads

Ion implantation was used to fabricate both the ohmic contacts and nanoscale leads in these samples [1]. The device is shown schematically in figure 6.16. Two different energies were used in the implantation. The first, 15keV, was used for the ohmic implantation, as this resulted in a peak distribution close to the Si-SiO2 interface, providing high quality ohmic contacts. The second energy, 20keV, was chosen for the leads so that they would be at the same depth as the P implanted into the sample region. The metallic region of these two implants intersected in the z direction, ensuring a continuous conducting path between the two implanted regions.

The implantation and incorporation of arsenic was discussed in more detail in section 3.1.3.

Measurements of Devices with As Leads

Figure 6.17a shows the spectra for a device with arsenic leads and 50 implanted donors.

The high field P resonance is clearly visible in the implanted sample, at $B = 348.07$ mT. This resonance is not obviously seen in the control, shown in figure 6.17b. This shows that it is possible to detect the signal from 50 donors via EDMR. However, it is possible that a small signal is present in the noise of the control sample. Even if a signal were observed, this may be due to a small contribution from the very small background doping present in the silicon wafer. The wafer has a background phosphorus density $[P] = 2 \times$

---

[1] We choose to implant the arsenic for safety reasons

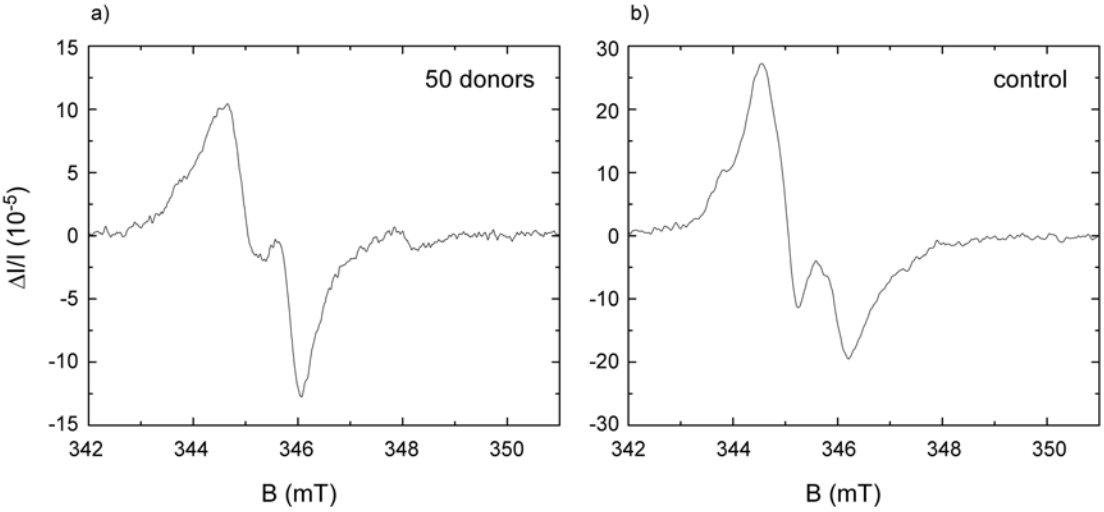

Figure 6.17: $\Delta I/I$ vs B for 0.1μm x 0.1μm devices fabricated on intrinsic ^{n}Si wafers a) with and b) without a non-metallic cluster implant. In these devices, the leads and ohmics are fabricated via ion implantation of arsenic. The high field resonance from the P donors is clearly visible in the 50 donor device, and is not visible in the control.

10^{11}cm^{-3}. The number of donors ion the area between the ohmic contacts ($\sim$ 10μm $\times$ 10μm $\times$ 2μm) at this doping density is expected to be 40. However, the current will flow preferentially through the implanted leads due to the lower resistance. Making the assumption that at most 20% of the current flows around the leads, then there is an effective contribution of 8 P donors to the EDMR signal. This would lead to a small signal being observed. However, the better the constriction of the current to the leads, the smaller this contribution. This suggests a future experiment where more effective detection is obtained by complete restriction of the current to the sample region, which is discussed below.

However, even if there is complete detection of these donors, the the measurements presented in this chapter represent the detection of less than 100 donors, at a level at least 7 orders of magnitude better than standard ESR, and

4 orders of magnitude better than previous EDMR studies of donors in silicon.

6.10 Conclusions

The ability to detect the spins of donors in silicon is fundamental to a number of proposals for quantum computation. By selective implantation of phosphorus into silicon using EBL, a pathway to the spectroscopic study of a small number of donors in semiconductors has been demonstrated. We have shown that it is possible to observe, using reasonably standard techniques, the change in conductivity caused by as few as 100 spins.

It is important to note that this technique is not restricted to P, but can be extended to other dopants, provided the donor electron is able to form a singlet state with the defect electron. This will depend on the energy level structure of the donor, which varies form case to case. It remains to be seen if this technique can be extended to the study of single donors, which would make possible a very interesting set of experiments.

One possibility for improving the signal seen would be to further restrict the current flow through the device. This could be achieved by etching of SOI to provide three dimensional restriction of the current to a small sample area. A proposed architecture is shown in figure 6.18. A device 200nm ×100nm ×25nm thick on material with $[P] = 10^{16}\text{cm}^{-3}$ would contain on average 10 donors, and would also restrict the current to the interface region where the spin dependent recombination process occurs.

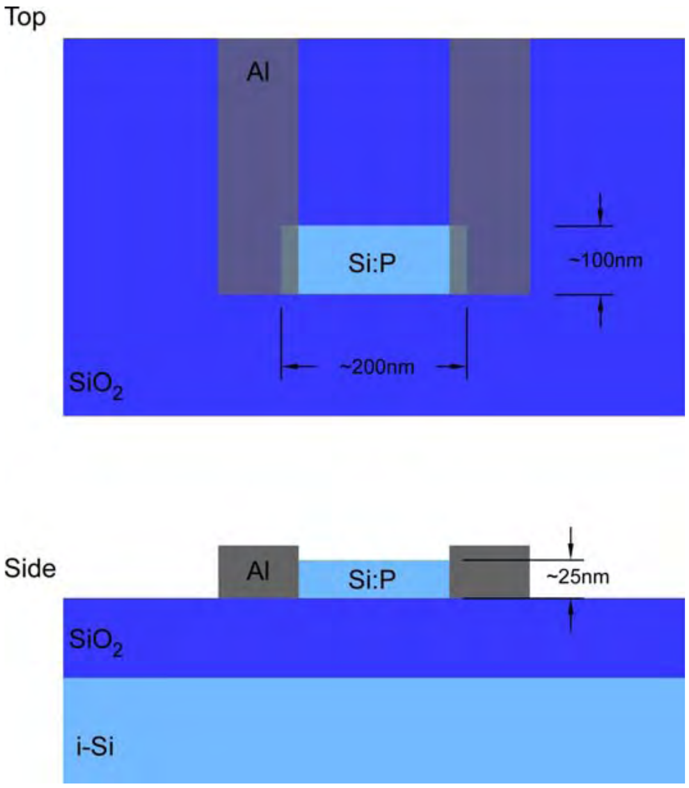

Figure 6.18: Proposed architecture for the elimination of unwanted shunt currents, by etching small islands of Si:P using Silicon-on-insulator material.

6.11 Acknowledgements

The work in this chapter was undertaken in collaboration with researchers at the Walter Schottky Institute of the Technical University of Munich, Germany. The work on the devices with arsenic leads was supported by the Australian Research Council Nanotechnology Network through an Overseas Travel Fellowship.

Chapter 7

EDMR of phosphorus donors in isotopically pure ^{28}Si

This chapter investigates the use of ^{28}*Si for the detection of few spins in the solid state. Properties of the material such as chemical and isotopic purity are investigated, as these factors effect the ability of this material to be used in the detection of small numbers of donors.*

7.1 Introduction

Silicon consists of three natural isotopes. The natural abundance and nuclear spin of these isotopes is shown in table 7.1. This chapter investigates phosphorus doped isotopically purified ^{28}Si in EDMR experiments, and the effect this has on the observed spectra, and the information that can be gained regarding the suitability of this material for spin dependent devices.

In ^{n}Si :P, the relatively large fraction of ^{29}Si with nuclear spin 1/2 leads to the large linewidths observed in the EDMR spectra due to the superhyperfine

Species	Natural Abundance (%)	Nuclear Spin
^{28}Si	92.22%	0
^{29}Si	4.69%	1/2
^{30}Si	3.10%	0

Table 7.1: Natural abundance and nuclear spin of the 3 naturally occurring silicon isotopes[140].

interaction between the dopant and the ^{29}Si nuclei. In contrast to the standard hyperfine interaction, where the donor electron interacts with the donor nuclei, the superhyperfine interaction is due to the interaction of the donor electron the nuclei in the surrounding lattice.

The superhyperfine interaction in silicon is much smaller than the hyperfine interaction. It has a typical strength of less than 0.3mT, compared with 4.2mT for the standard hyperfine interaction. The superhyperfine interaction is manifest in the ESR spectra of Si:P as a broadening of the hyperfine split lines. This results from a slightly different superhyperfine shift of the resonance position of each of the donor electrons due to the random distribution of ^{29}Si atoms in the crystal.

7.2 Material

The material used in these experiments is commercially obtained isotopically purified ^{28}Si, supplied by Isonics Corporation[1]. The isotopic purity is greater that 99.9%. The material is supplied as a 10μm epilayer on a high resistivity

---

[1] http://www.isonics.com/silicon28.htm

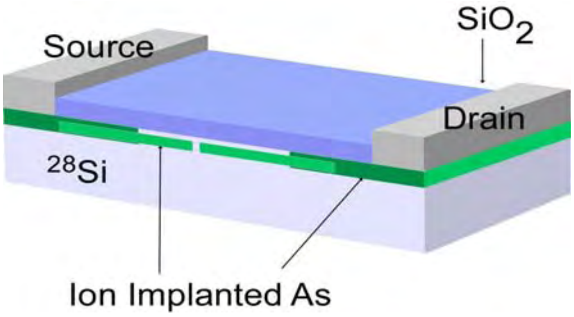

Figure 7.1: Schematic of the devices used for investigation of the intrinsic ^{28}Si .

^{n}Si substrate. The epilayer has a resistivity greater than 800Ω.cm, and the substrate greater than 10 kΩ.cm.

7.3 Fabrication of EDMR devices

To perform EDMR, devices based on those outlined in section 6.9.2 of chapter 6 were fabricated, and are shown schematically in figure 7.1. These devices were fabricated using ion implanted As for both the Ohmic contacts and leads. The naming convention, ″implanted″ and ″control″, is the same as that explained in section 6.3.

7.4 EDMR of ^{28}Si:P

In this section, EDMR measurements of ^{28}Si :P are reported. Figure 7.2 shows the EDMR signal from a 2μm × 2μm implanted sample. The two hyperfine split lines are visible, as is the P_b resonance. However, in contrast to the ^{n}Si samples, the P donor resonances dominate the spectra. This major difference is due to the narrower lionewidth of the observed signal, which is discussed in more detail below.

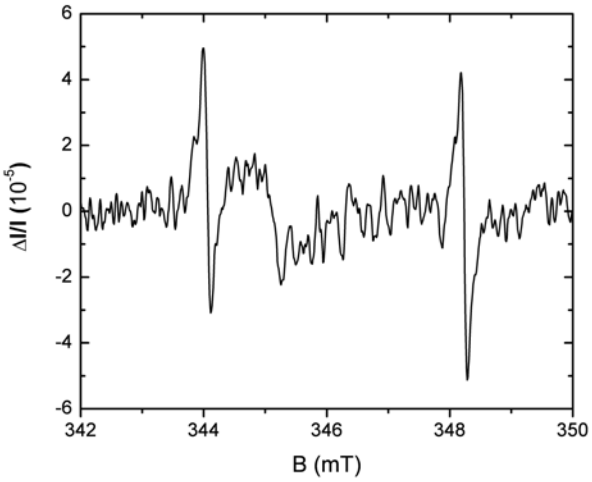

Figure 7.2: EDMR spectra of ion implanted ^{28}Si :P. $P_{\mu \text{wave}}$ = 17dBm, $B_{\text{mod}} = 0.05$mT

7.4.1 The cw-EDMR Linewidth

One way to characterise the purity of ^{28}Si is to measure the linewidth of the P donor resonance. The width of this line is dependent on the fraction of ^{29}Si present, $f =^{29}$ Si/Si, with the linewidth decreasing as $f^{1/2}$ [54] .

However, the linewidth is also dependent on the measurement parameters, including the specific microwave power and B-field modulation used during the measurement. Overmodulation of either of these parameters can result in artificially large linewidths, and as a result it is important that the effect of these two parameters be determined.

Figure 7.3 shows a series of measurements at P_{μ}wave = 17dBm, with 3 different values of B-field modulation, 0.3 mT, 0.1 mT and 0.05 mT. The experimentally observe line width decreases from 0.31 mT to 0.09 mT, showing that the broadening in this case is due to over modulation of the B-field.

To determine the smallest observable line width, a series of measurements

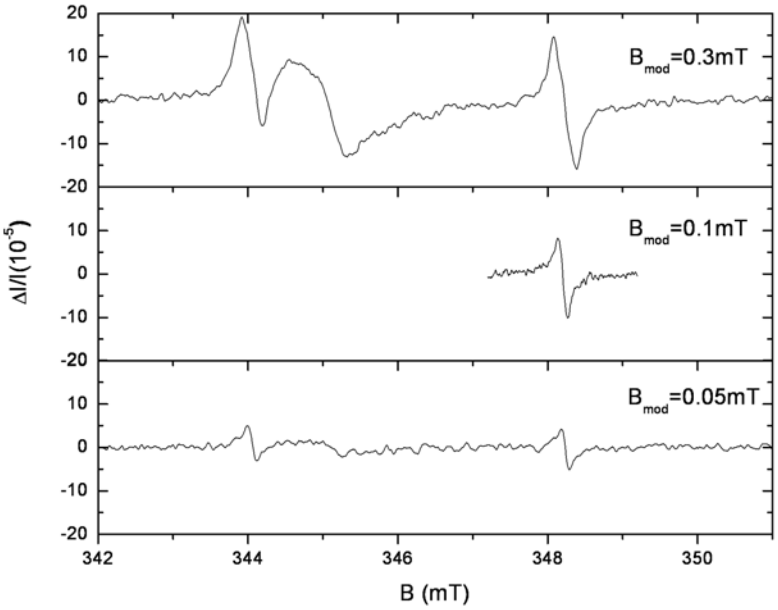

Figure 7.3: EDMR signal as a function of the B field modulation amplitude, with P_{μ}wave $= 17$dBm.

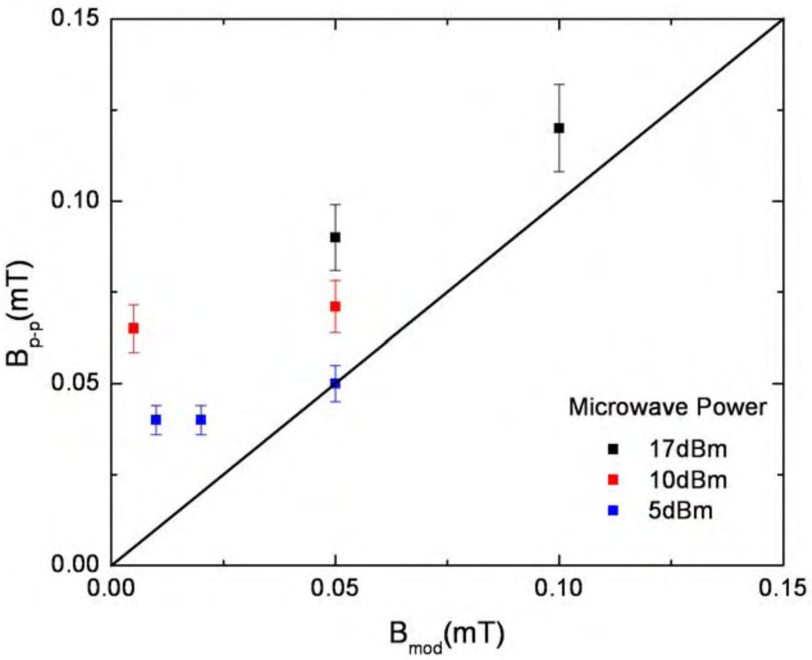

Figure 7.4: High field P linewidth as a function of both B field modulation and microwave power.

were taken, varying both the microwave power and B-field modulation amplitude. The linewidths of the high field P signal obtained from these measurements is shown in figure 7.4. Both the power and the modulation serve to increase the measured line width. However, the smallest line width observed has B_{p-p} = 0.04 mT, measured at 5dBm with $B_{mod} = 0.01$mT. Using the data in reference [54], this equates to a ^{28}Si fraction of 0.999, in good agreement with the manufacturers claimed purity of 0.999 [141]. However, this linewidth may still be broadened by the microwave power, indicating that 0.999 is the lower limit for the ^{28}Si fraction.

From the linewidth measurements, we can also place a lower limit on the phase coherence time of the ^{28}Si:P donor electrons. A line width of 0.04mT at 330mT equates to a minimum coherence time of 850ns. This compares poorly with recent pulsed ESR measurements on ^{28}Si:P, which indicate coherence times of up to 62ms at 6.9K [31] for P densities of 10^{16}cm^{-3}. This may indicate that the linewidth being measured is still being broadened by the high microwave power necessary tpo obtain a signal. This is supported by the fact that decreasing the power in this regime always results in a lower linewidth.

The ability to measure narrower linewidths by continuing to reduce the power and modulation is limited by the length of time it takes to obtain a spectra with good signal-to-noise ratio. The spectra with the smallest linewidth has $S/N|_1 = 0.086$. This measurement required 840 averages to obtain $S/N|_{840} = 2.5$. To decrease the time taken to obtain this data, the external magnetic field range was restricted to a small 1mT window around the high field peak and the sweep time was reduced to 50 seconds. However, this measurement still took longer than 11.7 hours to complete. The decreasingly small signals obtained show that this method is unsuitable for determining the intrinsic T_2 limited linewidth, and a more appropriate method for determining the phase coherence times, such as the Hahn spin echo technique [142], is required.

However, recent pulsed-EDMR measurements [77, 143] of the Rabi oscillations of ^{n}Si:P have shown that the limiting factor in the coherence of systems probed using EDMR is the recombination of the donor electron with the P$_b$ centre. The recombination of the donor electron, which allows the EDMR signal to be observed, is also an effective measurement of the quantum state. This causes the loss of phase information, leading to an increase in the effective decoherence rate of the ensemble of spins. The measured recombination times in the those experiments, of order $2\mu s$, are very similar to the decoherence rate obtained from the cw-EDMR linewidths in the experiments discussed above.

The implication of these measurements is that, to measure long coherence times using EDMR, it will be necessary to stop the electrons from recombining during the period of spin manipulation. This could be achieved by performing the spin manipulation in the dark, followed by illuminating the sample to measure the spin state via EDMR. This will lead to a more complicated signal, as the initial generation of carriers will provide a very large current transient.

7.5 Few spins samples in ^{28}Si

This section tries to determine if the number sensitivity seen in the previous chapter is achievable using isotopically purified material.

Measurements on implanted sample with 50 implanted donors in the gap were undertaken, as well as corresponding measurements on control samples.

Figure 7.5 shows the EDMR signal from an implanted sample with $w_s = l_s =$ 100nm, containing 50 donors. As measurement induced broadening the spectra will not effect the results obtained, we choose to use a higher modulation amplitude (0.1mT) and microwave power (17 dBm) to provide faster measurement times.

Clearly visible in the spectra are the two hyperfine split P lines, as well as a smaller defect resonance at the P_b location. The maximum signal amplitude, $\Delta I_{max}/I \approx 9 \times 10^{-6}$. The narrow line widths, $\mathrm{B}_{p-p} \sim$ 0.15mT, indicate that the signal is indeed from donors in the ^{28}Si epilayer. This spectra has $\mathrm{S/N}|_1 =$ 1.05, which is much higher than that measured for the devices fabricated from natural silicon.

However, similar measurements on a control samples with $w_s = l_s =$

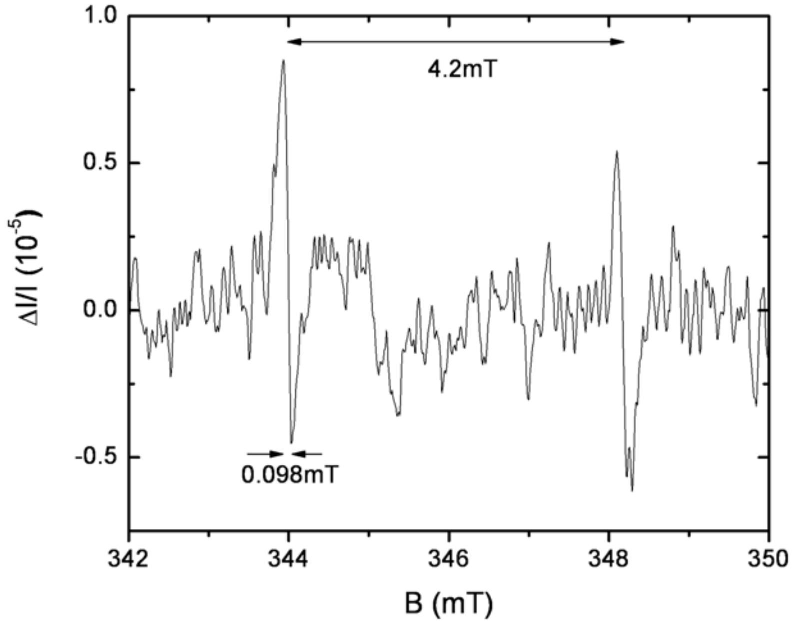

Figure 7.5: EDMR signal from an implanted ^{28}Si sample with $w_s = l_s = 100$nm containing 50 implanted donors in the sample region. The line broadening is due to overmodulation of the B-field, with $B_{\text{mod}} = 0.1$mT. The signal was averaged 20 times.

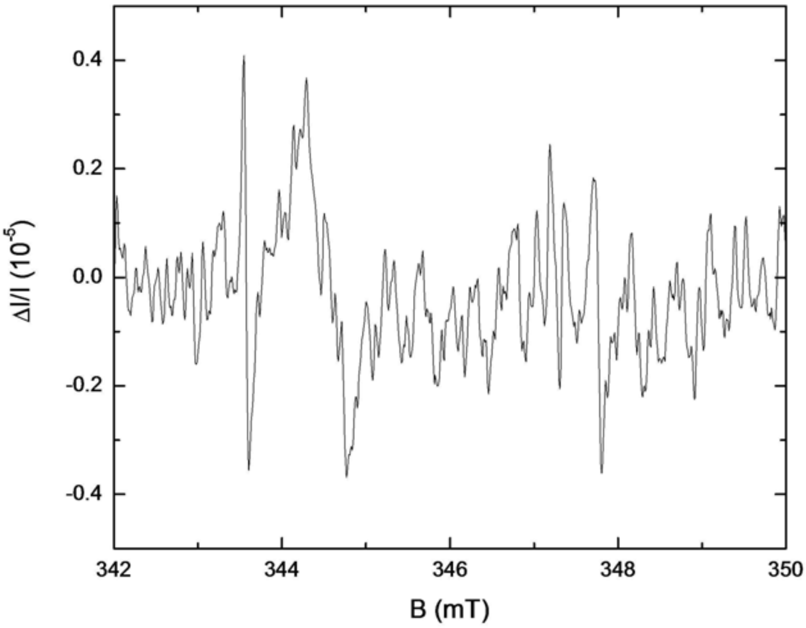

Figure 7.6: EDMR signal from a control ^{28}Si sample with $w_s = l_s = 100$nm containing no implanted donors in the sample region. The measurement was performed with $B_{\text{mod}} = 0.02$mT. The signal was averaged 40 times.

100nm (figure 7.6and $w_s = l_s = 1\mu$m (figure 7.7)also show similar results. The two hyperfine split P lines are again clearly visible, with $\text{S/N}|_1 = 0.56$ in the 100nm sample and $\text{S/N}|_1 = 0.43$ in the 1μm sample.

The fact that the Si:P resonance is seen in both mask-implanted and control samples indicates that the source of the resonance is not the donors implanted into the sample region, but P that was unintentionally present in the material.

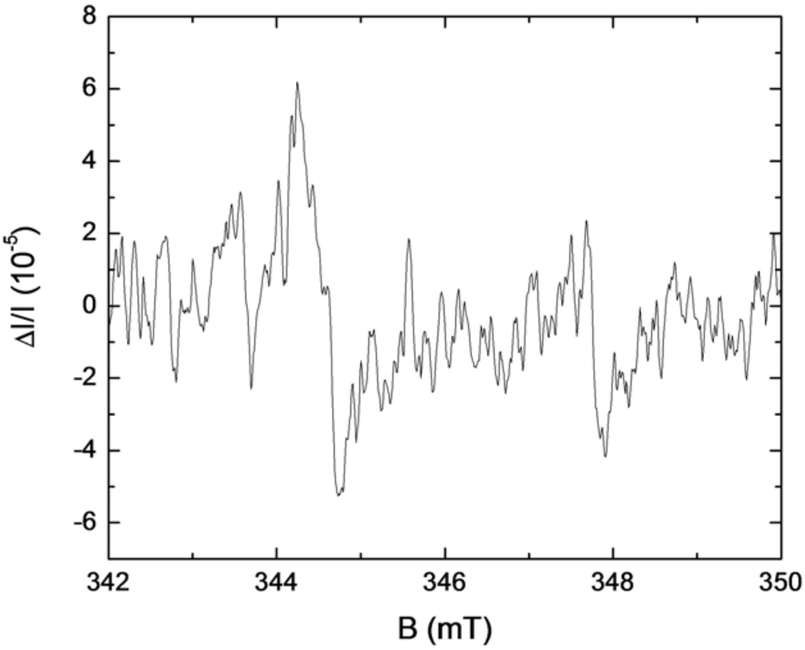

Figure 7.7: EDMR signal from a control ^{28}Si sample with $w_s = l_s = 1\mu$m containing no implanted donors in the sample region. The measurement was performed with $B_{\text{mod}} = 0.1$mT. The signal was averaged 100 times.

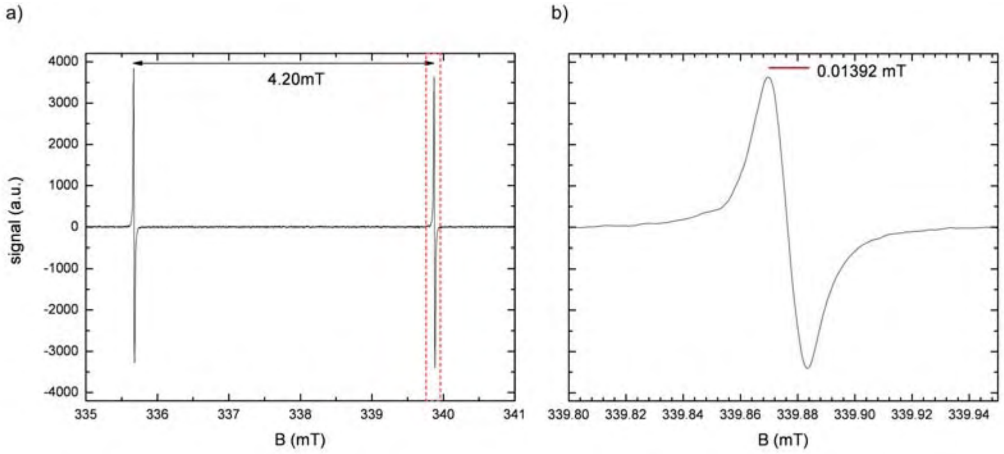

Figure 7.8: Conventional ESR of a 10μm ^{28}Si epilayer with [P] $= 10^{16}$cm^{-3}.

7.6 Conventional ESR on ^{28}Si

To further understand the the results indicating the presence of donors in the nominally undoped samples reported in section 7.5, the materials properties of the isotopically purified ^{28}Si was investigated with conventional ESR. Conventional measurements of the isotopically purified ^{28}Si:P was undertaken on material with a high background doping and material with nominally no doping. The material was measured in a standard Brucker ESR system. The results of these investigations are outlined below.

ESR of intentionally doped ^{28}Si ($[P] = 10^{16}$ cm^{-3})

Figure 7.8 shows the ESR spectrum for ^{28}Si:P doped to a density of 10^{16}P/cm^3.

These measurements show the standard 4.2mT hyperfine split P resonances. The two P resonances have a linewidth of 13.9μT.

ESR of nominally intrinsic ^{28}Si ($[P] = 0$)

Control measurements were also performed on nominally undoped epilayers of ^{28}Si . As there are no donors present in this sample, there should be no hyperfine P signal.

However, a signal was also observed in these samples. The width of the resonance ($\sim$ 0.01mT) indicates that the signal is from P donors in the ^{28}Si epilayer, as line widths of $\sim$ 0.3mT are expected from any donors in the ^{n}Si handle wafer due to inhomogeneous broadening of the resonance by ^{29}Si nuclear spins.

Comparison of the intensity of the P resonances with the defect resonance, and assuming a defect density of $2 \times 10^{11}\text{cm}^{-2}$ as determined in chapter 3, indicates that there is a background density of $\sim 2 \times 10^{1}3\text{P/cm}^{3}$. Resistivity measurements of the epilayer also give a similar doping level($\sim$ 800Ω.cm), which corresponds to a doping density of $\sim 6 \times 10^{1}2\text{P/cm}^{3}$.[22]

It is important to consider the implications of this level of doping on the signal seen in the ^{28}Si device, with the aim of looking at few donor EDMR. It is important to remember that the unintentional doping density of the intrinsic ^{n}Si handle (which was used for the devices presented in the last chapter) is less than $2 \times 10^{11}\text{P/cm}^{3}$.

Using these two densities, the number of donors expected in a 10um × 10um × 2um region (which is approximately the area between the diffused ohmic contacts in the devices used) is 40 and 4000, for intrinsic ^{n}Si and intrinsic ^{28}Si respectively. When we consider that a small amount of the current in the devices studied in the previous chapter will diffuse from one contact to the other around the implanted leads, the presence of 4000 donors in this area will greatly effect the signal that is seen. Making a simple assumption that the

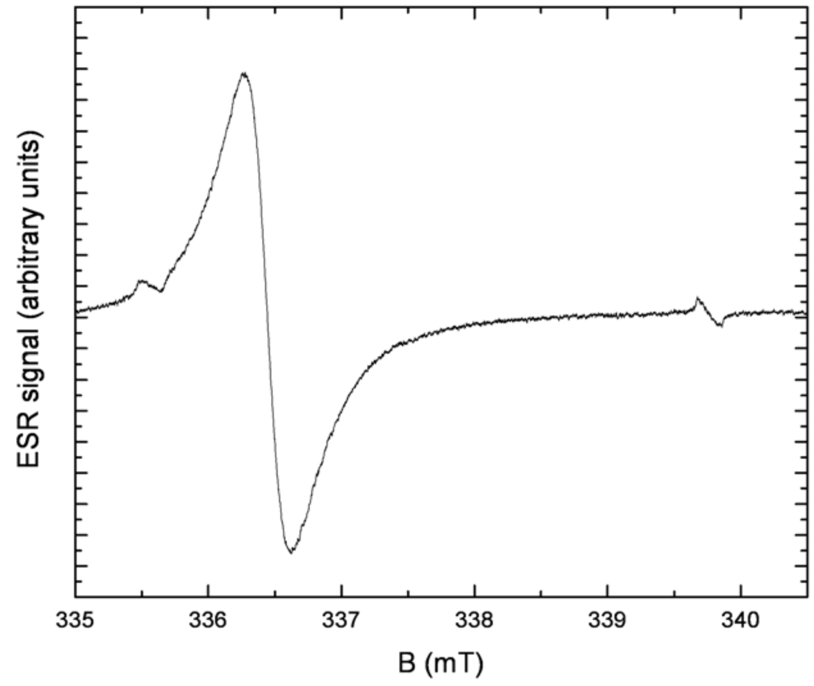

Figure 7.9: Conventional ESR of nominally undoped ($\sim 850\Omega$.cm))^{28}Si. $B_{mod} = 0.2mT$.

effective contribution from this area is 10% of the signal, the number of donors in the ^{n}Si case is effectively 4, which is negligible when compared to the 50 donors in the gap. However, in the ^{28}Si , this equates to 400 effective donors, which dominates over the 50 donors, making similar experiments impossible.

This background doping explains the reason that no difference is noted in the EDMR signal from the implanted and control ^{28}Si devices presented above.

However, this does not preclude the use of isotopically enriched ^{28}Si for few donor measurements. By further restricting the current through the sample, the effect of the unintentional background doping can be reduced. In fact, in a 100nm $\times$ 100nm $\times$ 15nm sample region there is on average only 0.006 donors in an unimplanted ^{28}Si device, indicating that the measurement is possible with more effective current restriction.

7.7 Future Improvement of the Method

The measurements above have shown that impurity concentration of currently available isotopically purified ^{28}Si is too low to perform measurements on small number of spins in the way presented in this thesis. However, there may be ways to achieve this using different device architecture. One of these would be to use very small volumes of Si to limit the number of donors present.

The growth of isotopically purified ^{28}Si nanowires has been demonstrated [144], which would provide the required small volume. These wires have radii as small as 10nm. At a standard doping density of 10^{16}cm^{-3}, a 1 $\mu\ m$ long wire of this diameter will contain on average only 3.1 donors.

Also, the wire radius is only 4.2 Bohr radii ($a_{Bohr} = 2.38$nm [145, 146]). Thus, a single P donor will extend over 5.6% of the cross sectional area of the wire. This large relative spatial extent, along with the complete restriction of the current to the nanowire, should lead to large changes in the current on resonance, making detection of EDMR easier.

7.8 Conclusions

In this chapter, EDMR of phosphorus in isotopically purified ^{28}Si was reported. The small resonance linewidth ($B_{p-p} < 0.04mT$)) verified that the signal seen was from phosphorus donors in silicon with isotopic purity was greater 99.9%. However, both EDMR and standard ESR measurements suggest that the material has an unintentional background phosphorus concentration of order 10^{13} cm^3, which prevents the detection of a small number of donors in this material. However, more effective restriction, by using Si nanowires for example, should allow these measurements to be performed.

7.9 Acknowledgements

This chapter described work undertaken at the Walter Schottky Institute of the Technical University of Munich, Germany, in collaboration with the Spin Physics Group. The work was supported by an Overseas Travel Fellowship from the Australian Research Council Nanotechnology Network. The conventional ESR measurements described in section 7.6 were performed by W. Hutchison at the Australian Defence Force Academy, Canberra.

Chapter 8

Pulsed Electrically Detected Magnetic Resonance of Ion Implanted Si:P nanostructures

This chapter reports results of pulsed EDMR measurements on ion implanted nanostructures. These measurements are the first reported p-EDMR measurements on implanted donors, and represent an important step towards electrical detection of the coherent manipulation of few donors in the solid state.

Of particular interest to the quantum computing community is the ability to control the quantum state of spins in the solid state. The ability to measure the effect of this manipulation on a small number of spins is an important step to the realisation of a spin based quantum computer. The ability to manipulate an ensemble of spins is well established, with pulsed-ESR (p-ESR)a model implementation. However, whilst p-ESR is good at manipulating and detecting the spins of large ensembles, and even manipulating manipulating single spins [56], it is unable to detect the spin state of a small number of spins.

Pulsed EDMR has the advantage over pulsed ESR in that the signal from

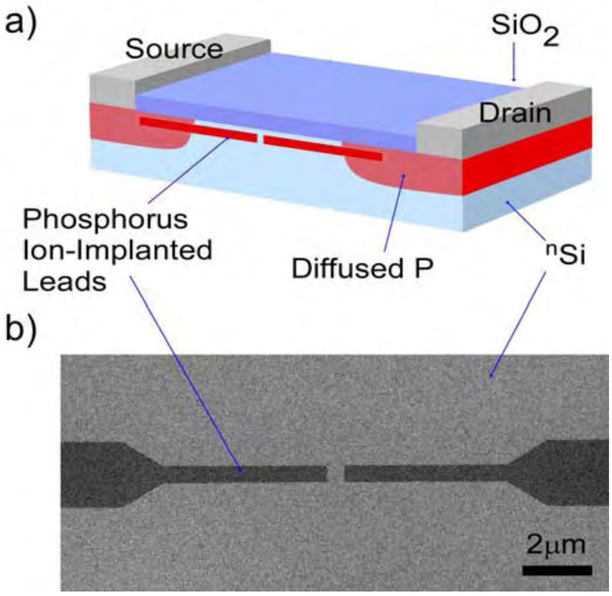

Figure 8.1: a) A schematic of the device used for the p-EDMR measurements. The device used was a field implanted device with $w_s = l_s =$ 500nm. b) SEM of the leads pre-RTA in a similar device.

a small number of spin should be observable, due to the reasons outlined in chapter 2. p-EDMR has recently been demonstrated on bulk doped ^{n}Si :P samples by Stegner *et al*[77, 143]. In this section, the first pulsed EDMR measurement of ion-implanted ^{n}Si :P is reported. This forms a logical progression of the work presented by Stegner *et al* [77], as ion implanted Si:P forms the basis of a number of promising QC architectures [19, 26].

The samples fabricated for the cw-EDMR experiments presented in chapter 6 were used to demonstrate the feasibility of p-EDMR in implanted structures. Samples with a low dose field implant of P were used as these samples showed the largest signal ($\Delta\ I/I$) in cw-EDMR measurements. These are shown schematically in figure 8.1.

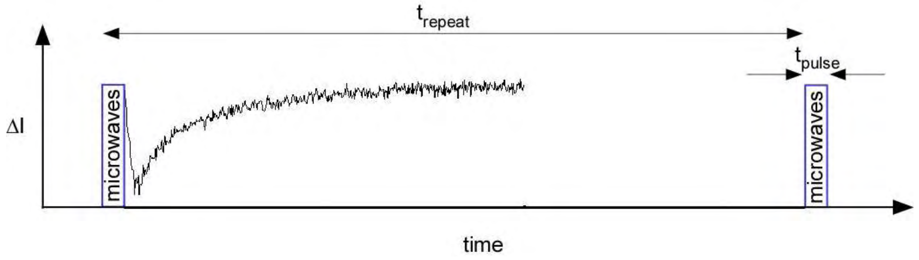

Figure 8.2: Outline of the pulse timing for the p-EDMR measurements. In the experiment reported in this chapter, $t_{\text{repeat}} = 170\mu s$ and $t_{\text{pulse}} = 350ns$.

8.1 Measurement Details

To perform the p-EDMR measurements, the sample was placed into an external magnetic field, which was swept from 342.7mT to 352.7mT in 128 steps. A bias of 1.88V was applied to the source of the sample, and the drain was connected to a Femto amplifier.

At each point of the sweep, high power microwaves ($f = 9.725$GHz) were pulsed for 350ns. The current through the sample was recorded for 100μ s, and the measurement repeated every 170μs. The measurement process is shown schematically in figure 8.2 The result of 500 shots was averaged at each point, and the magnetic field sweep was repeated and averaged 350 times.

To obtain the p-EDMR signal, the background (non-resonant) transient signal of the device was subtracted from each measured signal. The resulting transient map is shown in figure 8.3.

8.2 Proof of Concept Measurements

Figure 8.3 shows the transient signal as a function of both magnetic field and time after pulse. The data is from a field-implanted device with $w_s = l_s =$

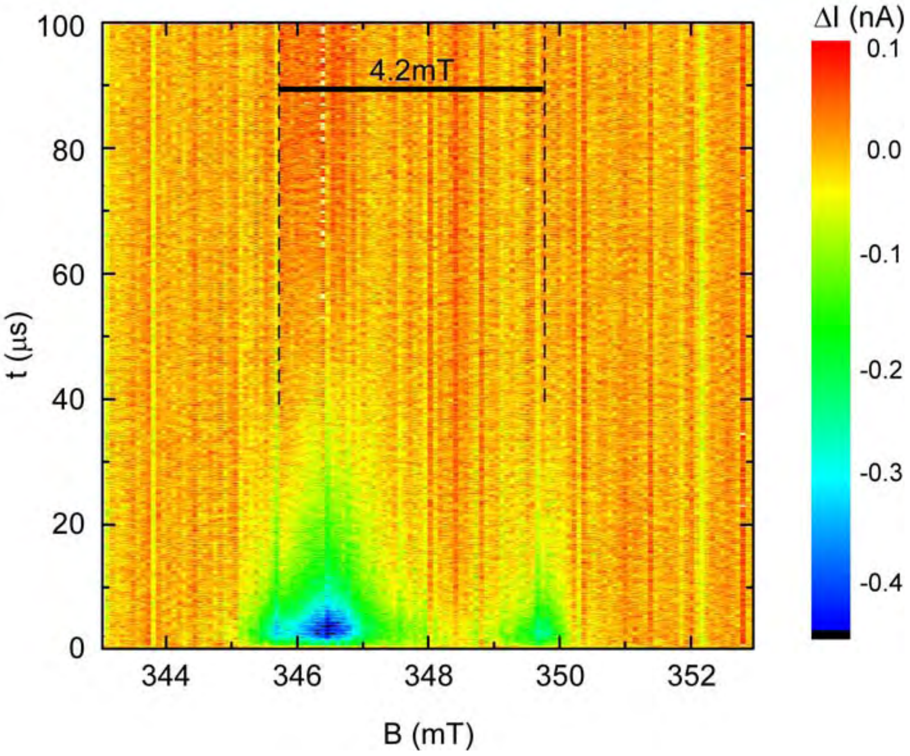

Figure 8.3: Current transient Δ I vs B for 0.5μm x 0.5μm devices measured after a 350 ns microwave pulse.

500nm, implanted with an areal phosphorus dose of 10^{12} cm^{-2}. The easiest way to interpret this map is to take two slices through it, in both the time and field direction. I will look first at a slice through the map at $t = 2.6\mu$s, which is shown in figure 8.4.

Figure 8.4 shows what is in effect a standard EDMR spectra. Clearly visible at B = 349.8±0.2mT is the high-field P resonance, with the corresponding low-field resonance visible at 345.7±0.2mT, a separation of 4.1±0.4mT, as expected from the hyperfine splitting of P in silicon. The large feature at B= 346.5 ± 0.4mT, which overlaps with the low field P resonance is identified as the P_b defect, as in the spectra measured in the cw-EDMR experiments

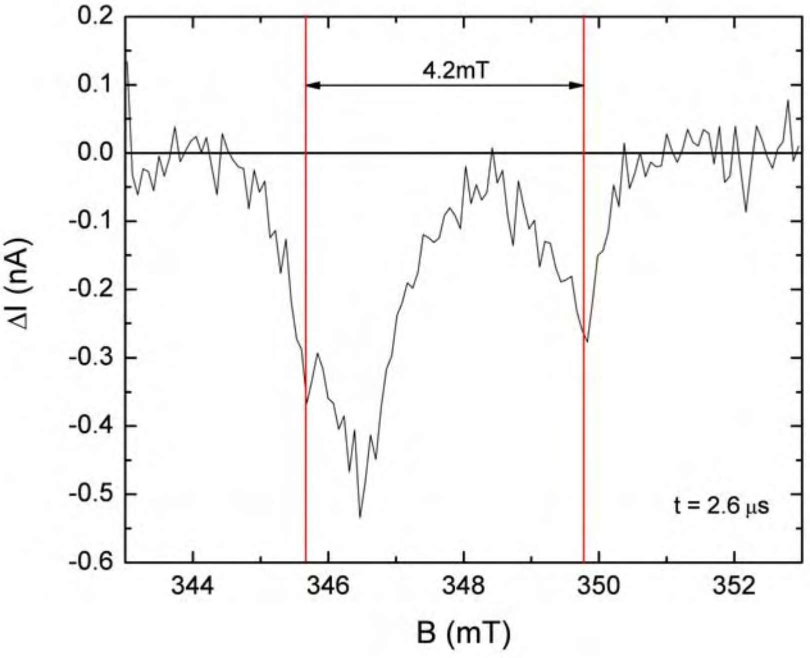

Figure 8.4: Slice through the pulsed EDMR spectra at $t = 2.6 \mu s$.

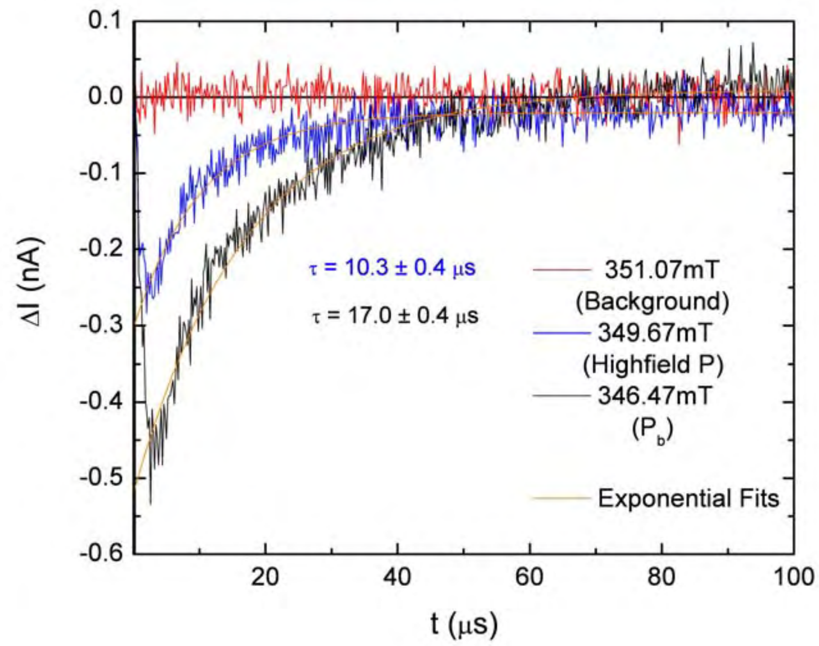

Figure 8.5: Slice through the EDMR spectra at various B corresponding to no resonance (red), high field P resonance (blue), and P_b resonance(black). The orange lines are simple exponential fits to the data, with the characteristic time, τ, indicated next to each.

described earlier.

We now turn to the extra information that can be obtained from these experiments. In addition to the spectra, which are also obtained in cw-EDMR experiments, we now have information about the temporal evolution of the signal. Figure 8.5 shows the time dependence of the signal for three different fields, corresponding to the high field P resonance, the P_b resonance and to a section of the spectra where no resonance is expected. The non resonant trace shows no change as a function of time. The traces for the two resonances show a dip in the current, both having a minima at approximately $t = 3\mu$s. At shorter times, the transient recorded is limited by the rise time of the amplifier, and this data is not able to be used in determining the actual response. Above this time however, the data is found to follow a simple exponential decay of the form $\Delta I(t) = \Delta I_{max} e^{(-t/\tau)} + I_0$, where τ is the characteristic decay time, ΔI_{max} the maximum change in current, and I_0 a small (~ 0), constant offset from 0.

The decay time is found to be $10.3 \pm 0.4\mu$s and $17.0 \pm 0.4\mu$s, for the high field P and P_b transients respectively. The simple exponential nature of the decay is different to that observed in other work. Both Boehme and Lips [147] and Stegner *et al* [77, 143] find that the transient signal is a complex composite of two exponential recombination curves, one enhancing recombination and one reducing recombination. This complex transient characteristic is due to the different recombination probabilities and populations of spin up and down electrons from the conduction band to the P donor after the microwave pulse [76]. However, close inspection of the P_b defect transient represented in figure 8.3 at $t \sim 80\mu$s - 100μs shows an slight increase compared with the background, indicating a reduction in the recombination. This reduction in recombination (increase in current) is not visible in figure 8.4 due to the noise of the measurement, which also limits the visibility in the case of the P resonances.

8.2.1 Noise Considerations

The logical extension of the work presented above is to determine the dependence of the current transient on the microwave pulse length. As shown in reference [77], it is feasible to use this technique to perform coherent Rabi oscillations of the donor electron spin. Unfortunately, the noise present in the system (both sample and measurement setup) at present prevent this measurement.

The signal to noise ratio, for the high field P signal, $S/N|_n = 3.5$, for $n = 175000$ averages. This equates to a single shot $S/N|_1 = 0.0085$. To obtain $S/N|_1 = 5$, which would easily allow the signal to be detected in a single shot, requires an improvement in $S/N|_1$ of approximately 3 orders of magnitude. However, if single-shot measurement is not necessary, such that averaging of the signal 100 times is allowed, and an order of magnitude improvement in both the signal and the noise were achieved, then the measurement with $S/N = 5$ could be undertaken in $\sim$ 20ms, compared with the 30s currently required. The benefit of this improvement is obvious when a measurement of the pulse length dependence is considered. To take data for 1000 different pulse lengths would a present take $\sim$ 8.5 hours, whereas the improvement would allow a similar measurement in 20 seconds. This allows the requirements for the stability of the measurement apparatus to be relaxed, and makes the investigations of these effects experimentally feasible.

8.2.2 Number of donors detected with p-EDMR

Of interest is the number of donors that contribute to the signal being measured. This can be determined by integrating the change in the current to determine the total number of electrons. This will set a maximum on the number of donors that contribute to the signal.

The integral of the P donor peak equates to 2.9×10^4 electrons, which is the maximum of the number of donors that may contribute to the signal. Given the signal to noise of 3.5, this equates to a maximum sensitivity of 8300 donors with $S/N = 1$. This represents an increase in sensitivity of approximately 6 orders of magnitude over conventional pulsed-ESR measurements, and is of the same order of magnitude that has been observed in pulsed EDMR measurements in bulk doped Si:P systems [77].

8.3 Conclusions

The measurements presented above show that the measurement of pulsed EDMR of ion implanted sample is in principle possible. Future work should focus on reducing the noise and increasing the signal to allow the electrical readout of coherent manipulation in few-donor ion-implanted systems. The ultimate aim, single shot electrical readout of the spin of a single donors, remains a formidable challenge, requiring the development of better electronic systems and new device architectures.

Acknowledgements

The measurement shown in section 8.2 was performed by H. Huebl at the Walter Schottky Institute, Germany. The samples were fabricated by the author.

Chapter 9

Conclusions and Future Work

In this thesis, the charge and spin properties of Si:P have been investigated using electrical transport measurements. Different device types and experimental techniques have been utilised as appropriate, and a number of new devices architectures developed where necessary.

9.1 Defect Density, Ion Implantation and Dielectrics

The defect density in Si-MOSFETs was determined by use of mobility measurements at low temperature. This method had the advantage of only measuring defects near the Si-SiO_2 interface, which is the most important region for a number of proposed QC architectures. The defect density of the pristine oxide was found to be $\sim 2 \times 10^{11}$cm^2, which is of order the dopant spacing in these proposals. This result indicates that the oxide will need to be improved for implementation of these types of QC architectures, but that devices consisting of one or two qubits could in principle be fabricated.

This technique was then used to investigate the effect of ion implantation on the defect density. The devices were implanted with 15keV P ions, and then annealed at 1000°C for 5 seconds to repair the damage due to implantation. The number of defects was found to increase linearly with implant density, with an additional 0.08 ± 0.01 defect per implanted ion. However, silicon implantation did not cause an increase in defect density. This lead to the conclusion that the additional traps were actually the additional P donors in the channel of the MOSFET. This fraction of the implanted dose agree well with the number of additional donors expected calculated using implantation modeling for the implant distribution and a Schrodinger-Poisson approach for the electron wavefunction.

This result is promising for the fabrication of both quantum mechanical and non-quantum mechanical electronic devices. As electrical devices become smaller, the effect of individual defects will play a larger role on the transport properties of the device. Since ion implantation is widely utilised in the fabrication of these devices, the ability to perform a low dose implant without creating additional defects is increasingly important.

Measurements on the properties of a number of dielectrics were undertaken. Thermally grown SiO_2 was found to provide the best properties, which was probably to be expected given the numerous and varied exploitation of this material in the semiconductor industry. However, Al_2O_3 deposited via atomic layer deposition was found to have a reasonable quality which, with further optimisation, may provide a high quality oxide for devices with low thermal budgets.

Concluding remarks regarding material research

As with the development of low defect density germanium for the point contact, fundamental work on improving the quality of materials can lead to advances that only become apparent further down the research path. Whilst of-ten laborious, continued study and improvement of the materials properties of systems proposed for quantum information applications remain necessary for the future advancement of the field.

9.2 Electrically detected magnetic resonance

In this thesis, the detection of spin resonance by its effect on the photoconductivity of phosphorus doped silicon was studied. First, a number of experimental parameters were investigated to find the optimum measurement regime. Ion-implanted nanoscale devices were fabricated that allowed the signal from 50 donors to be detected. A second generation of devices, incorporating arsenic implantation of the source and drain leads and ohmic contacts, was developed to confirm these results.

The effect of isotopic purification of the silicon substrate was investigated. In these samples, the phosphorus resonances had much narrower linewidths than in naturally abundant silicon, due to the reduction of the superhyperfine interaction with surrounding spin 1/2 ^{29}Si nuclei.

Finally, a proof of principle demonstration of pulsed electrically detected magnetic resonance on ion implanted samples was presented. These measurements demonstrate a path towards pulsed-EDMR measurment on few, or even a single, donor spins in the solid state.

However, to achieve such measurements, a number of improvements need to be made. Firstly, the signal to noise ratio of the measurements needs to be improved to allow the measurements to be undertaken on experimentally accessible timescales. The easiest way to achieve these improvements involve the reduction of shunt current present in the devices due to the diffusion of photoexcited carriers. This can be achieved by etching small structures into thin silicon-on-insulator material. The etching will provide lateral confinement of the current, whilst the thin ($\sim$ 50nm) device layer of the SOI will restrict the entire current to near the interface defects states necessary for the detection of EDMR. Alternatively, new materials may be investigated. Silicon nanowires are a good candidate, in that they provide a very small volume of silicon, which should provide large EDMR signals due to the extremely high current confinement.

However, alternate physical mechanisms may be more useful for the detection of spin properties of donor states in silicon. One such mechanism uses the difference in scattering cross sections between singlet and triplet pairs of electrons. This mechanism, which has been demonstrated in silicon MOSFETs, may provide a number of technological advantages, such as readout of the spin state on microsecond timescales. Some initial work on such a scheme is presented in Appendix A, as an example of the direction the work presented in this thesis may take.

Concluding remarks regarding single donor spin detection

Whilst the detection of single spins in the solid state have been demonstrated, the methods used have been time intensive, and as such are not able to be exploited for further research into the properties of the individual spins. Future work focused on the improvement of these methods, as well as the development of alternative methods, is required to provide access the unique physics that single spin detection and manipulation allows.

Bibliography

[1] Moore, G. E., Cramming more components onto integrated circuits. *Electronics* **38**, 114 (1965).

[2] Lenstra, A. K. & Lenstra Jr, H. W., *The Development of the Number Field Sieve*. Volume 1554 of *Lecture Notes in Mathematics*. Springer, 1993.

[3] Rivest, R. L., Shamir, A. & Adleman, L., A method for obtaining digital signatures and public-key cryptosystems. *Communications of the ACM* **21**, 120–126 (1978).

[4] Shor, P. Algorithms for quantum computation: Discrete logarithms and factoring, in *Proceedings of the 35th Annual Symposium on the Foundations of Computer Science* (Goldwasser, S., ed). IEEE Computer Society Press, New York, (1994).

[5] Grover, L. K. A fast quantum mechanical algorithm for database search, in *Proceedings of the 28th Annual ACM Symposium on the Theory of Computing (STOC)*. (1996).

[6] Steane, A. M., Error correcting codes in quantum theory. *Physical Review Letters* **77**, 793 (1996).

[7] Steane, A., Multiple-particle interference and quantum error correction.

Proceedings of the Royal Society A: Mathematical, Physical and Engineering Sciences **452**, 2551 (1996).

[8] DiVincenzo, D. P. & Shor, P. W., Fault-tolerant error correction with efficient quantum codes. *Physical Review Letters* **77**, 3260–3263 (1996).

[9] Nielsen, M. A. & Chuang, I. L., *Quantum Computation and Quantum Information*. Cambridge University Press, 2000.

[10] Cirac, J. I. & Zoller, P., Quantum computations with cold trapped ions. *Physical Review Letters* **74**, 4091 (1995).

[11] Nakamura, Y., Pashkin, Y. A. & Tsai, J. S., Coherent control of macroscopic quantum states in a single-cooper-pair box. *Nature* **398**, 786 (1999).

[12] Vandersypen, L. M. K. *et al.*, Experimental realization of shor's quantum factoring algorithm using nuclear magnetic resonance. *Nature* **414**, 883 (2001).

[13] DiVincenzo, D. P., The physical implementation of quantum computation. *Fortschritte der Physik* **48**, 771 (2000).

[14] Loss, D. & DiVincenzo, D. P., Quantum computation with quantum dots. *Physical Review A* **57**, 120–126 (1998).

[15] Vrijen, R. *et al.*, Electron-spin-resonance transistors for quantum computing in silicon-germanium heterostructures. *Physical Review A* **62**, 012306 (2000).

[16] Taylor, J. M. *et al.*, Fault-tolerant architecture for quantum computation using electrically controlled semiconductor spins. *Nature Physics* **1**, 177 (2005).

[17] Ladd, T. D. *et al.*, All-silicon quantum computer. *Physical Review Letters* **89**, 017901 (2002).

[18] Skinner, A. J., Davenport, M. E. & Kane, B. E., Hydrogenic spin quantum computing in silicon: A digital approach. *Physical Review Letters* **90**, 087901 (2003).

[19] Kane, B. E., A silicon-based nuclear spin quantum computer. *Nature* **393**, 133 (1998).

[20] Kane, B., Silicon-based quantum computation. *Fortschritte der Physik* **48**, 1023 (2000).

[21] Geng, H., *Semiconductor Manufacturing Handbook*. McGraw-Hill, 2005.

[22] Sze, S. M., *Semiconductor Devices Physics and Technology*. John Wiley & Sons: New York, 2nd edition edition, 2002.

[23] McGuire, G., *Semiconductor Materials and Process Technology Handbook*. William Andrew Publishing/Noyes, 1988.

[24] HiRes SILICON FOR GHz APPLICATIONS. http://topsil.cms123.com/files/pdf/Topsil_HiRes_leaflet.pdf, 2007.

[25] Haller, E., Isotopically controlled semiconductors. *Solid State Communications* **133**, 693 (2005).

[26] Hollenberg, L. C. L. *et al.*, Charge-based quantum computing using single donors in semiconductors. *Physical Review B* **69**, 113301 (2004).

[27] Chan, V. C. *Charge Sensing and Transport in Silicon Nanostructures*. PhD thesis, School of Electrical Engineering and Telecommunications, The University of New South Wales, 2006.

[28] Feher, G., Electron spin resonance experiments on donors in silicon. I. electronic structure of donors by the electron nuclear double resonance technique. *Physical Review* **114**, 1219 (1959).

[29] Waugh, J. S. & Slichter, C. P., Mechanism of nuclear spin-lattice relaxation in insulators at very low temperatures. *Physical Review B* **37**, 4337 (1988).

[30] Sarma, S. D., de Sousa, R., Hu, X. & Koiller, B., Spin quantum computation in silicon nanostructures. *Solid State Communications* **133**, 737 (2005).

[31] Tyryshkin, A., Lyon, S., Astashkin, A. V. & Raitsimring, A. M., Electron spin relaxation times of phosphorus donors in silicon. *Physical Review B* **68**, 193207 (2003).

[32] Petta, J. *et al.*, Preparing, manipulating, and measuring quantum states on a chip. *Physica E: Low-dimensional Systems and Nanostructures* **35**, 251 (2006).

[33] Liu, L., Valence spin-orbit splitting and conduction g tensor in Si. *Physical Review Letters* **6**, 683 (1961).

[34] Slichter, C. P., *Principles of Magnetic Resonance*. Volume 1 of *Springer Series in Solid-State Sciences*. Springer, 1996.

[35] Poole, C. P. & Farach, H. A., *Theory of Magnetic Resonance*. John Wiley and Sons, 1987.

[36] Feynman, R. P., Leighton, R. B. & Sands, M., *The Feynman Lectures on Physics, Volume 3*. Addison-Wesley, 1966.

[37] Spaeth, J. M. & Overhof, H., *Point Defects in Semiconductors and Insulators*. Springer, 2003.

[38] Abragam, A., *Principles of Nuclear Magnetism*. Oxford Science Publications, 1961.

[39] Bloch, F., Nuclear induction. *Physical Review* **70**, 460 (1946).

[40] Poole, C. P., *Electron Spin Resonance*. Interscience, 1967.

[41] Alger, R. S., *Electron Paramagnetic Resonance: Techniques and Applications*. Interscience, 1968.

[42] Zavoisky, E., Spin-magnetic resonance in paramagnetics. *Journal of Physics of the USSR* **9**, 211 (1945).

[43] Cummerow, R. L. & Halliday, D., Paramagnetic losses in two manganous salts. *Physical Review* **70**, 433 (1946).

[44] Fletcher, R. C. *et al.*, Spin resonance of donors in silicon. *Physical Review* **94**, 1392 (1954).

[45] Feher, G., Fletcher, R. C. & Gere, E. A., Exchange effects in spin resonance of impurity atoms in silicon. *Physical Review* **100**, 1784 (1955).

[46] Feher, G., Donor wavefunctions in silicon by the endor technique. *Journal of Physics and Chemistry of Solids* **8**, 486–489 (1959).

[47] Wilson, D. K. & Feher, G., Electron spin resonance experiments on donors in silicon . III. investigation of excited states by application of uniaxial stress and their importance in relaxation processes. *Physical Review* **124**, 1068 (1961).

[48] Hensel, J. C. & Feher, G., Valance band parameters in silicon form cyclotron resonances in crystals subject to uniaxial stress. *Physical Review Letters* **5**, 307 (1960).

[49] Hensel, J. C. & Feher, G., Cyclotron resonances experiments in uniaxially stressed silicon - valance band inverse mass parameters and deformation potentials. *Physical Review* **129**, 1041 (1963).

[50] Feher, G., Hensel, J. C. & Gere, E. A., Paramagnetic resonance absorption from acceptors in silicon. *Physical Review Letters* **5**(7), 309–311 (1960).

[51] Feher, G. & Gere, E. A., Electron spin resonance experiments on donors in silicon. 2. electron spin relaxation effects. *Physical Review* **114**(5), 1245 (1959).

[52] Feher, G. & Gere, E. A., Polarisation of phosphorus nuclei in silicon. *Physical Review* **103**(2), 501 (1956).

[53] Abe, E., Fujimoto, A., Isoya, J., Yamasaki, S. & Itoh, K. M., Line broadening and decoherence of electron spins in phosphorus-doped silicon due to environmental ^{29}Si nuclear spins. *eprint arXiv:cond-mat/0512404* (2005).

[54] Abe, E. *Pulsed Electron Spin Resonance in Phosphorus Doped Isotopically Controlled Silicon*. PhD thesis, Keio University, 2006.

[55] Maier, D. C., New frontiers in x-band cw-EPR sensitivity. *Bruker Report* **144**, 13 (1997).

[56] Koppens, F. H. L. *et al.*, Driven coherent oscillations of a single electron spin in a quantum dot. *Nature* **442**, 766 (2006).

[57] Rugar, D., Budakian, R., Mamin, H. J. & Chui, B. W., Single spin detection by magnetic resonance force microscopy. *Nature* **430**, 329 (2004).

[58] Xiao, M., Martin, I., Yablonovitch, E. & Jiang, H. W., Electrical detection of the spin resonance of a single electron in a silicon field-effect transistor. *Nature* **430**, 435 (2004).

[59] Yang, A. *et al.*, Optical detection and ionization of donors in specific electronic and nuclear spin states. *Physical Review Letters* **97**(22), 227401 (2006).

[60] Schmidt, J. & Solomon, I., Modulation of the photoconductivity in silicon at low temperatures by electron magnetic resonance of shallow impurities. *Comptes Rendus Hebdomadaires des Seances de l'Academie des Sciences, Serie B: Sciences Physiques* **263**, 169 (1966).

[61] New, D., Donor clusters in silicon. II. esr simulations. *Physical Review B* **32**, 2419 (1985).

[62] Honig, A. & Moroz, M., Precision absolute measurements of strong and highly inhomogeneous magnetic fields. *Review of Scientific Instruments* **49**, 183 (1978).

[63] Stich, B., Greulich-Weber, S. & Spaeth, J.-M., Electrical detection of electron paramagnetic resonance: New possibilities for the study of point defects. *Journal of Applied Physics* **77**, 1546 (1995).

[64] Brandt, M. S. & Stutzmann, M., Spin dependent conductivity in amorphous hydrogenated silicon. *Physical Review B* **43**, 5184 (1991).

[65] Kanschat, P., Lips, K. & Fuhs, W., Identification of non-radiative recombination paths in microcrystalline silicon (μc-Si:H). *Journal of Non-Crystaline Solids* **266**, 524 (2000).

[66] Stich, B., Greulich-Weber, S. & Spaeth, J.-M., Electrical detection of electron nuclear double resonance in silicon. *Applied Physics Letters* **68**, 1102 (1996).

[67] Kawachi, G., Graeff, C. F. O., Brandt, M. S. & Stutzmann, M., Saturation measurements of electrically detected magnetic resonance in hydrogenated amorphous silicon based thin-film transistors. *Japanese Journal of Applied Physics* **36**, 121 (1997).

[68] Murakami, K., Namba, S., Kishimoto, N., Masuda, K. & Gamo, K., Resistance changes induced by electron-spin resonance in ion-implanted si:p systems. *Journal of Applied Physics* **49**, 2401 (1978).

[69] Huebl, H. *et al.*, Phosphorus donors in highly strained silicon. *Physical Review Letters* **97**(16), 166402 (2006).

[70] Koiller, B., Hu, X. & Das Sarma, S., Strain effects on silicon donor exchange: Quantum computer architecture considerations. *Physical Review B* **66**(11), 115201 Sep (2002).

[71] Wellard, C. J. *et al.*, Electron exchange coupling for single-donor solid-state spin qubits. *Physical Review B* **68**, 195209 (2003).

[72] Brandt, M. S. *et al.*, Spin dependant transport in elemental and compound semiconductors and nanostructures. *physica status solidi C* **1**, 2056 (2004).

[73] Lepine, D. J., Spin dependent recombination on silicon surface. *Physical Review B* **6**, 436 (1972).

[74] Greulich-Weber, S., Stich, B. & Spaeth, J. M., Electrical detection of electron paramagnetic resonance: Studies of the mechanism of the spin-dependent recombination process.pdf. *Materials Science Forum* **196**, 1509 (1995).

[75] Dersch, H., Schweitzer, L. & Stuke, J., Recombination processes in *a*-si:h: Spin-dependent photoconductivity. *Physical Review B* **28**(8), 4678 Oct (1983).

[76] Boehme, C. *Dynamics of spin-dependent charge carrier recombination*. PhD thesis, Fachbereich Physik der Philipps-Universitat Marburg, 2002.

[77] Stegner, A. R. *et al.*, Electrical detection of coherent ^{31}P spin quantum states. *Nature Physics* **2**, 835 (2006).

[78] Sze, S. M., *Physics of Semiconductor Devices*. John Wiley & Sons: New York, 2nd edition edition, 1975.

[79] (Rai-Choudbury, P., ed), *Handbook of microlithography, micromachining and microfabrication, Volume 1 : microlithography*. Copublished by SPIE (The International Society for Optical Engineering) and The Institution of Electrical Engineers, 1997.

[80] Buehler, T. M. *The Twin rf-SET: Correlated Single Charge Detection on Microsecond Time-Scales*. PhD thesis, School of Physics, The University of New South Wales, 2003.

[81] Jamieson, D. N. *et al.*, Controlled shallow single-ion implantation in silicon using an active substrate for sub-20-kev ions. *Applied Physics Letters* **86**, 202101 (2005).

[82] Jamieson, D. N. *et al.*, Quantum effects in ion implanted devices. *Nuclear Instruments and Methods in Physics Research B* **249**, 221 (2006).

[83] Chan, V. C. *et al.*, Ion implanted Si:P double dot with gate tunable interdot coupling. *Journal of Applied Physics* **100**(10), 106104 (2006).

[84] Ziegler, J. F., SRIM - the stopping range of ions in matter. http://www.srim.org/.

[85] Shafarman, W. N., Koon, D. W. & Castner, T. G., dc conductivity of arsenic doped silicon near the metal insulator transition. *Physical Review B* **40**, 1216 (1989).

[86] Jones, E. C. & Ishida, E., Shallow junction doping technologies for ulsi. *Materials Science and Engineering: R: Reports* **R24**, 1 (1998).

[87] Shinada, T., Koyama, H., Hinoshita, C., Imamura, K. & Ohdomari, I., Improvement of focused ion-beam optics in single-ion implantation for higher aiming precision of one-by-one doping of impurity atoms into nano-scale semiconductor devices. *Japanese Journal of Applied Physics Part 2 - Letters* **41**, L287 (2002).

[88] Cole, J. H., Greentree, A. D., Wellard, C. J., Hollenberg, L. C. L. & Prawer, S., Quantum-dot cellular automata using buried dopants. *eprint arXiv:cond-mat/0407658* (2004).

[89] McKinnon, R. P. *et al.*, Nanofabrication processes for single-ion implantation of silicon quantum computer devices. *Smart Materials and Structures* **11**, 735 (2002).

[90] Schenkel, T. *et al.*, Solid state quantum computer development in silicon with single ion implantation. *Journal of Applied Physics* **94**, 7017 (2003).

[91] Clark, R. G. *et al.*, Progress in silicon-based quantum computing. *Philosophical Transactions of the Royal Society of London Series A - Mathematical Physical and Engineering Sciences* **361**, 1451 (2003).

[92] Yamasaki, K., Yoshida, M. & Sugano, T., Deep level transient spectroscopy of bulk traps and interface states in si mos diodes. *Japanese Journal of Applied Physics* **18**, 113 (1979).

[93] Peterström, S., Si-SiO_2 interface trap density in boron and phosphorus-implanted silicon. *Applied Physics Letters* **63**, 672 (1993).

[94] Sun, S. C. & Plummer, J. D., Electron mobility in inversion and accumulation layers on thermally oxidized silicon surfaces. *IEEE Transactions on Electron Devices* **27**, 1497 (1980).

[95] Witczak, S. C., Suehle, J. S. & Gaitan, M., An experimental comparison of measurement techniques to extract Si-SiO_2 interface trap density. *Solid-State Electronics* **35**, 345 (1992).

[96] Divakaruni, R. & Viswanathan, C. R., Quasi-static behaviour of MOS devices in the freeze-out regime. *IEEE Transactions on Electron Devices* **42**, 87 (1995).

[97] Saks, N. S., Ancona, M. G. & Rendell, R. W., Using the Hall effect to measure interface trap densities in silicon carbide and silicon metal-oxide-semiconductor devices. *Applied Physics Letters* **80**, 3219 (2002).

[98] Fang, F. F. & Fowler, A. B., Transport properties of electrons in inverted silicon surfaces. *Physical Review* **169**, 619 (1968).

[99] Sarma, S. D. & Hwang, E. H., Charged impurity-scattering-limited low-temperature resistivity of low-density silicon inversion layers. *Physical Review Letters* **83**, 164 (1999).

[100] Xiao, G., Lee, J., Liou, J. J. & Ortiz-Conde, A., Incomplete ionization in a semiconductor and its implications to device modelling. *Microelectronics Reliability* **39**, 1299 (1999).

[101] Snider, G., 1D poisson/schrodinger solver. http://www.nd.edu/~gsnider/1DPoi_PC.ZIP, 1996.

[102] Singh, J., *Semiconductor Devices: Basic Principles*. John Wiley and Sons: New York, 2001.

[103] Park, S. J. *et al.*, Processing issues in top down approaches to quantum computer development in silicon. *Microelectronic Engineering* **73**, 695 (2004).

[104] Schenkel, T. *et al.*, Strategies for integration of donor electron spin qubits in silicon. *Microelectronic Engineering* **83**, 1814 (2006).

[105] Stern, F. & Howard, W. E., Properties of semiconductor surface inversion layers in the electric quantum limit. *Physical Review* **163**, 816 (1967).

[106] Martinis, J. M. *et al.*, Decoherence in josephson qubits from dielectric loss. *Physical Review Letters* **95**, 210503 (2005).

[107] Kravchenko, S. V., Kravchenko, G. V., Furneaux, J. E., Pudalov, V. M. & D'Iorio, M., Possible metal-insulator transition at $B = 0$ in two dimensions. *Physical Review B* **50**, 8039 (1994).

[108] Schofield, S. R. *Atomic-scale placement of individual phosphorus atoms in silicon (001)*. PhD thesis, School of Physics, The University of New South Wales, 2003.

[109] Stasiak, J., Batey, J., Tierney, E. & Li, J., High-quality deposited gate oxide MOSFET's and the importance of surface preparation. *IEEE Electron Device Letters* **10**, 245 (1989).

[110] George, S. M., Ott, A. W. & Klaus, J. W., Surface chemistry for atomic layer growth. *Journal of Physical Chemistry* **100**, 13121 (1996).

[111] Wilk, G. D., Wallace, R. M. & Anthony, J. M., High-k gate dielectrics: Current status and materials properties considerations. *Journal of Applied Physics* **89**, 5243 (2001).

[112] Niinistö, L., Pivsaariand, J., Niinistö, J., Putkonen, M. & Nieminen, M., Advanced electronic and optoelectronic materials by atomic layer deposition: An overview with special emphasis on recent progress in processing of high-k dielectrics and other oxide materials. *physica status solidi A* **201**, 1443 (2004).

[113] George, S. M., Dillon, A. C., Ott, A. W. & Way, J. D., Surface chemistry of al2o3 deposition using al(ch3)3 and h2o in a binary reaction sequence. *Surface Science* **322**, 230 (1995).

[114] Lai, K. *et al.*, Modulation of the high mobility two-dimensional electrons

in Si/SiGe using atomic-layer-deposited gate dielectric. *Applied Physics Letters* **87**, 142103 (2005).

[115] Oh, S. *et al.*, Low-leakage superconducting tunnel junctions with a single-crystal Al_2O_3 barrier. *Superconductor Science and Technology* **18**, 1396 (2005).

[116] Buchanan, D. A. *et al.*, 80 nm poly-silicon gated n-FETs with ultrathin Al_2O_3 gate dielectric for ULSI applications. *International Electron Devices Meeting Technical Digest (IEEE)* , 223 (2000).

[117] O'Brien, J. L. *et al.*, Scanning tunnelling microscope fabrication of arrays of phosphorus atom qubits for a silicon quantum computer. *Smart Materials and Structures* **11**, 741 (2002).

[118] Schofield, S. R. *et al.*, Atomically precise placement of single dopants in Si. *Physical Review Letters* **91**, 136104 (2003).

[119] Schenkel, T. *et al.*, Electrical activation and electron spin coherence of ultra-low dose antimony implants in silicon. *Applied Physics Letters* **88**, 112101 (2005).

[120] Jelezko, F., Gaebel, T., Popa, I., Gruber, A. & Wrachtrup, J., Observation of coherent oscillations in a single electron spin. *Physical Review Letters* **92**, 076401 (2004).

[121] Elzerman, J. *et al.*, Single shot read-out of an individual electron spin in a quantum dot. *Nature* **430**, 431 (2004).

[122] Chan, V. *et al.*, An ion-implanted silicon single-electron transistor. *eprint arXiv:cond-mat/0510373* (2005).

[123] Hudson, F. *et al.*, Coulomb blockade in a nanoscale phosphorus-in-silicon island. *Microelectronic Engineering* **83**, 1809 (2006).

[124] Buehler, T. M. *et al.*, Controlled single electron transfer between Si:P dots. *Applied Physics Letters* **88**(19), 192101 (2006).

[125] Mitic, M. *et al.*, Demonstration of a silicon-based quantum cellular automata cell. *Applied Physics Letters* **89**(1), 013503 (2006).

[126] Pierreux, D. & Stesmans, A., Frequency-dependent electron spin resonance study of P_b-type interface defects in thermal Si/SiO$_2$. *Physical Review B* **66**, 165320 (2002).

[127] Helms, R. & Poindexter, E., The silicon silicon-dioxide system - its microstructure and imperfections. *Reports on Progress in Physics* **57**, 791 (1994).

[128] Toyoda, Y. & Hayashi, Y., Bolometric detection of esr in p-doped si at low temperature. *Journal of the Physical Society of Japan* **29**, 247 (1970).

[129] Lenahan, P. M. & Schubert, W. K., Effects of light and modulation frequency on spin-dependent trapping at silicon grain boundaries. *Physical Review B* **30**, 1544 (1984).

[130] Morooka, M., Tokita, M., Kato, T. & Tsurumi, I., Temperature dependence of esr lines related to phosphorus in silicon. *Japanese Journal of Applied Physics* **33**, 1872 (1994).

[131] Dugdale, D. E., Lacey, S. D. & Lancaster, G., A temperature dependent hyperfine interaction in n-type silicon. *Journal of Physics C: Solid State Physics* **4**, 654 (1971).

[132] Cantin, J. L. & von Bardeleben, H. J., An electron paramagnetic resonance study of the Si(100)/Al_2O_3 interface defects. *Journal of Non-Crystalline Solids* **303**, 175 (2002).

[133] Murakami, K., Masuda, K., Gamo, K. & Namba, S., Effects of ion-implanted atoms upon conduction electron spin resonance (CESR) in a Si:P system. *Applied Physics Letters* **30**(6), 300 (1977).

[134] Young, C. F., Poindexter, E. H., Gerardi, G. J., Warren, W. L. & J.Keeble, D., Electron paramagnetic resonance of conduction-band electrons in silicon. *Physical Review B* **55**, 16245 (1997).

[135] Kishimoto, N. & Morigaki, K., Resistivity decrease due to electron spin resonance in the metallic region of heavily phosphorus-doped silicon. *Journal of the Physical Society of Japan* **42**, 137 (1977).

[136] Morigaki, K. & Maekawa, S., Electron spin resonance studies of interacting donor clusters in phosphorus-doped silicon. *Journal of the Physical Society of Japan* **32**, 462 (1972).

[137] Cullis, P. R. & Marko, J. R., Electron paramagnetic resonance properties of n-type silicon in the intermediate impurity-concentration range. *Physical Review B* **11**, 4184 (1975).

[138] Boehme, C. & Lips, K., Spin-dependent recombination - an electronic readout mechanism for solid state quantum computers. *physica status solidi B* **233**, 427 (2002).

[139] Fletcher, R. C., Hyperfine splitting in spin resonance of group V donors in silicon. *Physical Review* **95**, 844 (1954).

[140] (Lide, D. R., ed), *CRC Handbook of Chemistry and Physics Internet Version 2006 www.hbcpnetbase.com*. Taylor and Francis Boca Raton FL, 2006.

[141] Silicon-28 epitaxial wafers data sheet. http://www.isonics.com/28datasheet.htm, 2006.

[142] Hahn, E. L., Spin echoes. *Physical Review* **80**(4), 580 Nov (1950).

[143] Stegner, A. R. Spin properties of phosphorus donors in silicon epilayers. Diplom Thesis, Physik Department, Technical University Munich, (2005).

[144] Hu, Q., Suzuki, H., Araki, H., Yang, W. & Noda, T., Growth of isotopically enriched ^{28}Si nanowires. *Superlattices and Microstructures* **32**, 255 (2002).

[145] Kettle, L. M. *et al.*, Numerical study of hydrogenic effective mass theory for an impurity P donor in Si in the presence of an electric field and interfaces. *Physical Review B* **68**, 075317 (2003).

[146] Kettle, L. M., Goan, H.-S., Smith, S. C., Hollenberg, L. C. L. & Wellard, C. J., The effects of J-gate potential and interfaces on donor exchange coupling in the Kane quantum computer architecture. *Journal of Physics: Condensed Matter* **16**, 1011 (2004).

[147] Boehme, C. & Lips, K., A pulsed edmr study of hydrogenated microcrystalline silicon at low temperatures. *physica status solidi C* **1**, 1255 (2004).

[148] Ghosh, R. N. *Spin Dependent Transport in a Silicon Two-dimensional Electron Gas*. PhD thesis, Cornell University, 1991.

[149] Ghosh, R. N. & Silsbee, R. H., Spin-spin scattering in a silicon two dimensional electron gas. *Physical Review B* **46**, 12508 (1992).

[150] Lo, C. C. *et al.* Electrically detected magnetic resonance of shallow donors in accumulation layer mosfets, in *Abstract for the March 2007 Meeting of the Americal Physical Society*. (2007).

[151] Schoelkopf, R. J., Wahlgren, P., Kozhevnikov, A. A., Delsing, P. & Prober, D. E., The radio-frequency single-electron transistor (rf-set): A fast and ultrasensitive electrometer. *Science* **280**, 1238 (1998).

[152] Ando, T., Fowler, A. B. & Stern, F., Electronic properties of two-dimensional systems. *Reviews of Modern Physics* **54**, 437 (1982).

[153] Pollak, M. & Geballe, T. H., Low-frequency conductivity due to hopping processes in silicon. *Physical Review* **122**, 1742 (1961).

Appendix A

Development of a new EDMR Scheme

In this chapter, a new device architecture for the manipulation and readout of the spin state of donor electrons in a MOSFET channel is presented. By embedding the MOSFET in a radio frequency tank circuit, changes in the conductance of the device can be monitored on a microsecond timescale. The fabrication process and initial testing of the device is reported.

A.1 Background and Motivation

In 1992, Ghosh and Silsbee [148, 149] presented the result of electrically detected magnetic resonance of donors in a MOSFET channel. They recognised that the spin dependent scattering cross section of the bound donors as seen by the conduction band electrons would allow the detection of ESR of the conduction donors, by monitoring the change in conductivity of the MOSFET due to changing the polarisation of bound donors under ESR conditions. Experimental implementation was undertaken by placing a Si-MOSFET into a resonant cavity, and then detecting the change in current during conventional ESR manipulation. Recently, other groups [150] have begun work on scaling the number of donors present by reducing the size of the MOSFET used, whilst maintaining conventional ESR manipulation involving a resonant cavity.

However, a number of experimental difficulties remain with this technique. One is the difficulty of decreasing the temperature of the MOSFET below ~ 1K due too the necessity of utilising the resonating cavity. Also, the time taken to readout the conductivity of the MOSFET channel prevents the realtime readout of the change in conductivity. this has implications if the realtime readout of free induction decay, possibly involving microsecond timescales.

In this chapter, an architecture for the detection of EDMR by spin dependent scattering in a 2DEG is presented. The aim of this device is to provide a fast readout mechanism for the detection of singlet-triplet scattering differences in two dimensional electron gas, which is operable at millikelvin temperatures.

A.2 Sample Design and Fabrication

The device is shown schematically in figure A.1. It is an accumulation mode MOSFET fabricated on a ^{n}Si <100> wafer with $[P] \sim 10^{16}\text{cm}^{-2}$. Source drain contacts were fabricated via P diffusion (see figure A.1b), with aluminium contact (d= 200nm). A planar microstrip resonator is utilised as the gate. This allows the application of both DC and microwave biases, which is required to induce charge carriers in the MOSFET channel (DC bias), and to induce B-fields in the channel (microwaves). This is discussed in more detail later. The

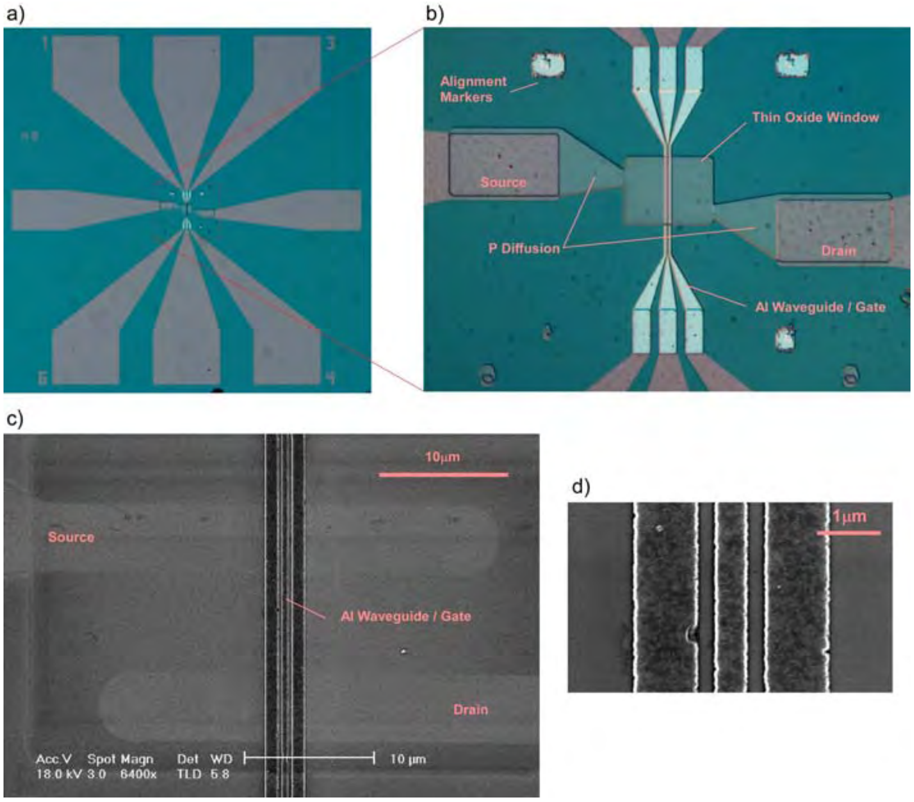

Figure A.1: a) and b) optical micrograph and c) and d) SEM of the devices used in this chapter.

inner of the microstrip is 500nm wide, with 1μm ground planes. The separation between the inner and outer is 300nm. The microstrip was fabricated via EBL. Following evaporation of the Al gates, the device was annealed in forming gas at 400°C for 15 minutes to reduce the effect of interface defects on the device conductivity.

A.3 Measurement Setup and Details

Measurements at microsecond timescales are difficult in dilution refrigerators due to the capacitance of the relatively long wires required, which lead to a large RC time constant with any reasonable device resistance[80]. Schoelkopf *et al* [151] proposed a solution (in their case for the single electron transistor) which involved embedding the transistor in a radio frequency network. It is this technique that is utilised to allow fast readout of the MOSFET.

To allow measurement in a dilution refrigerator, the device was mounted on a patterned PCB, and the measurement circuit built of microcomponents, which is shown in figure A.2a. Figure A.2b shows the entire measurement circuit schematically . The resonant circuit, which allows fast readout, consists of the 330nH inductor, the parasitic capacitance of the MOSFET and the resistance of the MOSFET channel. The measurement circuit also allows simultaneous RF and DC measurement of the channel resistance by application of a source and drain lead to the MOSFET, through two on-board low-pass filter. Each filter consists of a 1kΩ resistor and a 470nH inductor in series. The RF part of the circuit is isolated from the DC part by the addition of two 100pF capacitors on each side of the device, which act as high pass filters for the RF source and ground.

To obtain the maximum B field, the resonator which acts as the gate needs to be terminated near the MOSFET. However, the gate also requires that a DC voltage be applied to induce a 2DEG in the MOSFET. To allow this, the inner of the resonator is connected to ground (and thus the ground planes) via a 56pF capacitor, which allows the microwave component to pass freely to ground whilst also allowing the gate to be set to a DC bias. The DC and microwave components are applied to the gate line via through a room temperature bias tee.

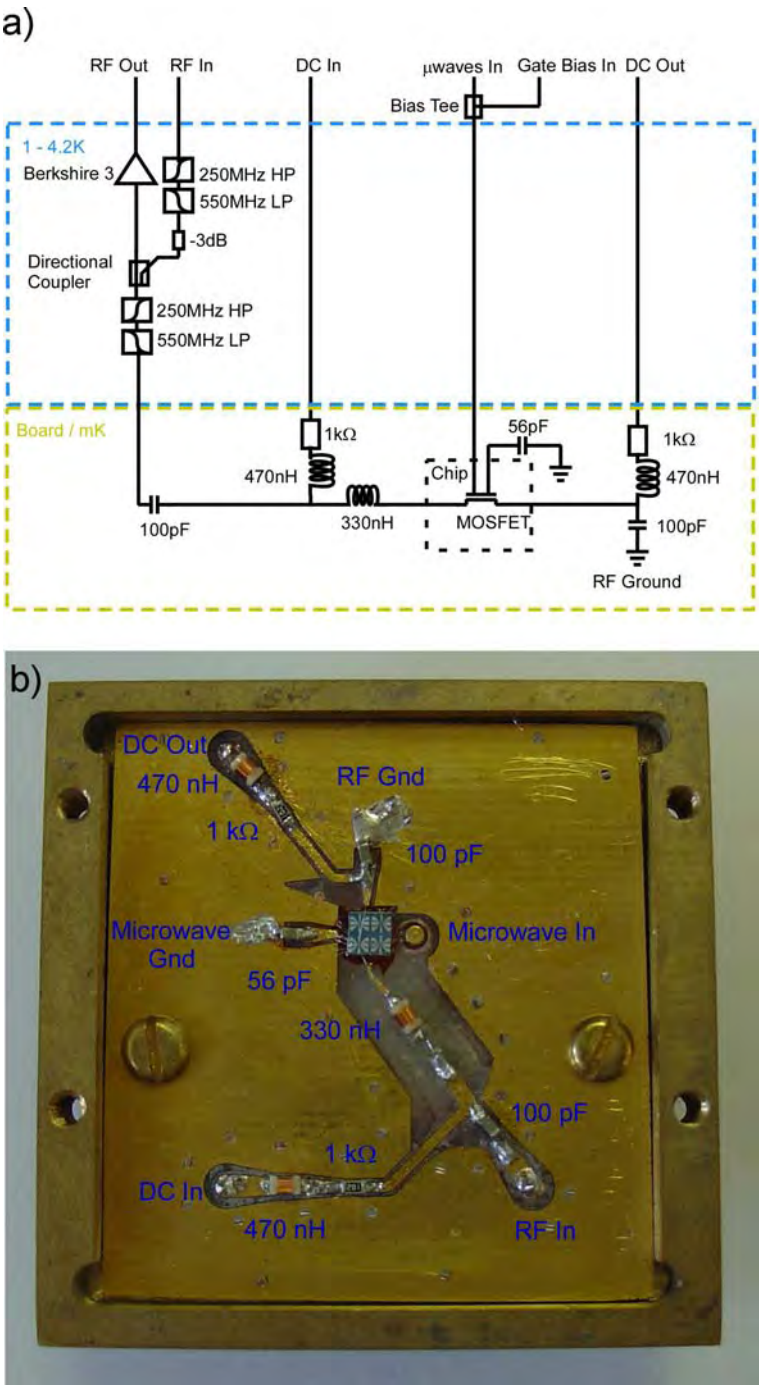

Figure A.2: a) Circuit diagram of measurement setup and b) photograph of the RF board, microcomponents and chip

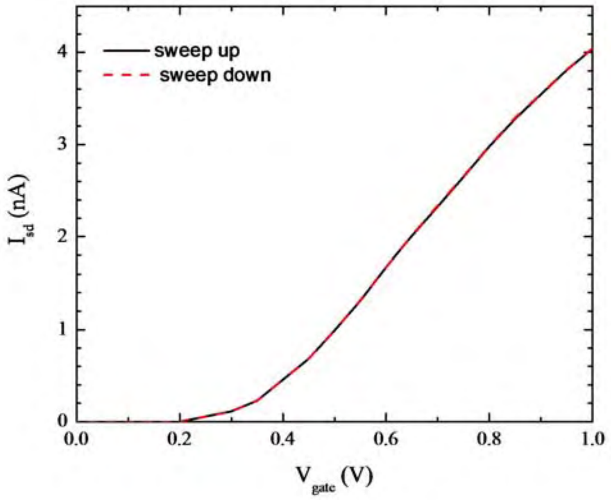

Figure A.3: I_{sd} vs V_{gate} for the device measured at 4K with $V_{sd} = 100\mu V$.

A.4 Measurement of the Device

A.4.1 Simple MOSFET operation

Figure A.3 shows the resistance of the device as a function of the DC gate voltage. Clear MOSFET behaviour is observed. The sheet resistance is less than 1.361k$\Omega/\Box$. The resistance is still in the ionised impurity scattering limit, indicating that the sheet resistivity can become even smaller. However, the gate voltage was limited to 1V to avoid current tunneling through the oxide, which may add noise to the channel current.

The repeatability is demonstrated by sweeping the gate voltage in both the positive and negative direction. These results show an average deviation of the current of 0.22%, with a maximum of 0.46%. This high level of reproducibility is necessary for measurements where small changes in the current are observed.

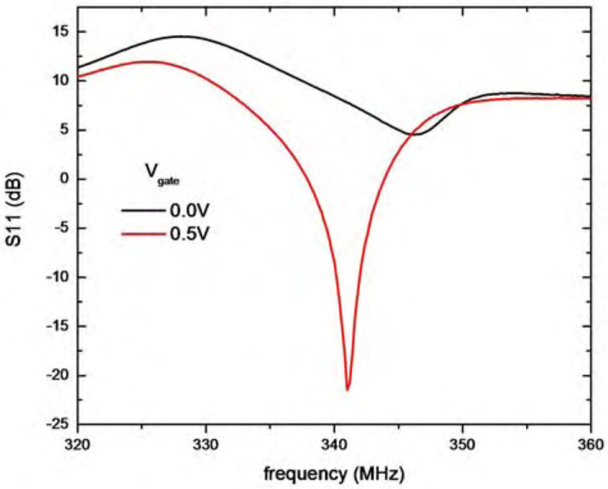

Figure A.4: S11 of the LCR tank circuit as a function of frequency, for V$_{gate} = 0V$ (no MOSFET channel) and V$_{gate} = 0.5V$ (MOSFET channel present).

A.4.2 Operation in an RF tank circuit

Next, the resonance of the tank circuit was investigated. Figure A.4 shows the reflected power from the circuit as a function of frequency for two gate voltages. First, the reflectivity for V$_{\text{gate}} = 0V$ is discussed. In this trace, a small resonance is seen at $f = 346.2$MHz. There is also a small non-linear background, due to the resonances formed by the lines running down the fridge. However, in the trace for V$_{\text{gate}} = 0.5V$, there is a large resonance with a depth of at least 29.3dB. However, this resonance is at a slightly different frequency than the resonance at V$_{\text{gate}} = 0V$, specifically $f = 341$MHz. This frequency shift was investigated by measuring the resonance as a function of the gate voltage, and is discussed below.

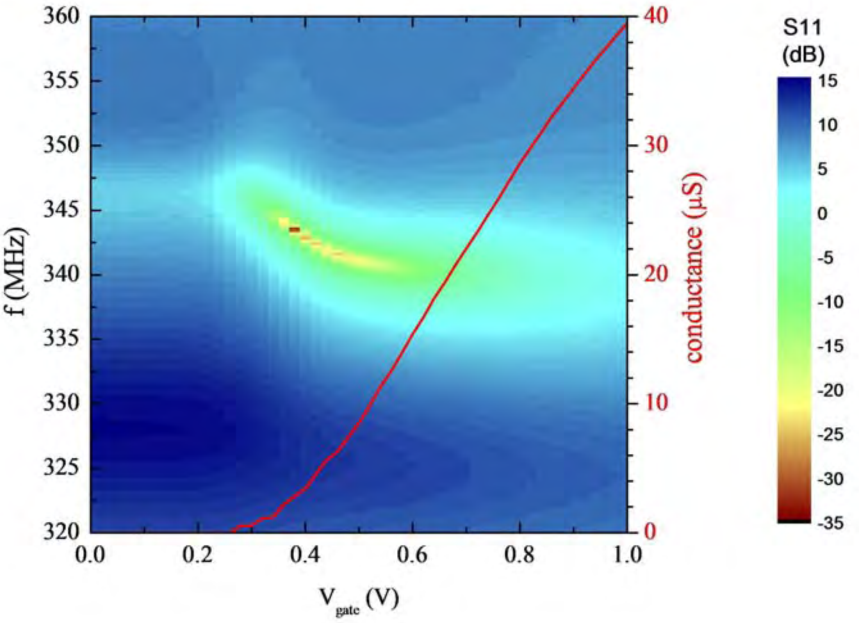

Figure A.5: Reflectance of the LCR circuit (S11) as a function of both frequency and gate voltage, and DC current as a function of gate voltage. Applied microwave power $P_{\mathrm{rf}} = -75\mathrm{dBm}$

A.4.3 Simultaneous RF and DC readout

The resonance and conductance of the device as a function of the gate voltage is shown in figure A.5. A number of features are obvious. Both the resonance frequency and the magnitude of the resonance are both highly gate voltage dependent after the turn on of the device. The position of the resonance, determined by finding the minimum of each frequency trace for each fixed gate voltage, is plotted in figure A.6.

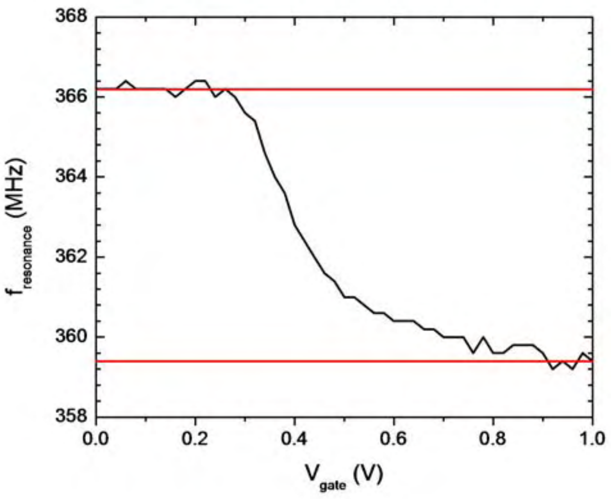

Figure A.6: Resonance frequency of the tank circuit as a function of the MOSFET gate voltage.

The resonance condition of the circuit is satisfied when

$$f = \frac{1}{2\pi}\sqrt{\frac{1}{LC}} \tag{A.1}$$

Since the inductance of the circuit is fixed, the change in resonance must be due to the change in capacitance as the MOSFET channel is formed.

The change in capacitance determined from the change in frequency$\Delta C =$ 21.6aF. Using a simple capacitance model for the MOSFET, its capacitance is determined to be 24 aF when d=7nm, where 5nm is for the oxide, and an additional 2nm for the separation between the interface and the electron wavefunction [152]. This is extremely good agreement, and indicates that the system behaves in a well understood fashion.

Next, the reflectivity of the circuit as is investigated. The matching point for the circuit, where the reflectivity is minimised, should be achieved when

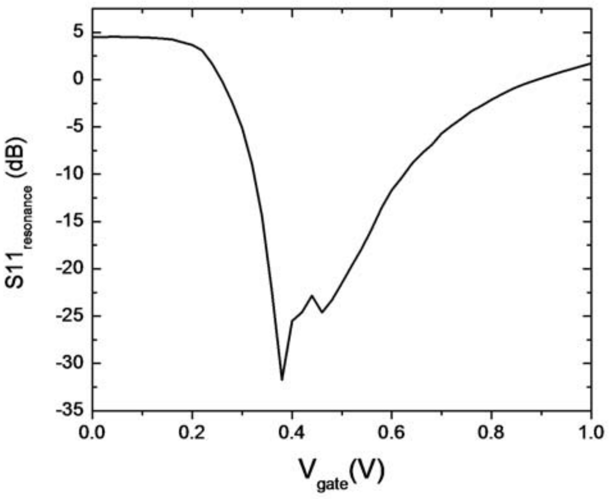

Figure A.7: Reflectivity of the tank circuit vs frequency for two different gate voltages.

the impedance of the circuit

$$Z_{\text{LCR}} = \frac{L}{RC} = 50\Omega \tag{A.2}$$

By substituting the values of L and C determined above, the resistance of the MOSFET at matching should equal $11.5k\Omega$. Figure A.7 shows the minimum value of S11 as a function of gate voltage. The minimum reflectivity is found to occur at $V_{gate} = 0.48V$. At this voltage, the resistance of the MOSFET as determined by the DC current measurements is $353k\Omega$, far from the expected value.

This is an unexpected outcome, which needs to be explained. One possible explanation is that the device conductivity is different for measurements at DC and RF frequencies. Indeed, there is experimental evidence that the conductivity of bulk silicon decreases with increasing frequency, with $\sigma \sim A\omega^s$, where $s \sim 0.8$ and A some constant [153]. This is due to hopping through donor states. Since the conductivity in this case is in a two dimensional channel (or

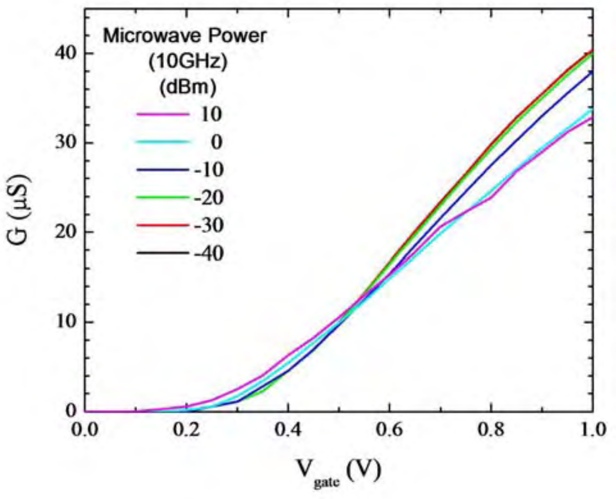

Figure A.8: DC IV measurements taken whilst 10GHz microwaves are applied to the gate, with varying power. $T = 4K$.

near the interface when no gate voltage is applied due to band bending), it is possible that s is less than the 0.8 quoted in ref [153]. However, more work is required to understand the discrepancy.

A.4.4 Operation with applied microwaves

Following the characterisation of the measurement circuit, the effect of the application of microwave power to the device was investigated. Figure A.8shows the IV characteristics as a function of the power for $f = 10$GHz microwaves applied to the gate.

A number of features are notable. Firstly, the threshold voltage of the device decreases as the power is increased. Next, the high gate voltage conductivity decreases with increasing microwave power.

To investigate these effects in more detail, the threshold voltage shift, ΔV_{th},

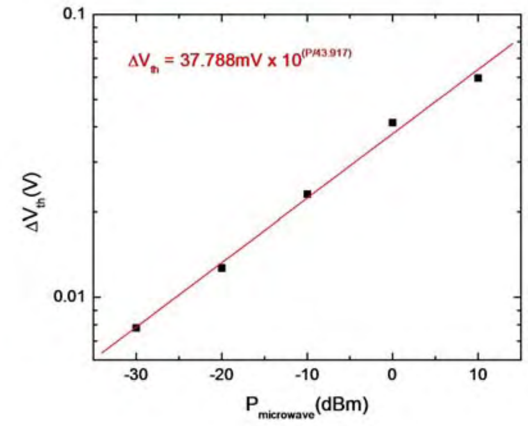

Figure A.9: Change in threshold voltage, ΔV_{th}, vs microwave Power.

as a function of the microwave power was determined, and is shown in figure A.9. The threshold shift is found to increase exponentially with microwave power. This may be due to rectification of the microwave voltage on the gate by the nonlinear IV characteristics of the device. An additional voltage equivalent to the microwave voltage on the gate would serve to reduce the DC threshold voltage. However, this would be impacted by the grounding of the resonator. Detailed modelling of the device beyond the scope of this thesis is required for detailed understanding of its microwave properties. However, the observation that microwaves effect the transport properties of the 2DEG indicate that the microwaves reach the gate, and should allow ESR to be undertaken.

A.5 First attempt at ESR

Figure A.10 shows an attempt at EDMR on the device shown above. The external magnetic field was swept through 10mT about the expected resonance

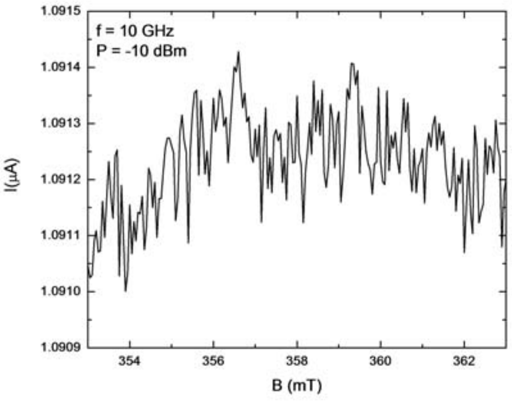

Figure A.10: First attempt at ESR in the MOSFET device. Microwaves with a frequency of 10GHz and power of -10dBm were applied during the measurement.

position of the P donors. Microwaves ($f = 10$GHz, -103dBm) were applied throughout the sweep.

No resonance is visible. This is probably due to the high level of noise in the measurement. The current noise is of order 1 part in 10^{-4}. This compares poorly with the signal observed by Silsbee and Ghosh, where they observe $\Delta I/I \sim 10^{-6}$. To observe such a signal would require the signal to noise ratio to be improved by two orders of magnitude. It is possible that such an improvement may be possible by increasing the size of the MOSFET channel, to remove any effects due to the narrowness of the device.

A.6 Conclusions

In this appendix, initial development and testing of a new device architecture for EDMR has been presented. The device consists of a MOSFET with a coplanar waveguide as a gate, embedded in an RF tank circuit. The measurement circuit allows readout of the device resistance at microsecond timescales, and the coplanar waveguide allows local application of an oscillating magnetic field, required for ESR.

Whilst EDMR has not been observed in this device, it does demonstrates an implementation that would allow fast readout of a small number of donor electron spins in silicon. The readout method should allow experiments that are not possible with conventional EDMR as illumination of the sample is not required.

A.7 Acknowledgements

The work reported in this appendix was undertaken in collaboration with Andrew J. Ferguson and Laurens H. Willems van Beveran.